# High Performance Quantum Dot Laser WDM Arrays for Optical Interconnects

by

Chi-Sen Lee

A dissertation submitted in partial fulfillment
of the requirements for the degree of
Doctor of Philosophy
(Electrical Engineering)
in The University of Michigan
2012

Doctoral Committee:

Professor Pallab Bhattacharya, Chair
Associate Professor Jamie Phillips
Associate Professor Kevin Pipe
Assistant Professor Pei-Cheng Ku

**© Chi-Sen Lee**

**2012**

**To my parents**

## Acknowledgements

Time has gone by so fast. I still remember when I carried that huge luggage and took an 18 hour plane from Taiwan, and landed in the Detroit airport. All of this seems like it just happened yesterday, but it has already been four and a half years. I have received an excellent education and training during this time, and in particular with semiconductor theory and knowledge. I have learned MBE growth, fabrication, and characterization. Of course, I have gotten a lot of help in accomplishing all this. First, I want to express my deepest appreciation to my advisor Prof. Pallab Bhattacharya, with his continuous support and encouragement. I have not only learned the physics and technology behind the work which I have done, but also the ability to set plans for projects, and the attitude to face these difficulties. I would also like to thank my committee members: Prof. Phillips, Prof. Piper, and Prof. Ku for their great suggestions from my prelim to my defense.

Second, I would like to thank all my past and current research group members and friends: Dr. Jun Yang, Dr. Dipankar Saha, Dr. Guan Huang, Dr. Debashish Basu, Dr. Meng Zhang, Dr. Wei Guo Hyun Kum, Ayan Das, Sishir Bhowmick, Animesh Banerjee, Shafat Jahangir, Saniya Deshpande, Allan Xiao, Marc Jankowski, Thomas Frost, Yi-Kuei Wu, I-Ning Hu and Christopher W. Berry. I also want to thank all the support provided by the LNF staff members.

Last, but not least, I would like to thank my parents for their love, patience, support and encouragement. Without them, I could not have pursued and finished my degree

here. I would also like to thank Intel Corporation, for their generous support of the project.

# Table of Contents

Dedication…………………………………………………………………………….....ii
Acknowledgements…………………………………………… ………………………iii
List of Figures……………………………………………………………………….....ix
List of Tables…………………………………………………………………………......xix
Abstract…………………………………………………………………………………..xx

Chapter 1 Introduction………………………………………………………………….1
1.1 Motivatio…………………………………………………………………1
1.2 Future Direction for Device Requirements for Optical Interconnects to
Silicon Chips ………………………………………………………….....3
1.3 Quantum Dot Laser……………………………………………………7
1.4 Dissertation Overview…………………………………………………9
Chapter 2 Performance Characteristics of 1.3 μm Quantum Dot Lasers: Effect of
Growth Parameters……………………..…………………………………….......11
2.1 Introduction………………………………………………………………..11
2.2 Experiment………………………………………………………………...12
2.3 Results and Discussion…………………………………………………15
2.3.1 Dependence on V/III Ratio of InAs QDs…………………….…………15
2.3.2 Dependence on Growth Interruption Time of InAs QDs…………..16
2.3.3 Tunnel Injection and P-doping in Quantum Dot Lasers – Physics
and Technology………………………………………………………..18
2.3.4 Quantum Do Lasers............................................................................21
2.4 Conclusions……………………………………………………………..22
Chapter 3 High Speed 1.22 μm Tunnel Injection p-doped Quantum Dot Excited State
Laser…………………………………………………………………….…......24
3.1 Introduction……………………………………………………………..24

3.2 Experiment……………………………………………………………...25
3.3 Results and Discussion…………………………………………………….28
3.4 Conclusions…………………………………………………………......33
Chapter 4 Quantum Dot Multichannel and Comb Lasers……………………..……….35
4.1 Introduction……………………………………………………………..35
4.2 Experiments……………………………………………………...……..36
4.2.1 MutliChannel Lasers……………………………………………….36
4.2.2 Comb Lasers……………………………………………………..38
4.3 Results and Discussion…………………………………………...........39
4.3.1 MutliChannel Lasers……………………………………………….39
4.3.2 Comb Lasers……………………………………………………..45
4.4 Conclusions……………………………………………………..…..50
Chapter 5 Distributed Feedback and Tunable Distributed Bragg Reflector Lasers
with Quantum Dot Active Region……………………………………………..54
5.1 Introduction……………………………………………………………..54
5.2 Experiment……………………………………………………………...56
5.2.1 Quantum Dot Distributed Feedback Laser….………………………56
5.2.2 Quantum Dot Distributed Bragg Reflector Laser …..………………58
5.2.3 Quantum Dot Tunable Distributed Bragg Reflector Laser……........60
5.3 Results and discussion…………………………………………….....62
5.3.1 Quantum Dot Distributed Feedback Laser….………………………62
5.3.2 Quantum Dot Distributed Bragg Reflector Laser …..………………64
5.3.3 Quantum Dot Tunable Distributed Bragg Reflector Laser……........66
5.4 Conclusion…………………………………………….......….….67
Chapter 6 Monolithic Integration of Quantum Dot Lasers with Waveguides for High
Temperature Operation……………………………………………………..68
6.1 High Temperature Stability of 1.3 µm QD Lasers with Dry Etched
Facets……………………………………………………………………...68
6.1.1 Introduction……………………………………………………...68
6.1.2 Experimen………………………………………………………..69
6.1.3 Results and Discussion……………………………...…………...70

6.1.4 Conclusions……………………………………………………………...77
6.2 1.3µm QD lasers with dry etched lasers integrated with SiN waveguides.77
6.2.1 Introduction……………………………………………………………...77
6.2.2 Design and Experiment…………………………………………………..78
6.2.3 Results and discussion…………………………………………………..83
6.2.4 Conclusions……………………………………………………………...92
6.3 1.3 µm QD cross lasers with dry etched lasers integrated with SiN waveguide……………………………………………………………….…93
6.3.1 Introduction……………………………...…………………………94
6.3.2 Design and Experiment…………………………………………………..69
6.3.3 Results and Discussion…………………………………...……….101
6.3.4 Conclusions……………………………………………………….105
Chapter 7 Conclusions……………………………………………………………….106
7.1 Summary of dissertation…………………………………………………106
7.1.1 Performance Characteristics of 1.3 µm Quantum Dot Lasers: Effect of Growth Parameters ………………………………….106
7.1.2 High Speed 1.22 µm Tunnel Injection p-doped Quantum Dot Excited State Laser………………………………………........107
7.1.3 Quantum Dot Multichannel and Comb Lasers……..………..……107
7.1.4 Distributed Feedback and Tunable Distributed Bragg Reflector Lasers with Quantum Dot Active Region……..........………..........108
7.1.5 Monolithic Integration of Quantum Dot Lasers with Waveguides for High Temperature Operation …………………..……………....109
7.2 Suggestions for Future Work………………........................…………..109
7.2.1 Integrated Single Optical and Longitdunial Mode Coupled Quantum Dot Laser-Waveguide System………………………..109
7.2.2 Hybrid Integration of Quantum Dot Lasers with Coupled Waveguides…………………………….………........................110
Appendix A: Fabrication of Silicon Nitride Waveguides with Dry Etched Coupling Grooves……......……………………………………………112

Bibliography....................................................................................................114

## List of Figures

Figure 1.1 (a) There is an ever increasing need for more bandwidth which (b) electrical interconnects will soon not be able to provide. Optical interconnects, compatible with silicon CMOS technology, are desperately needed to provide future bandwidth needs 2

Figure 1.2 Photonic CMOS enabled wavelength division multiplexing (WDM) Architecture 5

Figure 1.3 Optical network for on-chip and off-chip using dense WDM 6

.

Figure 1.4 Circuit simulation-based optical transceiver power efficiency estimates versus data rate for 45 nm to predictively-modeled 16 nm CMOS technology of integrated optical I/O architecture 6

Figure 1.5 Density of states for charge carriers in structures with different dimensionalities 8

Figure 2.1 The test quantum dot layer structure 14

Figure 2.2 The heterostructure of the quantum dot laser 14

Figure 2.3 AFM images of 2.5 MLs InAs QDs grown at V/III (a) 35 (b) 40 and (c) 45 15

Figure 2.4 Room temperature PL spectra of the QDs with different V/III ratio 16

Figure 2.5 Room temperature PL spectra of the QDs with different growth interrupt time 17

Figure 2.6 AFM images of 2.5 MLs InAs QDs grown at different interruption time (a) 0 (b) 5 and (c) 10 sec 17

Figure 2.7 Schematic of a tunneling injection (TI) quantum dot 19

Figure 2.8 Schematic of p-doped quantum dot 20

Figure 2.9 (a) L-I-V measurements under CW biasing. (b) EL spectra 21
(c) Temperature dependence of $J_{th}$ and the characteristic temperature, $T_0$ and temperature dependence of $\eta_d$ and $T_1$ for each laser 22

Figure 3.1 (a) The heterostructure of the quantum dot laser (b) The reflectivity of the HR coating showing the reflectivity at the excited state (91%) and at the ground state (45%) simulated by transfer matrix method 27

Figure 3.2 Measured photoluminescence and lasing spectra 28

Figure 3.3 Measured light-current (L-I) characteristics 29

Figure 3.4 (a) Cavity length dependence of external quantum efficiency; (b) modal gain vs current density from which a ground state modal gain of 22 $cm^{-1}$ and an excited state modal gain of 56 $cm^{-1}$ are derived 31

Figure 3.5 Measured small-signal modulation response for excited state lasing. A maximum modulation bandwidth ($f_{-3dB}$) of 13.5 GHz is measured 33

Figure 4.1 Heterostructure of the QD laser (a) three different types of QD in 1.3 μm (b) 3 stacks of 1.2 μm InAs QDs and 5 stacks of 1.05 μm InGaAs QDs 37

Figure 4.2 The heterostructure of the quantum dot comb laser with band diagram of one period of tunnel injection QD active region 39

Figure 4.3 (a) Electroluminescence spectrum of the four channels at room temperature (b) L-I measurements of the four lasers under CW biasing 41

Figure 4.4 (a) Electroluminescence and Photoluminescence spectrum of the three channels at room temperature; (b) L-I measurements of the four lasers under CW biasing 42

Figure 4.5 (a) Temperature dependence of $J_{th}$ and the characteristic temperature, $T_0$, for each device; (b) Temperature dependence of $\eta_d$ and $T_1$ for each laser 44

Figure 4.6 Electroluminescence spectrum at 300 K. The inset shows pulsed and CW light-current data at room temperature with threshold current Density $J_{th}$=650 and 675 A/cm$^2$ and differential efficiency $\eta_d$ = 52 and 40%, respectively 45

Figure 4.7 (a) Temperature dependence of $J_{th}$ and $\eta_d$ , from which $T_0$ and $T_1$ were derived to be 110 and 300K; (b) ground-state modal gain versus current density of comb laser from which a saturated modal gain of 4 cm$^{-1}$ per QD layer and a transparency current density $J_{tr}$ = 150 A/cm$^2$ are derived 47

Figure 4.8 (a) Electroluminescence spectra at 300 K in the wavelength range of 1283-1288 nm for two cavity lengths: 1040 and 2060 μm. The respective channel spacing are ~0.2 and 0.1 nm; (b) the inset shows electroluminescence spectra at 300 and 323K with unchanged 0.2 nm peak wavelength spacing 48

Figure 4.9 Small-signal modulation bandwidth of a QD comb laser with L= 1040 μm at different injection current levels. A maximum modulation bandwidth ($f_{-3dB}$) of 7.5 GHz is measured 49

Fig. 4.10 Comb laser-based WDM transceiver options: (a) conventional design based on comb channel de-multiplexing, modulation, and multiplexing in the Tx, de-multiplexing and detection in the Rx 52
(b) unconventional design based on in- line ring resonators for combined channel selection and modulation in the Tx and channel selection and detection in the Rx 53

Figure 5.1 The tunable DBR consists of three sections: the gain, phase, and DBR section with a contact to alter the grating index through a biasing current 56

Figure 5.2 (a) Schematic overview of the DFB structure using a half etched DFB grating. (b) An SEM image of the DFB after fabrication 57

Figure 5.3 (a) The laser heterostructure is presented. (b) The grating consists of deposited shallow metal grating, deposited near the active region 58

Figure 5.4 (a) The grating reflectivity is plotted using the transfer matrix method. (b) An SEM image of the shallow titanium metal grating 59

Figure 5.5 Maximum tunable range of the DBR as a function of (actual) DBR length 60

Figure 5.6 (a) An SEM of the semiconductor grating. (b) A schematic of the grating showing a thin metal strip of metal remaining from the e-beam step acting as contact to the grating. (c) A picture showing the three sections of the fabricated DBR 61

Figure 5.7 (a) The light-current measurements of the DFB show $J_{th}$=258 A/cm$^2$, and $\eta_d$=43%. (b) The spectrum is shown to be a pure single mode at 1286 nm, with FWHM=0.16 nm 62

Figure 5.8 (a) The DFB laser is characterized by $T_0$=60K, and $T_1$=380 K, and 63
(b) a temperature dependence of the lasing wavelength of 0.1 nm/$^o$C 64

Figure 5.9 The emission wavelength occurs at 1333 nm, with a FWHM of 0.2 nm at 1.53 $I_{th}$. The SMSR is ~30 dB 65

Figure 5.10 (a) The light current measurement with a threshold of 298 mA. (b) The temperature dependence of the emission wavelength is 0.1nm/$^o$C 65

Figure 5.11 (a) The laser spectrum is shown as a function of DBR bias voltage 66
(b) the light current characteristics of the laser 67

Figure 6.1 The quantum dot laser heterostrucutre incorporates modulation p-doping of the dot, tunnel injection, and a superlattice structure. A detailed plot of the superlative band diagram, and simulated electron electivity are also shown 69

Figure 6.2 (a) At high temperatures, electrons are able to escape the active region in a structure without a superlattice. (b) The band structure of the superlattice. (c) The superlattice has an effectively higher barrier than the AlGaAs material itself, and the initial barrier blocks low energy (<$U_0$) electrons from tunneling through the superlattice 70

Figure 6.3 A smooth dry etched facet is created using a $Cl_2$+Ar+$BCl_3$ dry etching recipe 72

Figure 6.4 (a) The facet is intentionally roughened using a non-optimized dry etching recipe. (b) I use an HBr based wet chemical etching to polish the roughened facet, leaving smooth facet, which can serve as a good laser cavity mirror 73

Figure 6.5 (a) The electroluminescence shows a lasing wavelength of 1304 nm. (b) The L-I-V characteristics are shown as a function of temperature. (c) The temperature dependence of threshold and external quantum efficiency are shown 75

Figure 6.6 (a) Light-current-voltage characteristics of a laser with both facets dry etched (b) The temperature stability in the same device 76

Figure 6.7 (a) The quantum dot laser heterostructure used as the integrated optical source with the waveguides. (b) I wish to maintain a high laser reflectivity ($S_{11}$) in order to minimize the laser threshold, while coupling as much of the remaining power as possible ($S_{21}$) 79

Figure 6.8 (a) The laser reflectivity and transmission are simulated and plotted as a function of groove width. (b) As the width of the waveguide is made wider, the coupled power increases. This particularly important for smaller lasers which have a greater divergence angle, and for wider grooves 81

Figure 6.9 (a) The side view of the system showing the coupled laser/waveguide system, separated by a 2.1 μm coupling groove. (b) The overhead view of

the system with a 4μm laser coupled to an 8μm waveguide, which is subsequently tapered to 800 nm 82

Figure 6.10 (a) The waveguide is coupled to the laser by a dry etched groove of ~2.1 μm to provide reflectivity similar to that of a cleaved laser facet. (b) The tip of the waveguide is made 800 nm wide in order to prevent the propagation of higher order mode 84

Figure 6.11 (a) The output spectrum shows a single mode at 1.298 μm at 1.4 $I_{th}$ at 300K. (b) The L-I measurements demonstrate the excellent coupling from the laser into the waveguide. (c) Temperature dependent threshold measurement show excellent temperature stability with $T_0$~∞ from 5-55$^o$C. (d) From the fitting of $J_{th}(\infty)$, and C, the reflectivity of the dry etched groove facet can be calculated for each device 85

Figure 6.12 The calculated propagation loss is 11 dB/cm. The insertion loss of 3.2 dB is largely due to the tapering loss, but is also contributed to bythe radiated power in the groove 87

Figure 6.13 As the width of the waveguide is tapered to narrower dimensions, more power is radiated away in the tapered region. Additionally, at ~800 nm, the waveguide is below the cutoff of the 1$^{st}$ higher order mode, so no power propagates in this mode 90

Figure 6.14 Using a double tapered waveguide will allow for a reduced tapering and propagation loss 91

Figure 6.15 L-I measurements from both single tapered and double tapered devices with comparable threshold, showing a higher slope efficiency in the double tapered devices 92

Figure 6.16 Two possible mode filtering laser geometries, in an overhead view, with the green representing the laser cavity. (a) A tapered laser allows more power to be generated, but the narrow region prevents lasing in higher order modes. (b) The cross waveguide also induces a large loss in higher order modes ..... 94

Figure 6.17 Shows how the mode propagates through the cross. Starting at bottom, as the mode enters the cross, it begins to expand. When the mode reaches the other edge of the cross, it is forced to rapidly contract, radiating a large portion of the power. This loss prevents the higher order modes from lasing. The fundamental mode diverges the slowest, and experiences the least loss ..... 95

Figure 6.18 The transmission of the fundamental mode and first higher order mode are presented as a function of cross length. The width of the filter is kept constant at 30 µm ..... 97

Figure 6.19. The mode filter has gradual tapers, allowing the fundamental mode which has diverged less a short distance to contract back into the narrow region. Higher order modes have diverged too much for this to help, and still experience a large loss ..... 98

Figure 6.20 Device heterostructure with the ridge illustrated. The greyed out region represented the material removed to form the ridge. The etch depth is chosen to be 1200µm in order to prevent fundamental mode divergence into the mesa ..... 99

Figure 6.21 (a) The hexagonal mode filter is added to the standard ridge waveguide laser to filter out higher order modes, which allows for the use of a wider, non-single mode waveguide. (b) The lases (right) is integrated with a silicon nitride waveguide (left) ..... 100

Figure 6.22 (a) The laser with the mode filter (red) shows near identical slop efficiency as compared to a standard laser without the filter, and only a slight increase in threshold. (b) The mode filtered laser with integrated waveguide is characterized by near temperature insensitive performance with $T_0$~∞ between 5°C to 40°C ........ 101

Figure 6.23 The spectrum from the mode filter laser shows a peak emission wavelength of 1305nm ........ 102

Figure 6.24 (a) The measured mode profile of the laser as captured by the camera, and (b) a contour plot of the relative mode profile ........ 103

Figure 6.25 (a) The laser with the mode filter (red) shows near identical slop efficiency as compared to a standard laser without the filter, and only a slight increase in threshold. (b) The mode filtered laser with integrated waveguide is characterized by near temperature insensitive performance with $T_0$~∞ between 5°C to 40°C ........ 104

Figure 7.1 A potential integration scheme of a single longitudinal mode DBR Laser coupled to a tapered-to-single-mode silicon nitride waveguide ........ 110

Figure 7.2 The GaAs based QD laser is integrated with a silicon nitride waveguide, whose mode is coupled to another waveguide on the silicon wafer ........ 111

Figure A.1 Laser device is processed using standard techniques ........ 112

Figure A.2 The $SiO_2$ cladding and $Si_3N_4$ core coat the sidewall of the laser. This is too thick to etch directly (~4 µm) ........ 113

Figure A.3 The laser facet is dry etched, and the sidewall coating is allowed to crack naturally 113

# List of Tables

Table 1.1 Key Parameters for Technology Node, On- and Off-Chip Clock Frequencies, and Signal Pins From the ITRS 2007 Roadmap......................7

Table 1.2 Integrated optical I/O link budget..................................................7

## Abstract

Robust photonic integrated circuits (PICs) capable of operating at high temperatures with low power consumption, low delay, and good signal integrity will be essential for future on-chip communication. The most practical communication system would be a WDM or DWDM optical communication system consisting of an array of closely spaced (in wavelength) tunable lasers. Ultimately, for such a communication system, integrated photo-transceivers capable of delivering a high data rate (20-40 GB/s) with low power consumption (1mW/GB/s) are desirable. The lasers and photonic circuits must also function reliably in the microprocessor environment, where the case and junction temperatures can reach ~100°C. In other words the form factor and reliability must be consistent with CPU systems.

InAs/GaAs self-organized quantum-dots (QDs) lasers on GaAs substrates for 1300 nm light source, as an alternative to the traditional InP lasers, have drawn much attention recently. The GaAs-based QD lasers have achieved low threshold current density, high output CW-power, and high characteristic temperature ($T_0$). I use a novel two step growth process to grow dense and uniform QDs, with an emission at 1300 nm. First, I use a relatively high growth rate in order to grow a dense 2 ML QD seed layer. The relatively small QDs (2 ML) will reduce the possibility of forming coalescent dots. This is followed by a series of growth interruptions until the total deposition reaches 2.5 ML. I calibrated the growth interruption time and found that 5 seconds was the best time to use. Finally, a 7-QD-stack laser with the best growth conditions is designed. Superlattice barrier, p-type

modulation doping and tunnel injection is incorporated into the active region to further improve the device performance was grown and fabricated.

Quantum dot lasers emitting in the excited state have been shown theoretically to have a much higher direct modulation bandwidth due to the two-fold degeneracy in the excited state, and the associated saturation gain. Using a wavelength selective high reflectivity mirror coating, designed to suppress lasing in the ground state, I fabricated a device forcing excited state lasing at 1.22 μm. The excited state laser is characterized by saturation modal gain is 56 $cm^{-1}$ and small signal modulation bandwidth is 13.5 GHz.

The realization of a tunable laser will allow for the creation of an array of identical lasers with varying output wavelengths. To this end, I grew a laser heterostructure with layers of varying size quantum dots, and created a tunable array by varying the device cavity length. The carriers fill the states in the QDs in the following manner. The carriers first fill the states in the largest QDs due to the lower energy level. After overcoming the total loss, the laser begins lasing at this lowest energy level. However, the largest QDs have the least gain, and they have fewer stacks, which only allow them to overcome the loss at the longest cavity length. Conversely, the laser which has the shortest cavity length, can only lase with the smallest QDs, which have more stacks and a higher modal gain.

An alternative to using an array of expensive single mode DFB or DBR lasers is to utilize the highly uniform longitudinal modes of a single Fabry-Perot laser wherein the mode spacing can be varied by altering the cavity length. Such multi-wavelength emitters or comb lasers need to satisfy several conditions. First, the active medium should display a uniform and broadband gain spectrum with a sufficiently large value of gain to enable lasing in the entire desired wavelength range. I report the characteristics of a 1.3 μm

quantum dot comb laser with an electroluminescence linewidth of 75.9 nm achieved by variations in molecular beam epitaxy (MBE) techniques. The large modulation bandwidth, a direct consequence of tunnel injection, implies that individual channels can be modulated at a frequency of ~7.5 GHz. Therefore, several identical high-speed comb lasers with direct (current) modulation can be used in a WDM—Passive Optical Network (WDM—PON) architecture.

I demonstrate the use of DFBs and DBRs to create single longitudinal outputs. I also apply a contact to the grating, and use a phase section to create a tunable DBR, with a tunable wavelength range of 4 nm. Additionally, an important element of such PICs is a low-loss monolithically integrated waveguide/directional coupler which can couple and/or transfer information from the laser to the CMOS chip. I fabricated monolithically integrated silicon nitride waveguides with low insertion loss of 3.2 dB, and propagation loss of 11 dB/cm. I also demonstrate the use of the mode filter laser to create a single mode output without the need for a single mode waveguide.

# Chapter 1

# Introduction

## 1.1 Motivation

In terms of computing power, the CPU is the most important element of a computer system. On personal computers and small workstations, the CPU is housed in the microprocessor chip. As shown in Fig. 1.1 (a), at the present time, there is an urgent need for large bandwidth (exceeding 200 GB/s) in the CPU, for high-end applications, Fig. 1.1 (b) shows that electrical interconnects are rapidly becoming non-suitable to provide the large bandwidth required [1,2]. At the present time there is an urgent need for large memory bandwidth (exceeding 100 GB/s) in the CPU, for high-end applications, such as for servers. While on-die embedded memory architecture is an option, it is not very practical. A more attractive option is an off-die arrangement where the memory is situated in a package away from the CPU. As this memory distance increases, there is a need for low-power, high data-rate communication links (20-40 GB/s). The most practical communication system would be a WDM or DWDM optical communication system consisting of an array of closely spaced (in wavelength) tunable lasers. Ultimately, for such a communication system, integrated photo-transceivers capable of delivering a high data rate (20-40 GB/s) with low power consumption (1mW/GB/s) are desirable. The lasers and photonic circuits must also function reliably in the microprocessor environment, where the case and junction temperatures can reach ~100°C. In other words the form factor and reliability must be consistent with CPU systems.

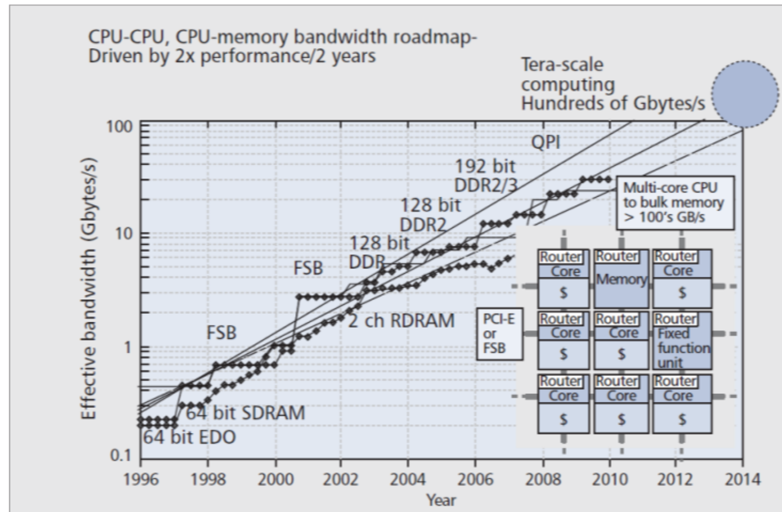


(a)

(b)

Fig. 1.1 (a) There is an ever increasing need for more bandwidth which (b) electrical interconnects will soon not be able to provide. Optical interconnects, compatible with silicon CMOS technology, are desperately needed to provide future bandwidth needs.

At the heart of the optical interconnect system is a suitable tunable laser, which must have ultralow threshold current insensitive to temperature (large $T_0$) up to large ambient temperatures. The laser should also have narrow spectral linewidth and display negligible filamentation of the output beam.

## 1.2 Future Direction for Device Requirements for Optical Interconnects to Silicon Chips [1,3-5]

Just as transistor shrinkage produced exponential growth in CPU performance (Moore's Law), and unprecedented economies of scale, increasing the number of CPU cores integrated on the microprocessor will produce similar performance scaling. The microprocessor architecture transition from multi-core to many-core will drive increased chip-to-chip I/O bandwidth demands at processor/memory interfaces and in these many-processor systems. Future architectures will require bandwidths of 200GB/s to 1.0TB/s and will bring about the era of tera-scale computing. It will become necessary to provide interconnect scaling to achieve higher bandwidth between the cores on chip, and between these cores and the off-chip DRAM. For on-chip interconnects, there is an upper limit on energy consumption. The International Technology Roadmap for Semiconductors estimates an upper boundary of 200 W for the amount of heat that can be removed from a chip in a cost-effective way [6]. A second consideration is the required interconnect density and the available (cross-sectional) area for it. Next generation system architectures will require around 80 Tb/s [7] up to 780 Tb/s per chip, expected in 2022 [4]. With data rates of 10–20 Gb/s per channel, this means that the required number of channels is in the order of thousands to tens of thousands. However accommodating an architecture for the required (tens of) thousands of channels is a significant implementation challenge. Dense WDM seems the only feasible approach, and in [7], an approach is proposed with 250 waveguides transmitting 64 wavelengths, i.e., making a total of 16 000 channels that can run at 10 Gb/s each. Such an architecture can be implemented in a single layer. A photonic CMOS architecture for optical WDM of

signals monolithically integrated on-chip is shown in Fig. 1.2. The ring resonator modulator selectively modulates a single wavelength from a multi-wavelength source and eliminates the need for separate optical de-mulitiplexers and multiplexers [3]. At the receiver, passive ring resonator optical filters can de-multiplex the optical data by selecting a single unique wavelength for detection at each photodetector. Since the photonic CMOS ring resonator modulators have such a narrow tuning range, the WDM wavelengths can be spaced at less than 1 nm (100 GHz in optical frequency with a reference of 230 THz). Thus, the ring resonator technology provides the means for bandwidth to scale by adding more wavelengths to each waveguide channel. In addition to bandwidth scaling through WDM, optical signals also enable a switchable high-bandwidth optical network for both on-chip and off-chip. Data can be routed to a determined core. Fig. 1.3 shows future 3D-integated chip consisting of several layers connected with each other with very dense and small pitch interlayer vias of optical networks on-chip and off-chip using dense WDM [8]. The lower layer is a processor itself with many hundreds of individual cores. The memory layer (or layers) are bonded on top to provide fast access to local caches. On top of the stack is the Photonic layer with many thousands of individual optical devices (modulators, detectors, switches) as well as analogue electrical circuits (amplifiers, drivers, latches, etc.). In this device, the photonic layer is not only responsible for providing point to- point broad bandwidth optical links between different cores and off-chip traffic, but also to route this traffic with an array of nanophotonic switches. Fig. 1.4 shows circuit simulation-based power efficiency estimates of transmit and receive front-end circuits, excluding the clock timing systems, for these two optical I/O architectures in CMOS technologies spanning from 45

nm to predictive 16 nm [3]. This analysis predicts that hybrid optical data transmission at 1 pJ/b will be realized in the future. Assuming a 1310 nm CW laser source with 3 dBm optical power, the integrated optical link power efficiency, displays similar behavior at a much lower power level due to low capacitance of the modulator and photodetector allowing for very efficient optical drivers and receivers. Ultra-low receiver input capacitance allows a trans-impedance amplifier based receiver without any limiting amplifier stages to provide sufficient sensitivity at data rates exceeding 30 Gb/s. The data rate at which extra limiting amplifier stages become necessary scales with the improved CMOS technology , as seen by the discrete jumps in the power efficiency curves. These projections indicate that photonic CMOS will enable integrated optical interconnect to reach 0.3 pJ/b. I summarize summary conclusions from the energy targets and integrated optical I/O links are shown in Fig. 1.5 and table 1.1 and 1.2 [3-4].

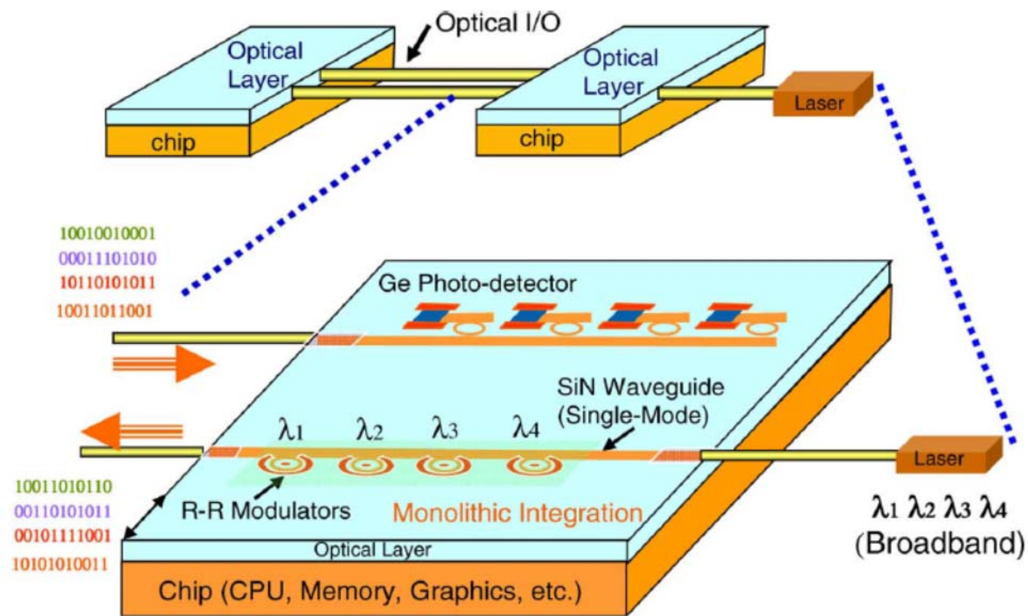


Fig. 1.2 Photonic CMOS enabled wavelength division multiplexing (WDM) architecture.

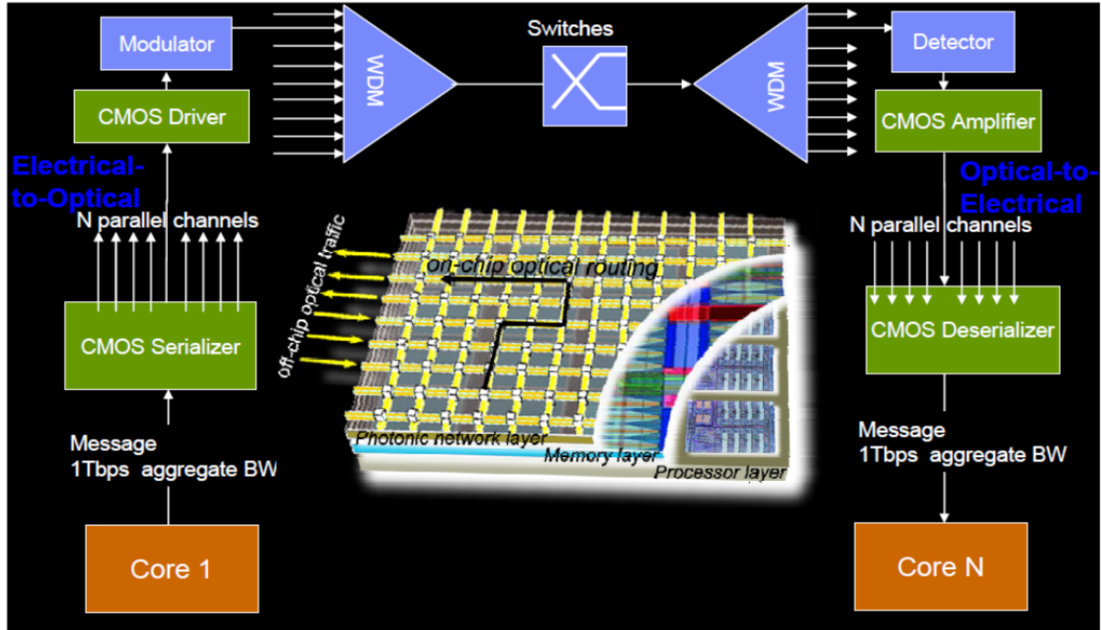


Fig. 1.3 Optical network for on-chip and off-chip using dense WDM.

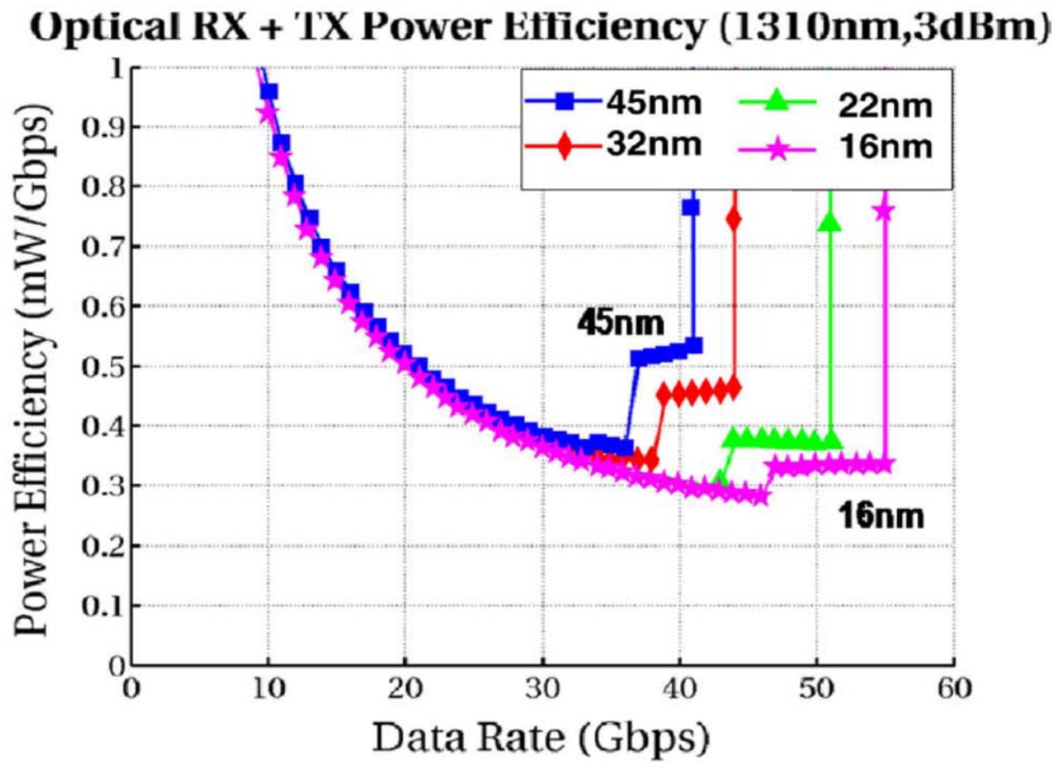


Fig. 1.4 Circuit simulation-based optical transceiver power efficiency estimates

versus data rate for 45 nm to predictively-modeled 16 nm CMOS technology of integrated optical I/O architecture.

| Year | Tech Node(nm) | On Chip Clock (GHz) | Off Chip Clock (GHz) | Signal Pins | Total I/O (Tb/s) | fJ for off Chip |
|---|---|---|---|---|---|---|
| 2015 | 65 | 8.5 | 29.1 | 2800 | 82 | 490 |
| 2022 | 25 | 14.3 | 67.5 | 3420 | 230 | 170 |

Table 1.1 Key Parameters for Technology Node, On- and Off-Chip Clock Frequencies, and Signal Pins From the ITRS 2007 Roadmap.

| Source CW Laser Power | 3.0 dBm |
|---|---|
| Source Laser to SMF Coupling | -2.0dB |
| SMF to Modulator Coupling | -2.0dB |
| Modulator Loss | -2.0dB |
| Modulator to SMF Coupling | -2.0dB |
| SMF to Photodetector Copling | -3.0 dB |
| Extinction Ration (8dB) Penalty | -1.4 dB |
| Margin | -3.0 dB |
| Link Budget | -15.4 dB |
| Required RX Sensitivity | -12.4 dBm |

Table 1.2 Integrated optical I/O link budget.

### 1.3 Quantum Dot Laser

Since the first theoretical predication and experimental demonstration by Arakawa and Sakaki in 1982 [9], quantum dot (QD) lasers have been expected to outperform bulk, quantum well (QW) and quantum wire lasers. The three-dimensional quantum confinement of the electrons and holes in a quantum dot with size equal to or below the exciton results in a delta-function-like density of state as can be seen in Fig. 1.5 [10]. Therefore, semiconductor lasers with quantum dot active regions are expected to have a low threshold current density [11-13], high characteristic temperature [14-16], high material gain [11], and large modulation bandwidth [17].

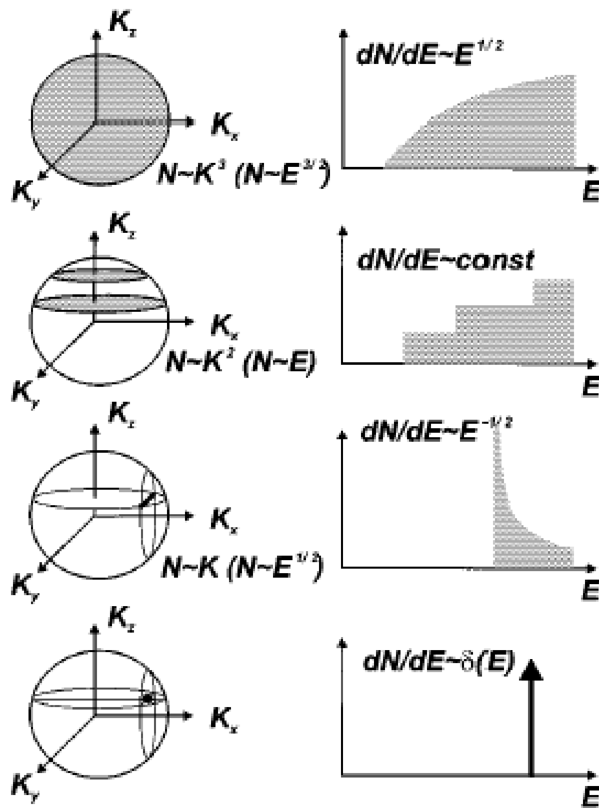


Fig. 1.5 Density of states for charge carriers in structures with different dimensionalities.

Up to date the most successful method to realize quantum dot structure is through the self-organization of quantum dots. During the highly strained heteroepitaxy the formation of the three-dimensional structure provides a way of strain relief and prevents the formation of dislocations. Uniform dots with small size, high density and high emission efficiency can be easily realized in conventional molecular beam epitaxy (MBE) and metalorganic vapor phase epitaxy (MOVPE).

Quantum dot lasers are one of the most representative candidates for the practical application of quantum dot structures. In 1994, the first edge-emitting, current injection

laser using self-assembled QDs as the active region was demonstrated [18]. That was an AlGaAs/GaAs GRIN-SCH laser with 1-mm-long cavity length, its threshold current density is 120 A/cm$^2$ at 77K and as high as 950 A/cm$^2$ at room temperature. The characteristic temperature is 350K between 50 and 120K. It should be noted that Bhattacharya's optoelectronics group at the University of Michigan was one of the first groups to report room temperature operation and the modulation properties of QD lasers [19]. After this work, significant progress on the performance of QD lasers has been made. In 1999, the first QDs laser with threshold current density lower than QW lasers was achieved by Liu [20]. The current density was only 26 A/cm$^2$. Regarding the characteristic temperature, in 2004, Fathpour et. al used p-doped quantum dots to obtain an almost temperature insensitive ($T_0 = \infty$) quantum dot laser in the temperature range from 5 to 75°C [15].

By placing InAs/GaAs QDs in InGaAs quantum wells or capping InAs/GaAs QDs with InGaAs layer, the emission wavelength of the laser can be extended to 1300 nm or even further longer wavelength range [20,21-29]. Since the high-index-contrast AlAs/GaAs DBR can be easily grown on GaAs substrate, vertical cavity surface emission lasers (VCSELs) based on this type of quantum dot structure are expected to achieve high performance and low cost simultaneously. Therefore, the device has been a very promising candidate for GaAs long-wavelength lasers, which have the potential to replace InP-based DFB lasers in metro or access networks in the future. Therefore, quantum dot lasers have become the best candidate for an optical interconnection source.

### 1.4 Dissertation Overview

The thesis is organized in the following manner. Chapter 2 describes the details of our

experiments including the growth and structures design of the lasers. Device fabrication and measurement results are also included. In chapter 3, I report the use of direct modulation on excited state quantum dot lasers, which emit in the excited state due to a high-reflectivity facet coating which is designed to suppress ground state lasing in the devices. This allows for a directly modulated device to be used in optical interconnects. In chapter 4, I report on the characteristics of a 4-channel multi-wavelength laser, where the emission wavelength is controlled by varying the cavity length. I can easily varying the length of the metal contact to make the different cavity length devices on the same chip. I also report our study on an InAs/GaAs QD comb Laser which is another scheme of optical interconnection source. In chapter 5, the design and characterization of distributed feedback (DFB) and dsitrubted Bragg reflector (DBR) lasers is done to create lasers which emit at a single longitudinal mode. Additionally, the design of a tunable DBR, whose output wavelength is controlled by applying a bias to the grating section, is designed, fabricated, and characterized. In chapter 6, I investigate the use of dry etching as an alternative to cleaving for creating the laser facets. Additionally, I use these techniques to form the groove between the laser and a coupled silicon nitride waveguide. I investigate the use of single mode lasers and narrow single mode waveguides for creating single spacial mode output. Finally, in chapter 8, I will briefly summarize my work, and give potential future topics further investigating these topics.

# Chapter 2

# Performance Characteristics of 1.3 µm Quantum Dot Lasers: Effect of Growth Parameters

## 2.1 Introduction

InAs/GaAs self-organized quantum-dots (QDs) lasers on GaAs substrates for 1300 nm light source, as an alternative to the traditional InP lasers, have drawn much attention recently. The GaAs-based QD lasers have achieved low threshold current density [11-13], high output CW-power [30], and high characteristic temperature ($T_0$) [14-16]. There are several approaches to achieving 1300 nm emission. The first approach is utilizing growth techniques to control the shape and size of QDs. Sub-monolayer (ML) deposition method for InGaAs QDs [31] and ultra-low growth rates for InAs QDs at high temperature [32] have been reported in literature. However, these methods provide low QD density of only 1-2 × $10^{10}$ $cm^{-2}$, which may limit the maximal ground-state gain in laser applications. Another approach is capping a layer on InAs QDs [33] or embedding InAs QDs in a quantum well [34]. InGaAs [35-36], InAlGaAs [37], GaAsSb [38], and InGaAsN [39] have been chosen to be overgrown on the InAs QDs as a capping layer. Among these, InGaAs with In mole fraction less than 0.2 is the most widely studied capping layer for InAs QDs. Capping InGaAs layer over the InAs QD may reduce the strain in InAs QDs [35-36], cause less In/Ga intermixing between QD and capping layer [37], and provide smaller band discontinuity between QD and capping layer [40]. In this chapter, I first study the growth of seed InAs QDs. The optimum V/III ratio for best optical and structural

properties is presented. To achieve emission of 1300 nm, I deposited a thin $In_{0.15}Ga_{0.85}As$ capping layer on the InAs QDs seed layer. Effects of growth method were also investigated. The optical and structural properties of the samples were characterized by room temperature photoluminescence (PL) and atomic force microscopy image (AFM), respectively. Finally, I demonstrate a 1300 nm quantum dot laser.

## 2.2 Experiment

The QD samples were grown on (100) $n^+$-GaAs substrate by Veeco Modular Gen II solid-source molecular-beam epitaxy. Two QD layers, one embedded in GaAs layers for PL study and the other one on the surface for AFM study, were deposited in each sample. The detailed structure is shown in Fig. 2.1. The substrate was heated at 600$^o$C. A 300-nm-thick GaAs buffer layer was deposited on the substrate at 600$^o$C. The substrate temperature was then ramped down to 510$^o$C to deposit an InAs QD layer. The nominal thickness of the QD layer was 2.5 monolayers (ML). Different V/III ratios ranging from 35 to 45 were used. After the deposition, there was a 30 sec growth interruption with a continuous flux of $As_2$. A thin $In_{0.15}Ga_{0.67}As$ layer with a nominal thickness of 5 nm was deposited on the InAs QD layer. Different growth methods were used. After the deposition, a 6-nm-thick GaAs layer and a 500-nm-thick GaAs layer were overgrown on the QD layer at 485$^o$C and 600$^o$C, respectively. Finally, the second QD layer with the same procedure was deposited on top of the GaAs layer at 485$^o$C for AFM measurements. No GaAs layers were overgrown on the surface dots. The growth rate of InAs was ~0.1 ML/s, which was determined by observing the reflection high-energy electron diffraction (RHEED) pattern and measuring the 2D (streak) to 3D (spots)

transition time during the deposition of the InAs QD seed layer. For growing the InAs QDs, different growth interruption times are also studied. InAs QDs were grown in the sequence of the following steps: First, I use a relatively high growth rate in order to grow a dense 2 ML QD seed layer. This is followed by a series of growth interruptions (0, 5 and 10 sec.) until the total deposition reaches 2.5 ML. Finally the dots are capped in a 5 nm $In_{0.15}$Ga0.85As strain reducing layer. Surface morphology of the QD samples was carried out by a NanoMan AFM. General lock-in technique was used in our room temperature PL measurement. The luminescence excited by the ~480 nm line of an argon ion laser was dispersed by a SPEX 500M monochromator and then detected by a Ge photodiode. Laser samples with QD active medium was grown on a Si-doped (100) GaAs substrates. The laser structure consists of a 500-nm-thick n-type GaAs buffer layer, a 1.5-μm-thick n-type $Al_{0.6}Ga_{0.4}As$ lower cladding layer, a 500-nm-thick GaAs waveguide layer in which the 7-stack QD active medium is embedded, a 1.5-μm-thick p-type $Al_{0.6}Ga_{0.4}As$ upper cladding layer, and a 300-nm-thick heavily Be-doped GaAs contact layer. In the center of the waveguide are the QD layers. The superlattice barrier is incorporated into the laser heterostructure for improved carrier confinement in the quantum dots. The barrier has an equivalent height is which is greater than that of the barrier material itself. Tunnel injection and p-doping are also incorporated to further improve device performance. The growth temperatures of InAs QDs, InGaAs capping layers, and AlGaAs cladding layers were 510 $^{o}$C, 510 $^{o}$C, and 620 $^{o}$C, respectively. After capping the InAs QDs with InGaAs layer and 7-nm-thick GaAs, the temperature was raised to 600 $^{o}$C to eliminate the dislocation accompanying the formation of the QDs from taking place, which may be formed with formation with QDs [41-42]. The laser structure is shown in Fig. 2.2.

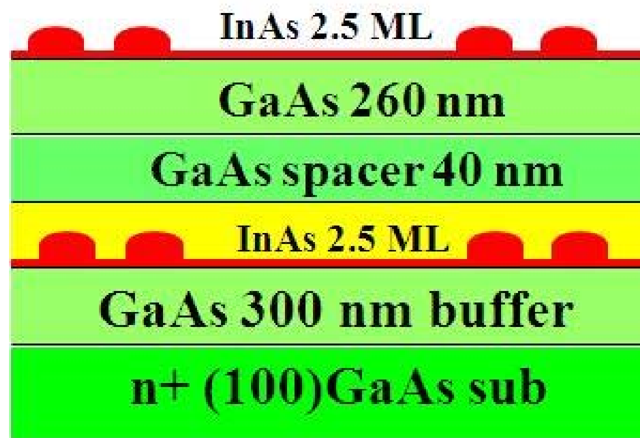


Fig. 2.1 The test quantum dot layer structure.

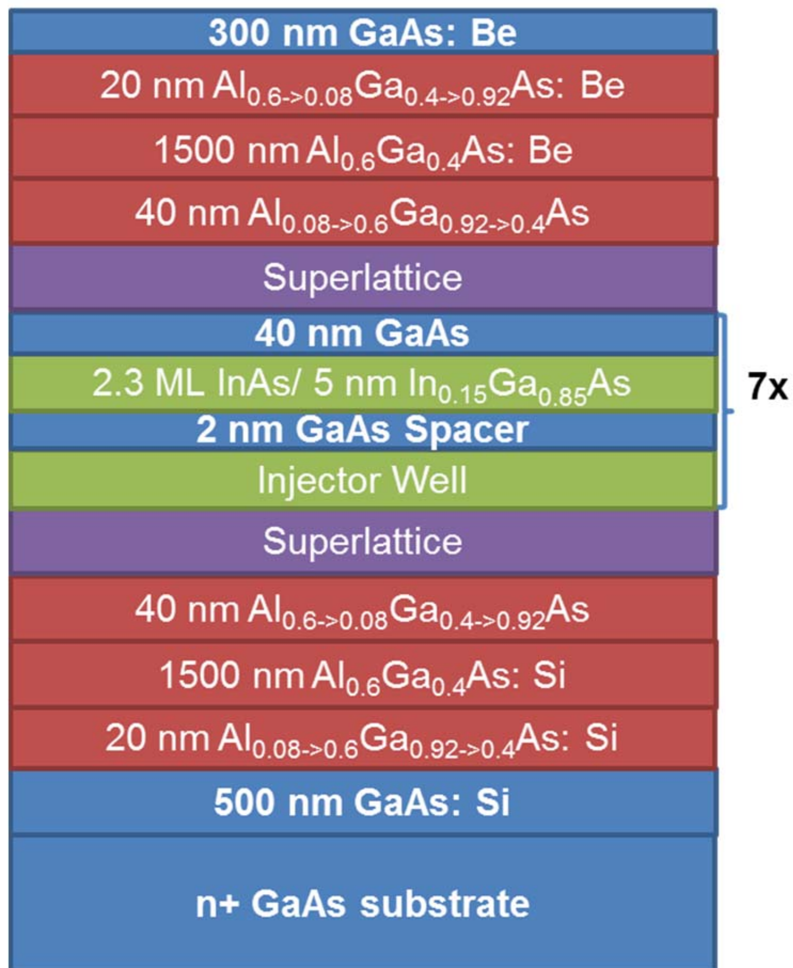


Fig. 2.2 The heterostructure of the quantum dot laser.

## 2.3. Results and Discussion

### 2.3.1 Dependence on V/III Ratio of InAs Quantum Dots

Fig. 2.3 (a) (b) and (c), grown using a relatively high growth rate (~0.1ML/s), show high dot density in all of the samples. Fig. 2.3(c) shows the AFM images of the 2.5 MLs InAs QDs grown at a V/III ratio of 45. Two types of QD, i. e., coherent dot and coalescent dot can be recognized from this AFM picture. The base diameter of the coherent dots and coalescent dots are 25 and 48 nm, respectively. Although the nominal thickness of the deposited InAs is only 2.5 MLs, there is a big size difference between the coherent and coalescent dots due to high V/III ratio. Basically, low V/III ratio may enhance the surface migration length of the In atoms. As V/III ratio is reduced, the enhancement in In surface migration renders the dots with larger diameter and smaller density. The high migration ability also improves the size homogeneity in the QD ensemble and thus significantly suppresses the formation of coalescent dots. When the V/III ratio is larger, the coalescence dot density increases correspondingly.

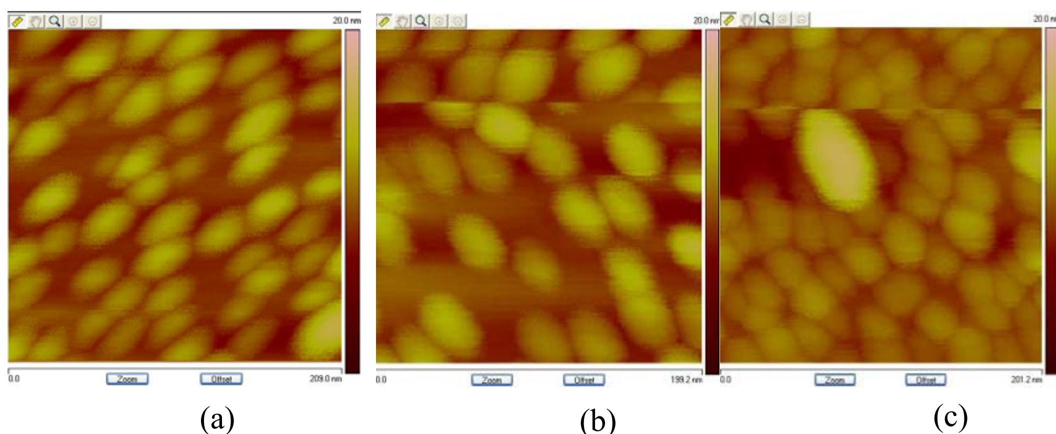


Fig. 2.3 AFM images of 2.5 MLs InAs QDs grown at V/III (a) 35 (b) 40 and (c) 45.

Room temperature PL spectra of the QDs with different V/III ratios are shown in Fig. 2.4. All spectra are dominated by QD luminescence at 1190–1215 nm. The PL intensity of the QDs is obviously enhanced by decreasing the V/III ratio. This verifies the aforementioned migration enhancement of the atoms due to low V/III ratio. The low V/III ratio is also found beneficial to the radiative recombination, which is ascribed to the reduction in the coalescent dot density. Misfit dislocations may be generated during the coalescence of the dots. Further decreases of the V/III ratio will result in the arsenide not being enough to protect the QD. QDs will begin to desorb. The PL linewidth slightly increases.

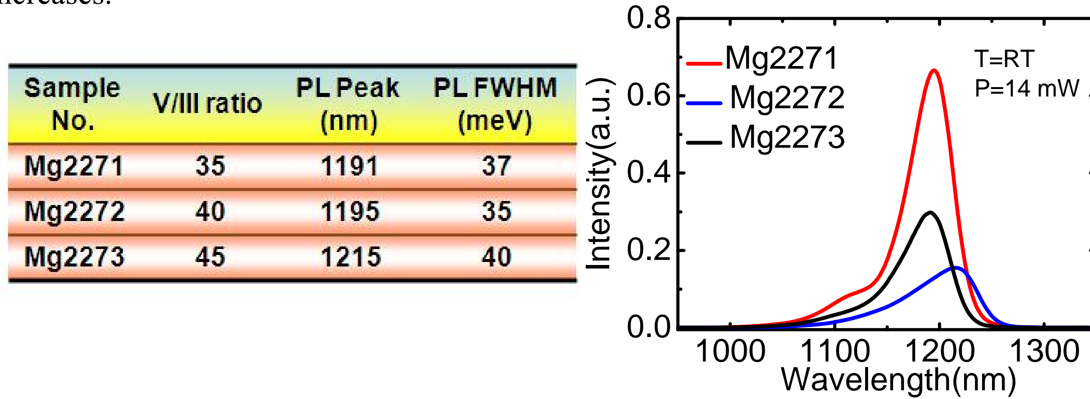

| Sample No. | V/III ratio | PL Peak (nm) | PL FWHM (meV) |
|---|---|---|---|
| Mg2271 | 35 | 1191 | 37 |
| Mg2272 | 40 | 1195 | 35 |
| Mg2273 | 45 | 1215 | 40 |



Fig. 2.4 Room temperature PL spectra of the QDs with different V/III ratio and summarize result in the table 2.1.

### 2.3.2 Dependence on Growth Interruption Time of InAs Quantum Dots

I use a relatively high growth rate to create a dense 2 ML QD seed layer. The relatively small QDs (2ML) will reduce the possibility of forming a coalescent QD. After that, I used growth interruption (GR). The indium atoms could move long distances to the QD seed layer due to the strain which results in more uniform and larger QDs compared with no GR. Further increasing the time of interruption will desorb the QD during this progress. I achieve our target wavelength of 1.22 μm with a very narrow linewidth as shown Fig. 2.5. The AFM images in Fig. 2.6 (a) (b) and (c) show that two step grows results in dense and

uniform QDs with low coalescent QD density in the large area (1μm× 1μm). The QD desorption phenomenon was not revealed in the AFM image with 10 sec growth interruption, possibly due to the fact that I directly cooled down the substrate to grow the surface QDs for an AFM image.

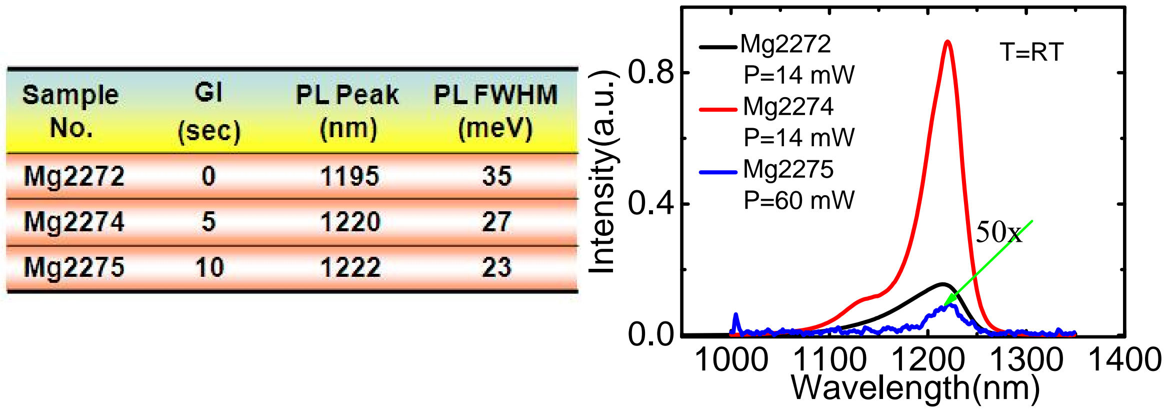

| Sample No. | GI (sec) | PL Peak (nm) | PL FWHM (meV) |
|---|---|---|---|
| Mg2272 | 0 | 1195 | 35 |
| Mg2274 | 5 | 1220 | 27 |
| Mg2275 | 10 | 1222 | 23 |



Fig. 2.5 Room temperature PL spectra of the QDs with different growth interrupt time and summarize result in the table 2.2.

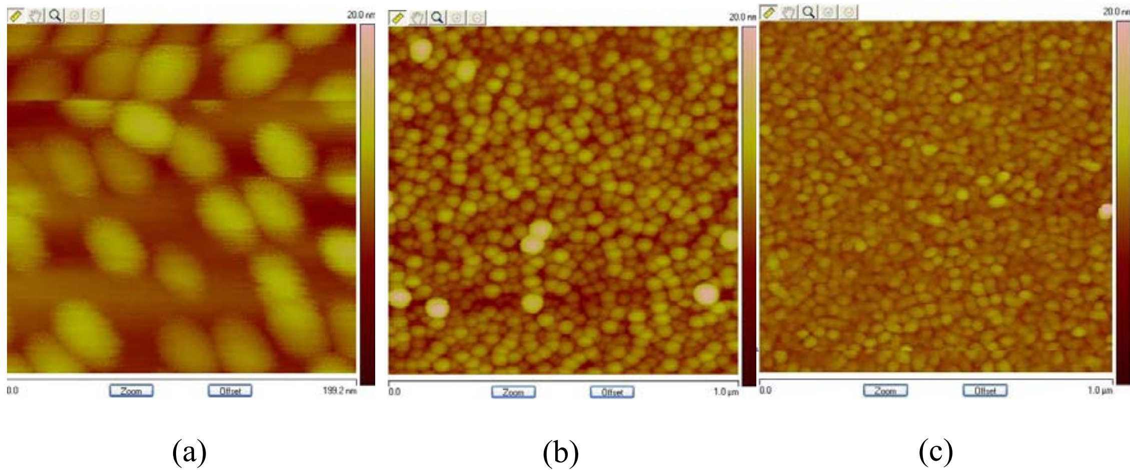


Fig. 2.6 AFM images of 2.5 MLs InAs QDs grown at different interruption time (a) 0 (b) 5 and (c) 10 sec.

### 2.3.3 Tunnel Injection and P-doping in Quantum Dot Lasers – Physics and Technology

The concept of using tunneling injection in semiconductor lasers to alleviate hot carrier problem and enhance modulation speed was proposed by Bhattacharya, et al. and demonstrated for the first time in quantum well lasers [43]. In the case of self-organized In(Ga)As QDs which are formed on a two-dimensional wetting layer during epitaxy [44], the wetting layer and the localized QD states form an electronically coupled system. In a conventional SCH semiconductor laser, carriers injected into quantum well/dots will not only fill the ground state, but also thermal heating forces more carriers to stay at higher energy and eventually leak into the adjacent layers. Such systems cannot be described by equilibrium quasi-Fermi statistics [45]. This leads to a hot carrier problem in QD lasers, inducing gain compression and degrading high-speed performance [46-48]. The hot carrier distribution also increases undesirable parasitic recombination outside of the QDs [49-50], resulting in increased temperature dependence of the threshold current and output slope efficiency.

This problem can be alleviated by tunneling "cold" electrons into the lasing states of quantum-well/dots from an adjacent injector layer, as shown in Fig. 2.7. Using this technique, cold carriers (electrons) are injected into the lasing states from an adjacent injector well through a tunnel barrier by phonon-assisted tunneling. Thereby, both the carrier heating in the active region and carrier leakage into the optical confinement layer are minimized. The only requirement is that the tunneling rate should be less than/or comparable to the lasing emission rate. DT spectroscopy measurements confirm the tunnel injection time to be $<2$ ps in TI-QD/QW laser heterostructures with temperature insensitivity. Enhanced modulation bandwidth and reduced Auger recombination and

chirp were demonstrated in TI-quantum well lasers [50-51]. Efficient tunneling of electrons from the injector well into the dots has been confirmed by femtosecond differential transmission spectroscopy measurements, which show an extremely fast tunneling time, ~ 1.7 ps [45]. Experiments showed QD TI lasers exhibit small-signal-modulation frequency up to 30GHz, chirp < 0.1 Å, and nearly-zero α-factor, etc.

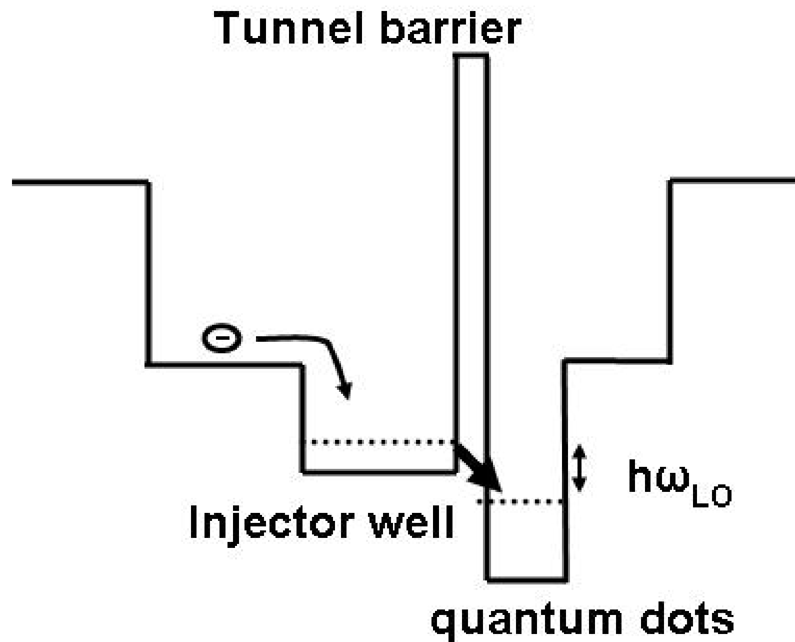


Fig. 2.7 Schematic of a tunneling injection (TI) quantum dot.

The energy separation of the hole states in QDs is less than the phonon energy, which induces thermal broadening of the hole distribution and temperature-sensitive operation. P-doping of the quantum dots [49] can provide excess holes to fill the ground state at high temperatures, as illustrated in Fig. 2.8. The energy separation of the hole states in the QDs is less than the phonon energy, which induces thermal broadening of the hole distribution and temperature-sensitive operation. The excess holes provided by

*p*-doping ensures that the hole ground states are filled and less injected electrons are needed for population inversion [49, 52]. Thereby, both the gain and the differential gain will increase, and the gain saturation associated with the thermal broadening of injected hole is reduced. *P*-doping also form a natural barrier to help reduce the number of holes which escape and leak into the GaAs barrier layer, which further reduces undesirable carrier recombination loss outside of the QDs.

P-doping in QDs is achieved either by direct doping or modulation doping. Considering the relatively-low dot density and the discrete energy levels in QDs, the optimum p-doping levels are ~$5.0 \times 10^{11}$ $cm^{-2}$, due to the low dot fill factor and the discrete energy levels in QDs. The excess holes provided by p-doping can occupy the wetting layer states, which can severely limit the potential benefits of this technique [53]. Additionally, p-doping can significantly enhance Auger recombination in QDs, which increases the threshold current [15].

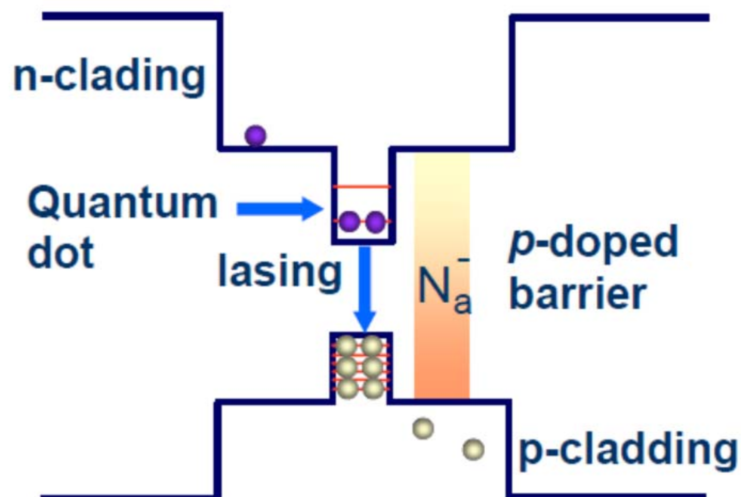


Fig. 2.8 Schematic of p-doped quantum dot.

### 2.3.4 Quantum Dot Lasers

Fig. 2.9 (a) shows the L-I-V curve of a laser with 7-stack QDs grown by MBE. The laser is 740 μm long and was driven under continue wave (CW) biasing with lasing at 1304 nm, with the L-I-V shown in Fig. 2.9 (b). The threshold current and external quantum efficiency of this laser are 23 mA and 57%, respectively. The measured temperature dependence of $I_{th}$ and $\eta_d$ are shown on Fig. 2.9 (c) from which values of $T_0$ and $T_1 \sim\infty$ in the temperature range of 5-60 $^o$C is observed. Between 60-85$^o$C, $T_0$= 90 K and $T_1$=280 K. Traditionally, in InGaAs/InP double heterostructure1.3 um lasers, $T_0$ is ~50 K. This encouraging result demonstrates why quantum dot lasers have become the best candidate for an optical interconnection source, especially when considering the temperature stability viewpoint.

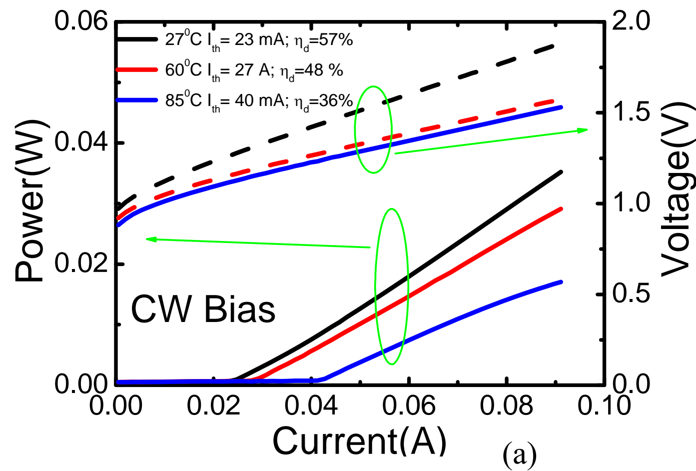


(a)

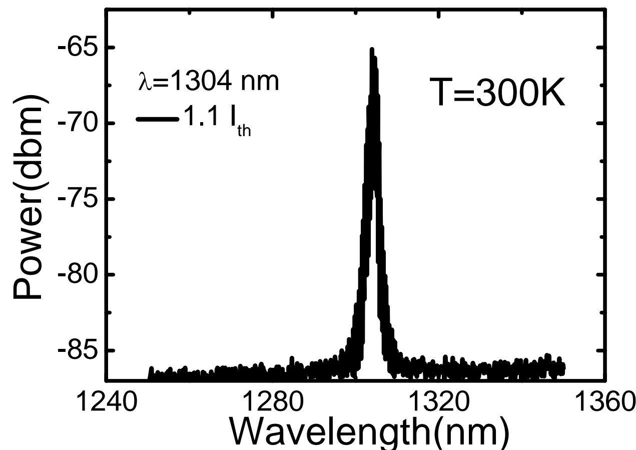

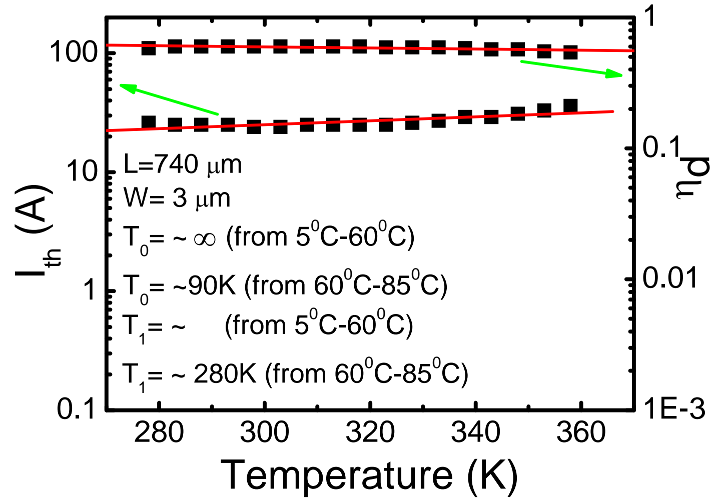


Fig 2.9 (a) L-I-V measurements under CW biasing. (b) EL spectra (c) Temperature dependence of $J_{th}$ and the characteristic temperature, $T_0$ and temperature dependence of $\eta_d$ and $T_1$ for each laser.

## 2.4 Conclusions

I report the effect of the growth conditions on the structural and optical properties of $InAs/In_{0.15}Ga_{0.85}As$ QDs. For the 2.5 ML core InAs QDs, I found that low V/III ratio (40) can drastically suppress the formation of coalescent dots and hence improve the optical quality. The deposition of $In_{0.15}Ga_{0.85}As$ on the core InAs QDs enlarges the average diameter of the QDs and results in a red-shift on the PL spectrum. The peak wavelength is as long as 1304 nm. I use a novel two step growth technique. First, I use a relatively high growth rate in order to grow a dense 2 ML QD seed layer. The relatively small QDs (2 ML) will reduce the possibility of forming coalescent dots. This is followed by a series of growth interruptions until the total deposition reaches 2.5 ML. I calibrated the growth interruption time and found that 5 seconds was the best time to use. Finally, a 7-QD-stack laser with the best growth conditions was designed and fabricated. Superlattice barrier,

p-type modulation doping and tunnel injection are incorporated into the active region to further improve the device performance was grown and fabricated. The as-cleaved 740 μm long ridge waveguide laser demonstrates an emission wavelength of 1304 nm and a threshold current density of 23 mA under CW biasing and the measured temperature dependence of $I_{th}$ and $\eta_d$, from which values of $T_0$ and $T_1 \sim\infty$ in the temperature range of 5-60 $^oC$ is observed. Between 60-85$^oC$, $T_0$= 90 K and $T_1$=280 K. The obtained laser performance indicates the good material quality of the $InAs/In_{0.15}Ga_{0.85}As$ QDs.

# Chapter 3

## High Speed 1.22 μm Tunnel Injection p-doped Quantum Dot Excited State Laser

### 3.1 Introduction

Semiconductor lasers emitting at 1.3 μm are attractive for use in metro-loop transmission links over short and medium range distances. In particular, relatively low threshold current, very high $T_0$ and near-zero chirp and α-factor have been demonstrated with 1.3 μm lasers which incorporate self-organized InAs quantum dots (QDs) in the active region [54-60]. A general problem with long wavelength lasers is that the gain and differential gain tends to be lower than those in shorter wavelength (e.g. 0.8 – 1.0 μm) lasers [17,61]. One of the consequences of this is a lower small-signal modulation bandwidth [61]. Self-organized QDs which emit at 1.3 μm have larger size and smaller aerial density than those which emit at 1.0 μm. As a result, their gain is smaller [17,61]. Furthermore, the optical matrix element of InAs QDs, typically used in 1.3 μm lasers, is ~ 30% smaller than the matrix element of $In_{0.4}Ga_{0.6}As$ QDs incorporated in 1.0 μm lasers [61]. Consequently, a small-signal modulation bandwidth of ~25 GHz has been measured in directly modulated in 1.0 μm QD lasers [17], while the measured bandwidth of 1.3 μm QD lasers is considerably smaller [17;57-63].

Nearly all quantum dot lasers that have been experimentally demonstrated, and are in use, emit light resulting from ground state transitions in the quantum dots. Because of the symmetry of the quantum dot geometry, the excited state (ES) level in each dot has a

twofold degeneracy [64-65]. It has been shown theoretically that a 1.3 μm QD laser with emission resulting from ES transitions can have a larger modulation bandwidth, compared to that from ground state (GS) lasing [66-68]. The challenges, however, are the design of the active region and the materials considerations involved in the growth of QDs which have excited state emission at 1.3 μm. Some reports on excited state lasing from QDs have been made [67]. In the present study, I have investigated the design, fabrication, and characterization of high-performance lasers in which lasing occurs as a result of excited state $e_1 - hh_1$ transitions and electrons are transported to the excited state by longitudinal optical (LO) phonon-assisted tunnel injection [57, 69]. Lasing from the excited state is ensured by coating one of the facets of the Fabry-Pérot cavity with a dielectric mirror which provides high reflectivity at the excited state emission wavelength and much lower reflectivity at the ground state emission wavelength. The peak wavelength of ES lasing is 1.22 μm. A high differential gain of 1.1 x $10^{-15}$ $cm^2$ and a small-signal modulation bandwidth of 13.5 GHz have been measured.

### 3.2 Experiment

The QD laser heterostructure grown by molecular beam epitaxy on (001)-Si-doped GaAs substrate is shown in Fig. 3.1 (a). One period of the QD tunnel heterostructure is shown in the inset and consists of a 5 nm $In_{0.2}Ga_{0.8}As$ injector, a 10 nm GaAs tunnel barrier and 2.3 monolayers of InAs quantum dots in a $In_{0.15}Ga_{0.85}As$ well (dot-in-a-well heterostructure). The thickness of these layers are first estimated from a calculation of the QD bound states using an 8-band $\boldsymbol{k} \cdot \boldsymbol{p}$ model (with the strain described by the valence force field model) [70-72], and then the heterostructure design is fine-tuned using

photoluminescence measurements as a feedback. The quantum dots are modulation doped p-type at a level of 5 x $10^{17}$ $cm^{-3}$ to maximize the differential gain [61, 52]. The active region consists of 7 QD layers with tunnel barriers and 50 nm GaAs spacer layers between them. The GaAs waveguide region is surrounded by n- and p-type step-graded AlGaAs cladding layers in the bottom and top of the waveguide and highly doped GaAs contact layers. The QD layers are grown at 530$^{o}$C at a rate of 0.08 monolayers/sec. The thin $In_{0.15}Ga_{0.85}As$ layers, which form the matrix in which the dots are immersed, also serve as strain engineering layers to tune the output emission peak wavelength. The GaAs layers on top of the dot/well heterostructure serve to smoothen the growth front. Each dot layer is annealed at 600$^{o}$C for 3 minutes in the growth ambient before growth is continued.

Fabrication of ridge waveguide lasers was accomplished by standard photolithography, dry etching and ohmic contact metallization techniques. The ridge width is 3 μm and the length, obtained by cleaving, varies from 480 to 2600 μm. One facet of the laser, with 480 μm cavity length, was coated with a high reflectivity distributed Bragg reflector (DBR) mirror consisting of 6 pairs of $ZnSe/MgF_2$ layers. The simulated reflectivity spectrum is shown in Fig. 3.1 (b). The center of the pass band of the DBR is tuned to 991 nm, such that 1.224 μm (ES) and 1.3μm (GS) reflectivities are 91 and 45%, respectively. These emission wavelengths correspond to the peaks of the ES and GS emission in the measured room temperature photoluminescence spectrum, shown in Fig. 3.2. Thus a high reflectivity is maintained for ES emission while that for GS emission is considerably lowered. It should be noted that the linewidth of the GS emission wavelength is only 27 meV due to the filtering action in the presence of the tunnel heterostructure, which injects electrons in QDs with a more homogeneous size distribution [45].

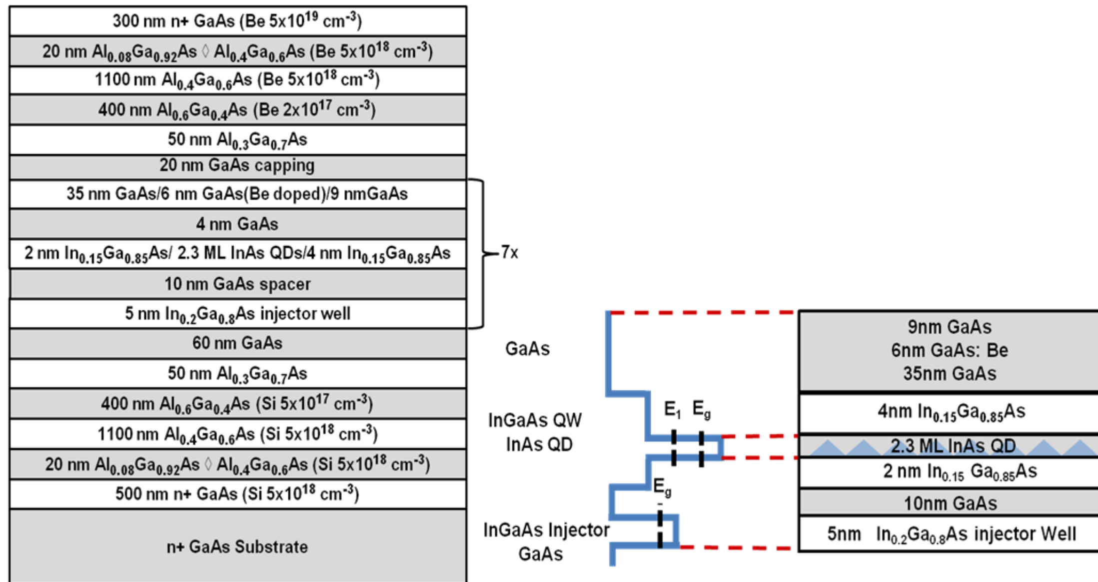


(a)

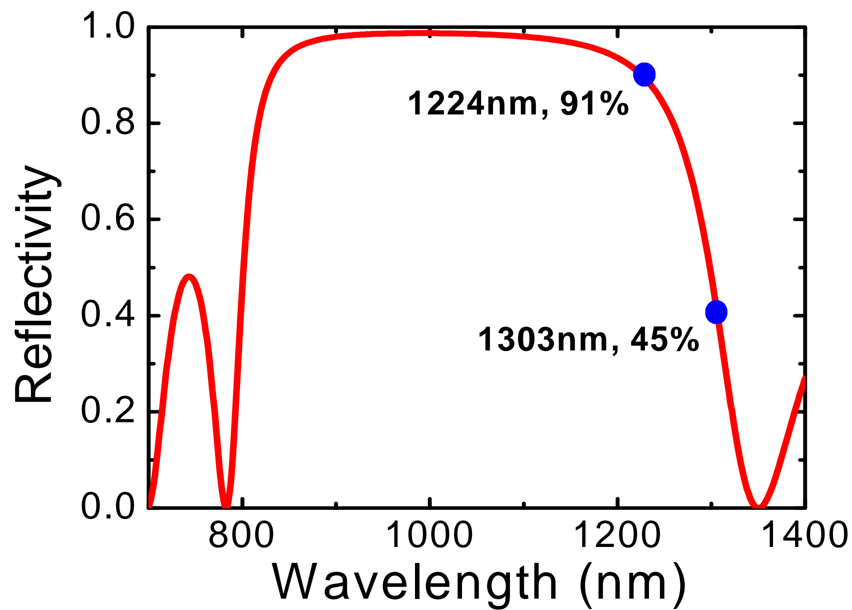


(b)

Fig. 3.1 (a) The heterostructure of the quantum dot laser (b) The reflectivity of the HR coating showing the reflectivity at the excited state (91%) and at the ground state (45%) simulated by transfer matrix method.

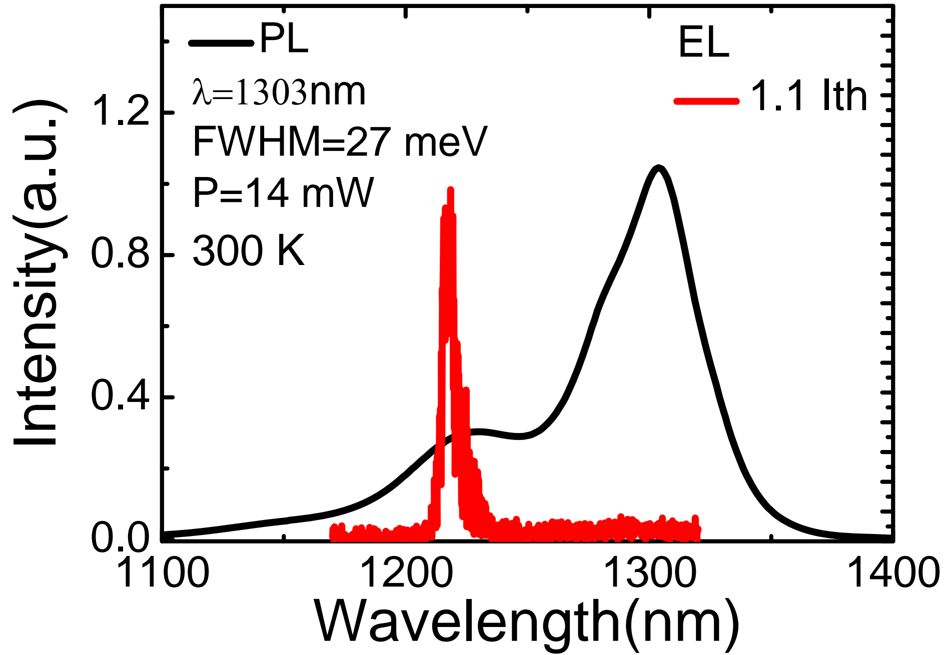


Fig. 3.2 Measured photoluminescence and lasing spectra

**3.3 Results and Discussion**

The steady state characteristics of the lasers were measured under pulsed bias condition (4 µm pulse width, 500 Hz repetition rate). The lasing emission spectrum for I = 38 mA is also shown in Fig. 3.2. The peak is observed at λ ≅ 1.22 µm. Further tuning of the QD heterostructure and growth conditions are necessary to shift the ES lasing peak to 1.3 µm. The light-current characteristics for the laser with cavity length 480 µm and with facet coating are shown in Fig. 3.3. The threshold current and external quantum efficiency for emission from one facet are 34 mA and 46 %, respectively. The relatively high value of the threshold current is attributed to two factors: p-doping of the dots which enhances the rate of non-radiative Auger recombination [73], and the required occupation of the ground states before the excited states can be filled.

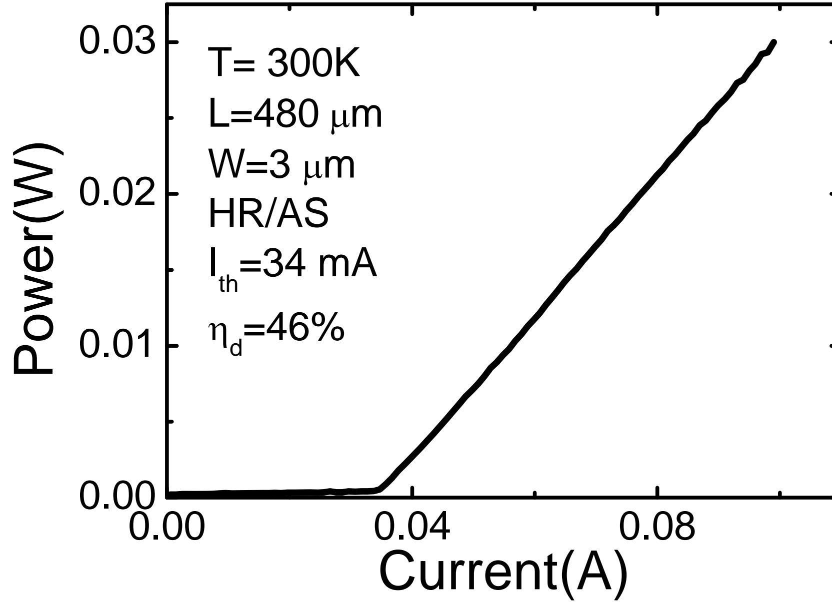


Fig. 3.3 Measured light-current (L-I) characteristics.

Similar L-I measurements were made on lasers with cavity lengths varying from 480 to 2600 μm and without any facet coating (R ~ 0.32). A plot of the inverse differential quantum efficiency $\eta_d$ versus cavity length, obtained from the measurements, is shown if Fig. 3.4 (a). Lasing is observed from the ground state for devices with larger values of cavity length and the data of Fig. 3(a) can be analyzed with the equation:

$$\frac{1}{\eta_d} = \frac{1}{\eta_i}\left(1 + \frac{\alpha_i L_c}{\ln(1/R)}\right) \tag{3.1}$$

where $\eta_i$ is the internal quantum efficiency, $\alpha_i$ is the cavity loss, and $\alpha_m$ is the mirror loss. Values of $\eta_i$ and $\alpha_i$ equal to 80% and 1.9 $cm^{-1}$, respectively, are obtained for ground state lasing from the fit to the data. For shorter cavity lengths, lasing takes place at λ=1.22 μm from the excited states. The measured values of $\eta_d$ decreases sharply, and the values of 1/

$\eta_d$ versus L do not follow the trend dictated by Eqn. 3.1. In short-cavity lasers the mirror loss increases, more carriers are required to provide optical gain and $\alpha_i$ also increases due to increases in free carrier absorption. Consequently, the threshold gain also increases and $\alpha_i$ will be a function of cavity length [59]. Figure 3.4 (b) depicts plots of threshold modal gain ($\alpha_i + \alpha_m$) versus threshold current density for GS and ES lasing, obtained from measurements on lasers with different cavity lengths. As mentioned earlier, $\alpha_i$ is constant for ground state lasing. For excited state lasing $\alpha_i$ is calculated for each cavity length using Eqn. 1 where $\eta_i$ is replaced with $\eta_i^*$, which is calculated following the method outlined in Zhukov, et al. [74] and is found to be 78%. The data are fitted to the empirical relation [75]:

$$g_{mod}=g_{sat}\{1-\exp[-\gamma(Jth-Jtr)/Jtr]\} \quad (3.2)$$

plotted as the solid curves in Fig. 3.4 (b), where $g_{mod}$ is the modal gain, $g_{sat}$ is the saturation modal gain, $J_{tr}$ is the transparency current density, and $\gamma$ is a non-ideality factor. The values of $g_{sat}$ for GS and ES lasing are 22 $cm^{-1}$ and 56 $cm^{-1}$, respectively. The ratio of the two values is ~2.5, which is well within the range of 2-3 [64-65, 75]. The gain per dot layer is 8 $cm^{-1}$. Similarly, the value of $J_{tr}$ for the excited state is nearly a factor of 2 larger than that of the ground state. The differential gain of the laser is determined from the relation:

$$J_{th} = J_{tr} + \frac{qd}{\Gamma \eta_i * \tau_e \frac{dg}{dn}}[\alpha_i + \alpha_m] \quad (3.3)$$

where d is the active region thickness, $\tau$ is the carrier lifetime in the excited state, and $\Gamma$ is the confinement factor. The differential gain is calculated for lasers of different cavity lengths and an average value of 1.1x $10^{-15}$ is obtained, assuming $\tau$ = 0.5 ns in the excited state for quantum dots with p-doping [76].

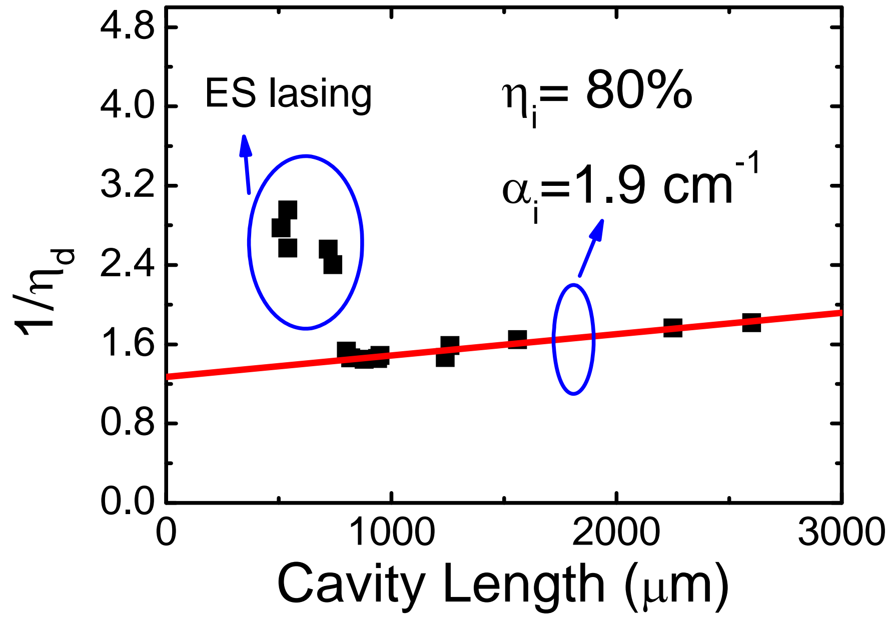


(a)

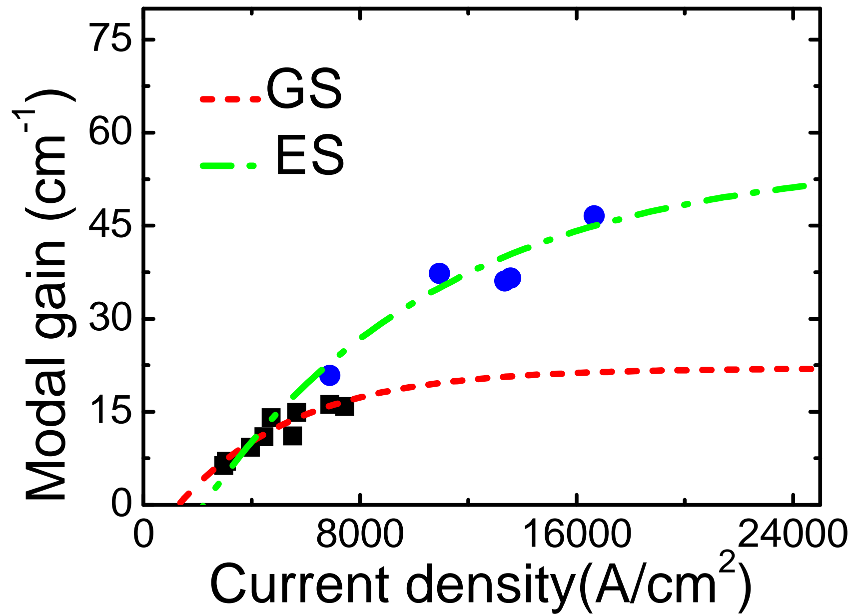


(b)

Fig. 3.4 (a) Cavity length dependence of external quantum efficiency; (b) modal gain vs current density from which a ground state modal gain of 22 $cm^{-1}$ and an excited state modal gain of 56 $cm^{-1}$ are derived.

Small-signal modulation measurements were made with the laser with high reflectivity facet coating and cavity length of 480 μm under pulsed biasing condition. The measurements have been described previously [17] and were made using a pulse generation, rf sweep oscillator and a bias tee for small signal biasing, high speed photodetector, low noise amplifier, and a electrical spectrum analyzer. The modulation-response characteristics for different levels of injection are shown in Fig. 3.5. Excited state lasing at ~ 1.22 μm is confirmed for all the injection currents. A modulation bandwidth, $f_{-3dB}$ = 13.5 GHz is measured for I = 4.5 $I_{th}$. This suggests that a similar device could be used for 20 Gb/s data transmission with a bit error rate of $<10^{-11}$. The measured bandwidth is larger than those previously reported for 1.3 μm QD lasers with emission from the ground state [17, 57-63]. I believe the larger modulation bandwidth results from the enhanced saturation modal gain in the excited states and due to the incorporation of tunnel injection [57]. The modulation bandwidth for ES lasing has been calculated as a function of $\tau_{21}$, the ES-GS carrier relaxation time and QD size fluctuation. [66] I have measured $\tau_{21}$ ~ 1 ps by differential transmission spectroscopy in $In_{0.6}Ga_{0.4}As$/ GaAs QDs [45]. The size fluctuation of the 1.3 μm QDs in our laboratory is estimated to be ~ 15%. For these values of the two parameters, our measured bandwidths are in excellent agreement with the calculated data. Finally, a comment is made regarding the peak of the modulation response. It is observed that with increase of injection current, the peak moves to higher frequencies, as expected, but the peak value is enhanced and so is the width. The characteristics are similar to those observed by Stevens, et al. [67]. Interdot coupling, which will cause level splitting, is more efficient among the QD excited states. Together, with the inhomogeneous broadening due to size fluctuation and the twofold degeneracy,

there will be an efficient dynamic redistribution of carriers among dots with increasing injection. This can effectively broaden the width of the resonance and can also reduce gain compression effects. It is also evident that the response, which is representative of the transfer function ΔP/ΔJ, has multiple poles, which can also result from dots of differing size. Further experiments are, of course, necessary to confirm these effects.

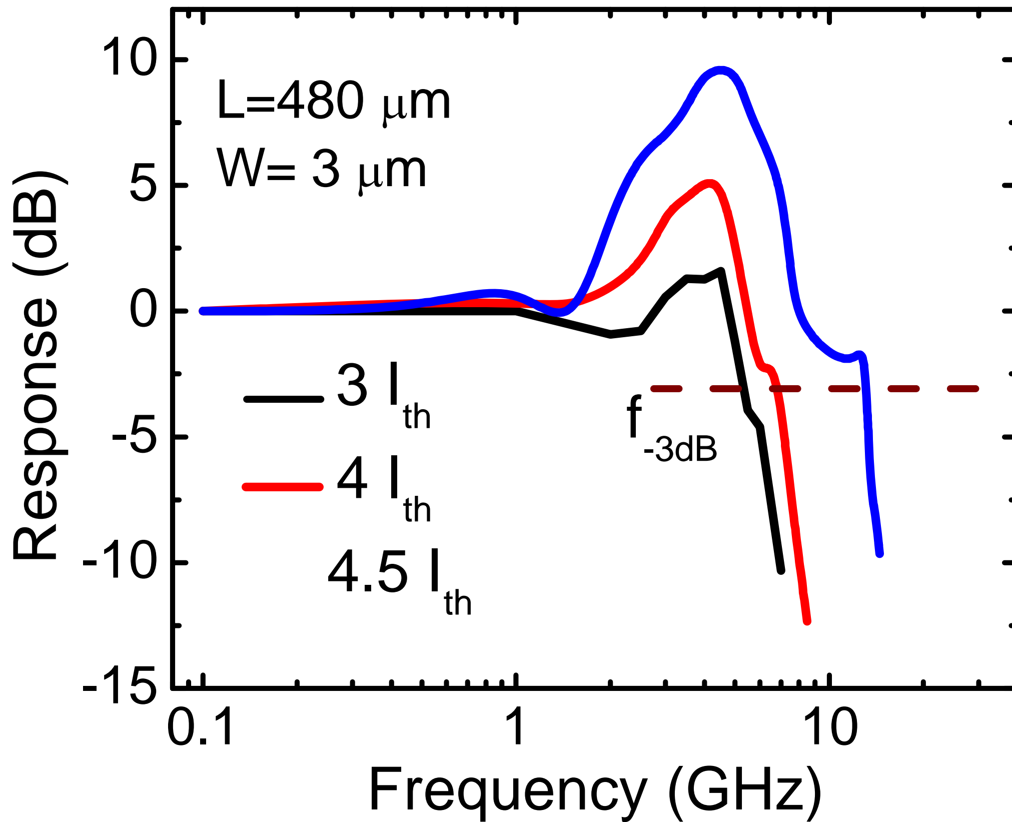


Fig. 3.5 Measured small-signal modulation response for excited state lasing. A maximum modulation bandwidth ($f_{-3dB}$) of 13.5 GHz is measured.

### 3.4 Conclusions

In conclusion, excited state lasing is unusual in QW lasers. Once lasing has started in QW lasers, the very fast stimulated recombination time consumes all further injected

carriers and the quasi-Fermi levels are pinned at the energy where the oscillation beings. This Fermi level pinning prohibits lasing at higher transition energies. However, in QD lasers, it is generally believed that the relaxation for carriers from the excited state into the ground state can be a bottleneck as the device is lasing is in the ground state and the ground state is in saturation. The finite time constant restricts the light output of the ground state and the carriers pile up the excited state, resulting in excited state lasing.

I report the characteristics of excited state lasing at 1.22 μm in InAs quantum dot lasers on GaAs. A high-reflectivity facet coating with appropriate reflectivity characteristics is used to suppress ground state emission and tunnel injection into the excited states and p-doping of the dots are incorporated to optimize device performance. The excited state saturation modal gain is 56 $cm^{-1}$ and small signal modulation bandwidth is 13.5 GHz.

# Chapter 4

# Quantum Dot Multichannel and Comb Lasers

## 4.1 Introduction

An optical source for dense wavelength division multiplexing (DWDM) is deemed to be important for future silicon photonics being developed for computing applications. An array of tunable distributed feedback (DFB) lasers is complex and expensive due to the large number of lasers involved, the difficulty in realizing precise gratings for equally spaced wavelengths, and the need for epitaxial regrowth. An alternative is the growth of a chirped quantum dot structure, which allows for the emission wavelength to be changed by varying the cavity length. These multichannel lasers have different types of QDs, and by varying the cavity length, the energy levels will have different threshold modal gains, thus generating light emission at different wavelengths [79-80]. Another alternative to using an array of DFB lasers is to utilize the highly uniform longitudinal modes of a single Fabry-Pérot laser wherein the mode spacing can be varied by altering the cavity length. Such multi-wavelength emitters or comb lasers need to satisfy several conditions [81-84]. First, the active medium should display a uniform and broadband gain spectrum with a sufficiently large value of gain to enable lasing in the entire desired wavelength range. The second requirement is temperature stability of the output. Such a multi-wavelength laser will have additional applications in sensing, metrology, spectroscopy, and optical

coherence tomography [85-86]. I design, fabricate, and characterize both multichannel and comb lasers.

## 4.2 Experiments

### 4.2.1 Multichannel Lasers

The multichannel QD laser heterostructure was grown on a (001) n+-GaAs substrate by (Varian Gen-II) solid-source molecular-beam epitaxy, as shown in Fig. 4.1 (a). The general laser structure consists of a 500-nm-thick n-type GaAs buffer layer, a 1500-nm-thick n-type $Al_{0.6}Ga_{0.3}As$ lower cladding layer with a doping concentration varying from $5x10^{17}$ to $5x10^{18}$ $cm^{-3}$, a 150-nm-thick GaAs waveguide layer where the QD active medium is embedded, a 1500-nm-thick p-type $Al_{0.6}Ga_{0.4}As$ upper cladding layer with a doping concentration varying from $2x10^{17}$ to $5x10^{18}$ $cm^{-3}$, and a 300-nm-thick heavily Be-doped ($5x10^{19}$ $cm^{-3}$) GaAs contact layer. The active region contains 8 QD layers. For each QD layer, 2.3 ML InAs was grown in an $In_{0.2}Ga_{0.8}As$ well (dot-in-a-well) with a single barrier tunneling heterostructure. The growth temperature and growth rate were 530 $^{o}C$ and 0.08 ML/s, respectively. An InGaAs strain-reducing layer was then grown at 490 $^{o}C$ with varying thicknesses to obtain different energy levels. P-type modulation doping of the QDs was added in each layer with beryllium at a concentration of $1\times10^{18}$ $cm^{-3}$. In order to test this simple and novel idea, I grew the laser heterostructure shown on the Fig. 4.1 (b) including 3 stacks of 1.2 μm InAs QDs and 5 stacks of 1.05 InGaAs μm QDs, as shown on the PL measurement. I wanted to make sure that the tuning to the different lasing wavelengths was due to the different stacks and not the inhomogeneous broadening. After the growth of the entire laser structures, standard photolithography, dry

etching, and metallization processes were used to fabricate 5μm wide as-cleaved ridge waveguide lasers.

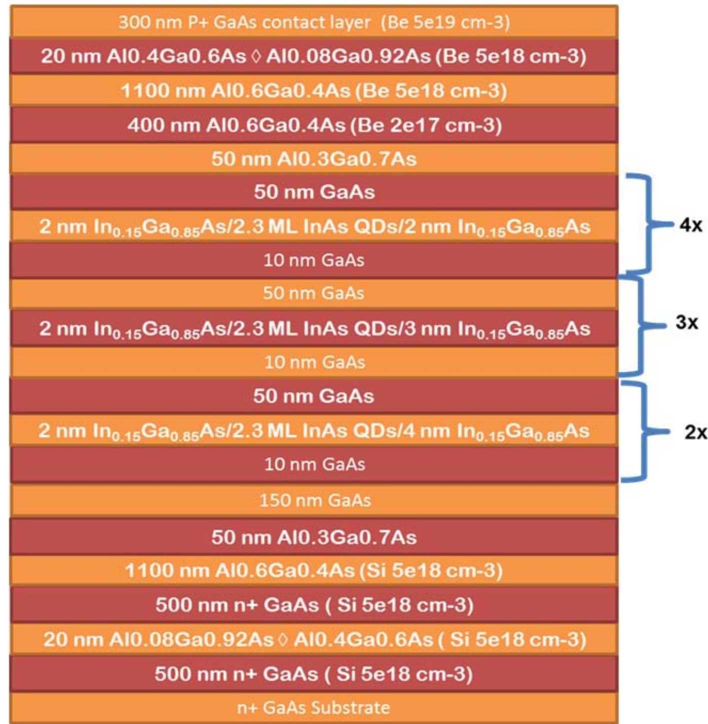


(a)

(b)

Fig. 4.1 Heterostructure of the QD laser (a) three different types of QD in 1.3 μm (b) 3 stacks of 1.2 μm InAs QDs and 5 stacks of 1.05 μm InGaAs QDs.

### 4.2.2 Comb Lasers

Self-organized quantum dots (QDs) can be used as the gain media in comb lasers, since the naturally occurring size distribution of the QDs during epitaxy enables the realization of wide luminescence and gain spectra. I report here the characteristics of a 1.3 μm quantum dot comb laser with an electroluminescence linewidth of 75.9 nm achieved by variations in molecular beam epitaxy (MBE) techniques. Tunnel injection of electrons [45, 87] and p-doping of the quantum dots [17, 61] are incorporated in the design of the active region to enhance the gain, differential gain and temperature stability of the multi-wavelength laser.

The quantum dot comb laser heterostructure, grown by MBE on (001) GaAs substrate, is shown in Fig. 4.2. The active region contains 8 quantum dot layers. Each layer consists of InAs quantum dots grown in a $In_{0.2}Ga_{0.8}As$ well (dot-in-a-well) and a single barrier tunneling heterostructure. In order to achieve 1.3 μm emission, a 2.5 monolayer (ML) InAs QD layer was grown at 530 $^{o}$C atop a 1 nm $In_{0.2}Ga_{0.8}As$ layer, and the QDs were capped with an $In_{0.2}Ga_{0.8}As$ strain reducing layer grown at 490 $^{o}$C. To obtain the broadest possible emission, the 8 QD layers were divided into three groups having various thicknesses of the $In_{0.2}Ga_{0.8}As$ capping layer: the first 3 QD layers with a 1.8 nm capping layer, the next 3 QD layers with 1.5 nm, and the last 2 QD layers with a 1.2 nm capping layer. *In-situ* annealing under $As_2$ overpressure before and after QD formation was also performed to enhance QD size inhomogeneity. P-type modulation doping of the quantum dots in each layer is done with beryllium with a concentration of $1\times10^{18}$ cm$^{-3}$. Separate confinement heterostructure (SCH) ridge waveguide lasers were fabricated by standard photolithography, dry etching, contact metallization and cleaving techniques. The ridge width is 5 μm and the cavity

length varies from 650-2300 μm. All the measurements reported here are with the laser facets uncoated (as-cleaved).

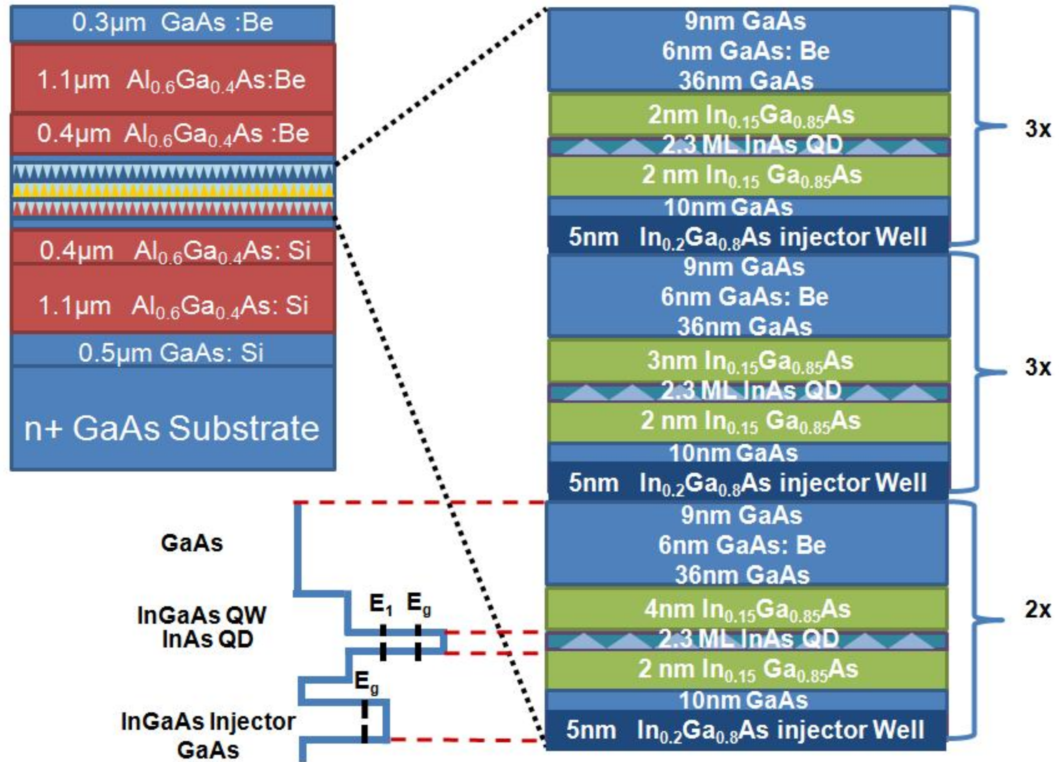


Fig. 4.2 The heterostructure of the quantum dot comb laser with band diagram of one period of tunnel injection QD active region

### 4.3 Results and Discussion

#### 4.3.1 Multichannel Lasers

I intentionally grew a QD laser structure with different dot sizes and different numbers of stacks to create different energy levels and modal gains for each type of QD. The modal gain of a QD laser is proportional to the dot density and density of states, which itself is inversely proportional to the average volume of individual dots. The differences in size and in the number of stacks cause the gain and modal gain to decrease in the larger QDs [17].

Lasers of various lengths were fabricated as follows: laser 1 (L=2400 μm), laser 2 (L=2060 μm), laser 3 (L=1100 μm), and laser 4 (L=980 μm). The following equation is well known:

$$\alpha_m = \frac{1}{2L_c}\ln(\frac{1}{R_1 R_2}) \tag{4.1}$$

where $\alpha_m$ is the mirror loss, $L_c$ is the cavity length, and $R_1$ and $R_2$ are the facet reflectivity assumed to be 0.32. I can easily change the lasing wavelength in this chirp laser structure by varying the cavity length of the laser. The room temperature electroluminescence (EL) spectra of these three lasers are shown in Fig. 4.3 (a). Their emission wavelengths are at 1278, 1274, 1271, and 1267 nm, respectively, indicating that the oscillations in these lasers all commence in the ground state of the QDs. The carriers fill the states in the QDs in the following manner. The carriers first fill the states in the largest QDs due to the lower energy level. After overcoming the total loss, the laser begins lasing at this lowest energy level. However, the largest QDs have the least gain, and they have fewer stacks, which only allow them to overcome the loss at the longest cavity length. Conversely, laser 4, which has the shortest cavity length, can only lase with the smallest QDs, which have more stacks and a higher modal gain. Although each QD has a δ-function-like density of states, the size inhomogeneity is broader than that of a single QD. Therefore, some lasing wavelengths can occur at specific cavity lengths, indicating that the gain media can reach oscillation at the shoulder of the density-of-state distribution function. For this reason, I successfully demonstrated a four-channel laser array with near equal spacing (~5 nm). Fig. 4.3 (b) shows the room temperature light current (L-I) characteristics measured with the continuous-wave (CW) biasing of lasers 1, 2, 3, and 4. The threshold current of these four lasers is 56, 47, 39, and 35 mA, with external quantum efficiencies of 32%, 34%, 44%, and 43%, respectively. It is worthwhile to mention that this observation is different from a

uniform-stacked multilayer QD active region that simultaneously lases in the GS and the ES.

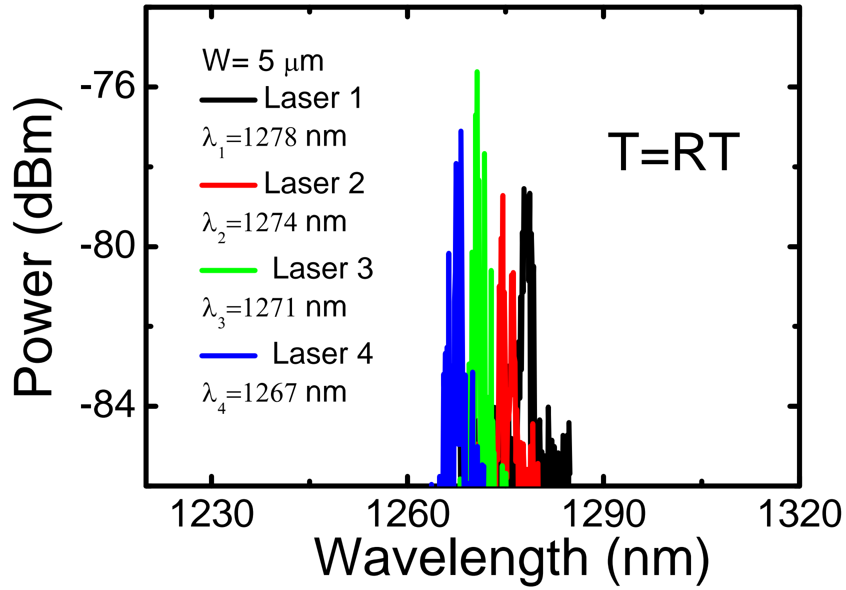


(a)

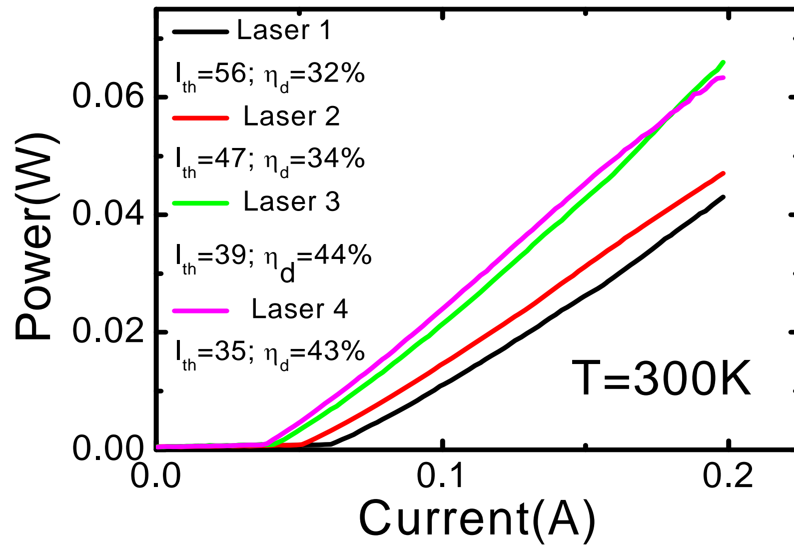


(b)

Fig 4.3 (a) Electroluminescence spectrum of the four channels at room temperature; (b) L-I measurements of the four lasers under CW biasing.

From the testing sample which includes 3 stacks of 1.2 μm InAs QDs and 5 stacks of 1.05 μm InGaAs QDs. By tuning the mirror loss of the laser (by varying the cavity length), I successfully achieved three different light emission wavelengths using the same heterostructure. These emission wavelengths are related to the GS and 1$^{st}$ ES of the InAs QDs, and GS of the InGaAs QDs as shown in the PL and EL spectrum in the fig. 4.4 (a). Due to the use of excited state lasing, the threshold currents are quite variable in this laser array as shown in fig. 4.4 (b). I can tune lasing wavelength over a large range (~120 nm) and potentially and tune from T band to O band.

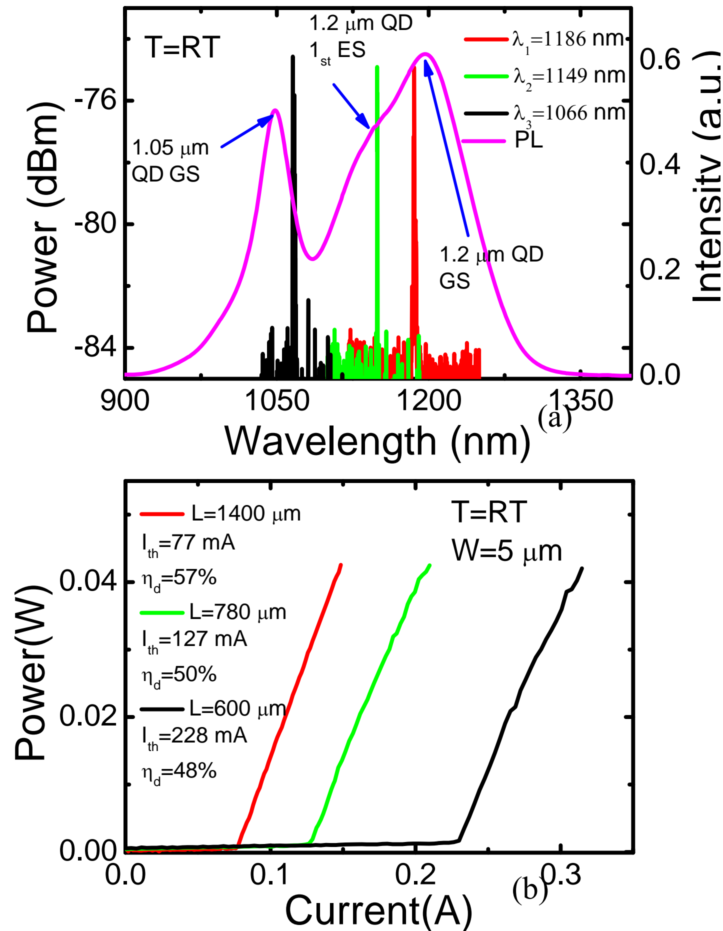


Fig 4.4 (a) Electroluminescence and Photoluminescence spectrum of the three channels at room temperature; (b) L-I measurements of the four lasers under CW biasing

Generally, the relaxation of carriers from the excited state to the ground state is believed to be a bottleneck because the device only lases in the ground state. The finite time constant restricts the light output of the ground state lasing, which piles up carriers in the excited state, resulting in excited state lasing [88-89]. However, these lasers all lase in the ground state of the QDs, which have relatively close threshold current values. Thus, laser arrays can be operated at almost the same bias. The measured temperature dependence of $J_{th}$ and $\eta_d$ is shown in Fig. 4.5. The corresponding temperature coefficients $T_0$ and $T_1$ can be found from the following equations:

$$J_{th}(T) = J_{th}(0)\exp\left(\frac{T}{T_0}\right) \tag{4.2}$$

$$\eta_d(T) = \eta_d(0)\exp\left(-\frac{T}{T_1}\right) \tag{4.3}$$

The obtained value of $T_0$ are 77, 82, 76, and 70 K for lasers 1, 2, 3, and 4, respectively, whereas the values of $T_1$ are 210, 280, 285, and 270 K, respectively. The typical value of $T_0$ in InGaAs/InP double heterostructure 1.3 μm lasers is ~50 K. The excellent temperature stability of these lasers, as characterized by their large values of $T_0$ and $T_1$, is a direct consequence of the use of tunnel injection and p-doping. Tunnel injection is used to suppress the hot carrier effect and carrier leakage from the QD lasing states that allow cold carriers (electrons) to be injected by tunneling in the QD lasing states and the minimization of carrier occupation in the wetting layer and barrier states. P-doping of the QDs ensures that hole ground states are filled, thereby substantially increasing the gain and differential gain. Therefore, both of these techniques can be used to enhance $T_1$ and $T_0$ [57].

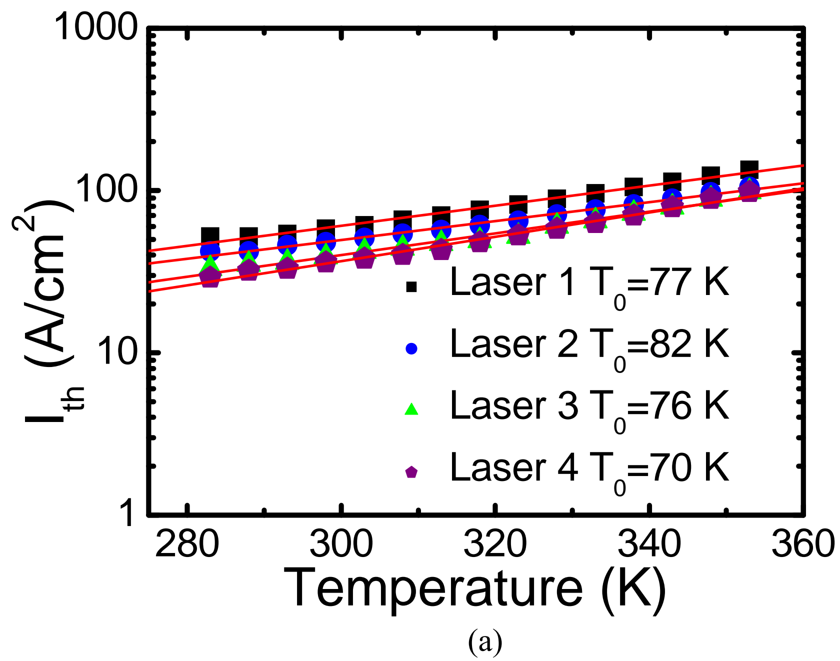


(a)

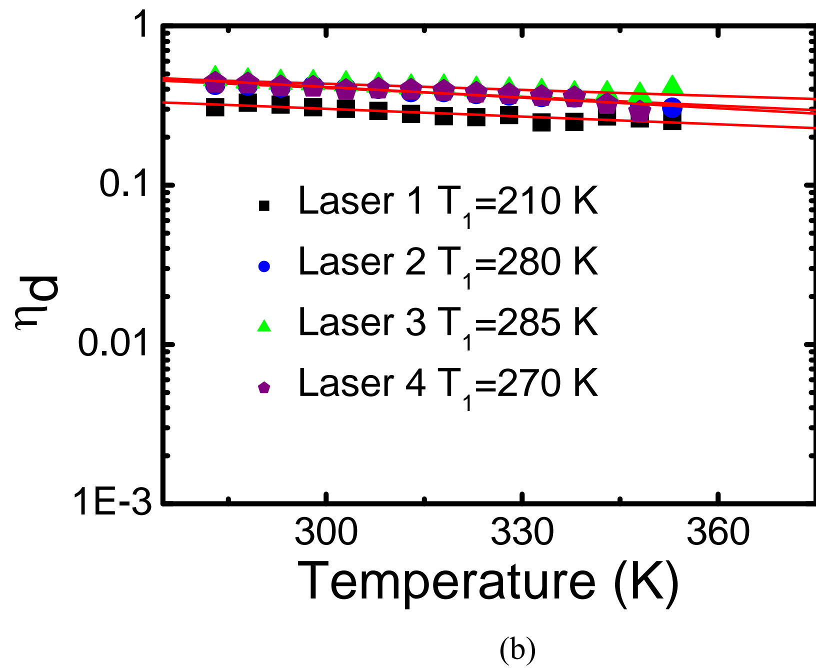


(b)

Fig. 4.5 (a) Temperature dependence of $J_{th}$ and the characteristic temperature, $T_0$, for each device; (b) Temperature dependence of $\eta_d$ and $T_1$ for each laser.

### 4.3.2 Comb Lasers

Figure 4.6 shows the spectrum from the comb laser, measured at room temperature with a pulsed bias current of 0.95 A (28 $I_{th}$). The spectral bandwidth is characterized with a 81 nm (FWHM) and a 90 nm ($\triangle_{-13dB}$) wide lasing spectrum, which is the broadest emission for InAs or InGaAs QDs [90]. The total output power density is 400 mW from both facets under a pulsed bias current density of 0.95A, which corresponds to 5 mW/nm.The inset to Fig. 5.2 illustrates the room temperature light current (L-I) characteristics, measured with pulsed and continuous-wave (CW) biasing, for a device with a 1040 µm cavity length. The corresponding threshold current density $J_{th}$=650 and 675 A/cm$^2$, respectively, and the differential efficiency $\eta_d$ = 52 and 40%, respectively. The relatively high values of $J_{th}$ are attributed to p-doping of the dots and the associated enhancement of Auger recombination [73, 91].

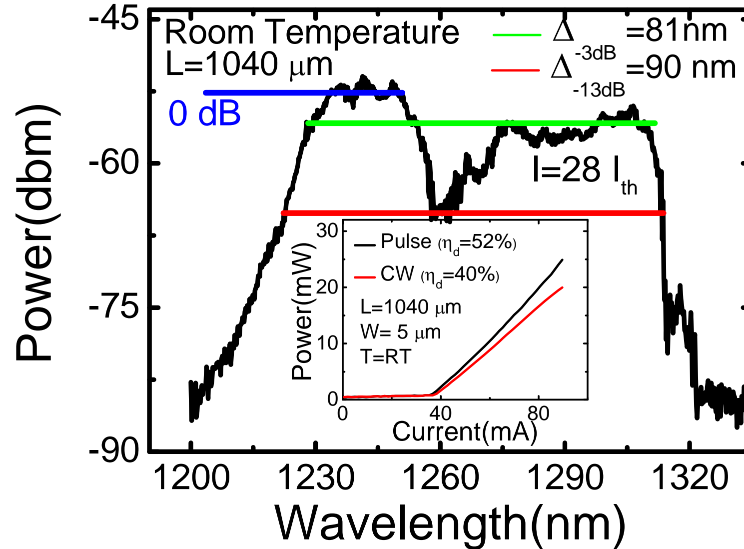


Fig. 4.6 Electroluminescence spectrum at 300 K. The inset shows pulsed and CW light-current data at room temperature with threshold current density $J_{th}$=650 and 675 A/cm$^2$ and differential efficiency $\eta_d$ = 52 and 40%, respectively.

From the measured dependence of $\eta_d$ on cavity length, an internal quantum efficiency $\eta_i$ = 77% and a waveguide propagation loss $\alpha_i$ = 7 $cm^{-1}$ are calculated. The measured temperature dependence of $J_{th}$ and $\eta_d$ are shown in Fig. 4.7 (a) for a device with a cavity length of 2060 µm. The corresponding temperature coefficients $T_0$ and $T_1$, given by $I_{th}(T) = I_{th}(0)exp(T/T_0)$ and $\eta_d(T) = \eta_d(0)exp(T/T_1)$ respectively, are 110 and 300 K. It may be noted that for InGaAs/InP double heterostructure 1.3 µm lasers, $T_0$ typically has a value of ~50 K which described earlier. The excellent temperature stability of the lasers characterized by the large values of $T_0$ and $T_1$ is a direct consequence of tunnel injection and p-doping. Hot carrier effects and carrier leakage from the active region are reduced by tunnel injection of electrons into the quantum dot. P-doping of the dots increases electron-hole scattering and consequently the Auger recombination rate. This helps to increase $T_0$, at the cost of an increased $I_{th}$ [90], which I observe in these devices. Figure 4.7(b) depicts the variation of modal gain with threshold current density. The latter are measured in lasers of different cavity lengths. The data are fitted to the empirical relation $g_{mod}=g_{sat}\{1-exp[-\gamma(J_{th}-J_{tr})/J_{tr}]\}$ plotted as a the solid curve, where $g_{mod}$ is the modal gain, $g_{sat}$ is the saturation modal gain, $\gamma$ is a non-ideality factor and $J_{tr}$ is the transparency current density [92]. The saturation modal gain per quantum dot layer is 4 $cm^{-1}$, which is matches the values of 3-4 $cm^{-1}$ per dot layer reported for 1.3 µm quantum dot lasers [92]. Thus, the broad gain spectrum does not reduce the peak gain, possibly due to p-doping of the dots.

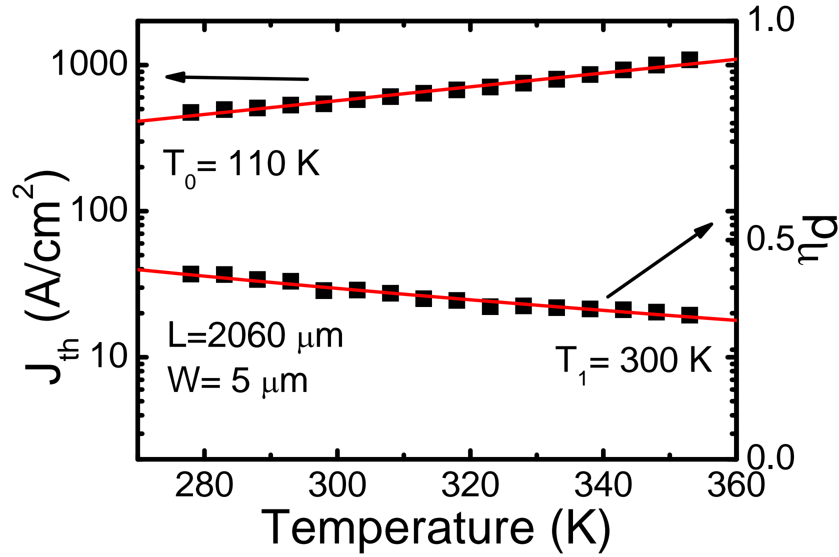


(a)

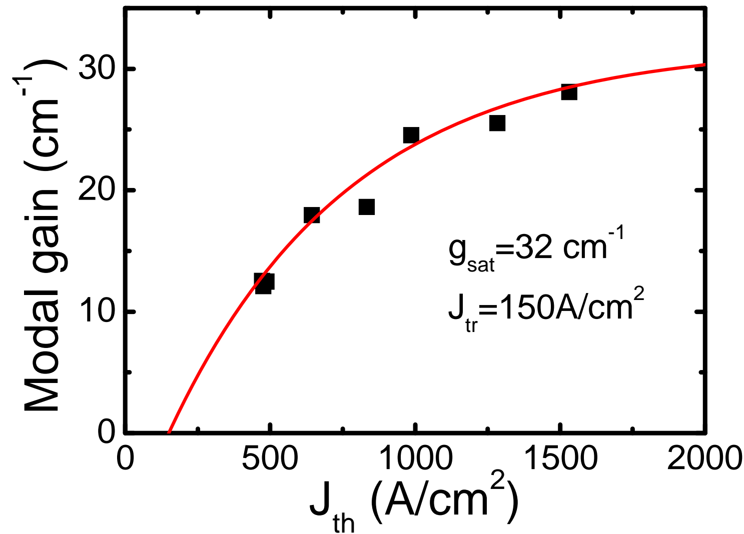


(b)

Fig. 4.7 (a) Temperature dependence of $J_{th}$ and $\eta_d$ , from which $T_0$ and $T_1$ were derived to be 110 and 300K; (b) ground-state modal gain versus current density of comb laser from which a saturated modal gain of 4 cm$^{-1}$ per QD layer and a transparency current density $J_{tr}$ = 150 A/cm$^2$ are derived.

Figure 4.8 shows high-resolution room temperature lasing spectra in the wavelength range of 1283-1288 nm for two cavity lengths, 1040 and 2060 μm. The respective channel spacings are ~0.2 and 0.1 nm, thereby demonstrating good control of channel spacing with

cavity length. The spacings are in good agreement with theoretically calculated ones using the equation: $\Delta\lambda(\lambda)= \lambda^2/2n_{eff}L$ where L is the cavity length and $n_{eff}$ is the effective refractive index of the gain region dependent on T, λ, and J [93]. For the laser with a 1040 μm cavity length, there are 105 and 185 simultaneously emitted longitudinal modes in the spectral range of 1231-1252 nm and 1274-1311 nm respectively with a non-uniformity of the peak intensity of less than 3 dB. The inset shows lasing spectra measured at 300 and 323 K. The peak wavelength spacing of 0.2 nm remains unchanged, demonstrating extremely good temperature stability of the multi-wavelength lasers. The maximum measured peak-to-peak ratio is ~20 dB, but I believe that the actual signal-to-noise ratio (SNR) of the device is much larger with the measured value being limited by the resolution of our optical spectrum analyzer (estimated to be ~ 0.08 nm).

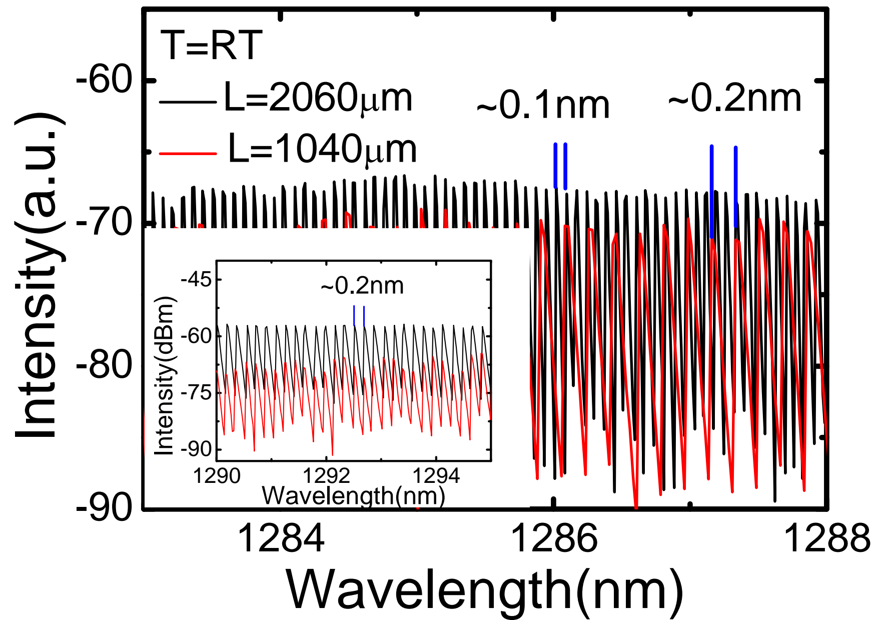


Fig. 4.8 (a) Electroluminescence spectra at 300 K in the wavelength range of 1283-1288 nm for two cavity lengths: 1040 and 2060 μm. The respective channel spacings are ~0.2 and 0.1 nm; (b) the inset shows electroluminescence spectra at 300 and 323K with unchanged 0.2 nm peak wavelength spacing.

Small-signal modulation measurements were made at room temperature to determine the frequency response of the lasers. The modulation response characteristics of a device with L = 1040 μm at different injection current levels are shown in Fig. 4.9. A maximum modulation bandwidth ($f_{-3dB}$) of 7.5 GHz is measured. This compares favorably with the largest small-signal modulation bandwidth measured for a high-speed 1.3 μm QD laser [45]. Without the incorporation of tunnel injection and p-doping in a comb laser, the 3 dB bandwidth would have been limited to ~1.25 GHz, as reported earlier [84]. The small-signal response at high values of injection, as seen in Fig. 4.9, is characterized by what appears to be multiple resonance peaks. I believe that such multiple peaks in the frequency response would be a characteristic of QD lasers with a large distribution of dot size. With increased injection, there is a dynamic redistribution of carriers between dots of different sizes, accompanied by gain compression and mixed lasing between ground and excited states. Thus the resonance frequency $\omega_R$ of the largest dots is first reached and subsequently the smaller dots. The modal gain is larger in smaller dots.

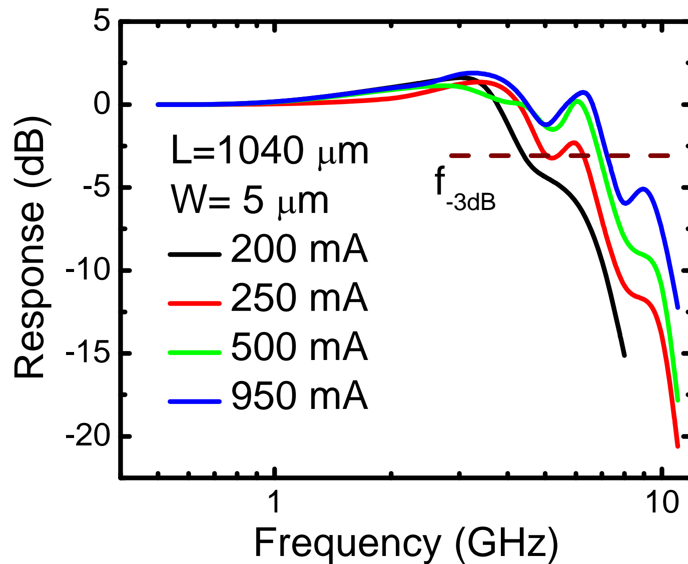


Fig. 4.9 Small-signal modulation bandwidth of a QD comb laser with L= 1040 μm at different injection current levels. A maximum modulation bandwidth ($f_{-3dB}$) of 7.5 GHz is measured.

### 4.4 Conclusions

In summary, I successfully achieved three different light emission wavelengths using the same heterostructure. These emission wavelengths are related to the GS and $1^{st}$ ES of the InAs QDs, and GS of the InGaAs QDs and also demonstrated a four-channel QD laser with near equal channel spacing (~5 nm) and threshold current that can be controlled by simply altering the cavity length. By using a p-doped, tunnel injection, chirp QD laser heterostructure, the laser also shows good temperature stability with $T_0$~ 75 $^oC$ and $T_1$~270 $^oC$. This laser has high potential for use in future local area network connections especially when a single wavelength operation is not a stringent requirement.

It is also of interest to discuss the implications of the measured comb laser characteristics. The wide output spectrum confirms that many channels can be obtained for DWDM communication. The large modulation bandwidth, a direct consequence of tunnel injection, implies that individual channels can be modulated at a frequency of ~7.5 GHz. Therefore, several identical high-speed comb lasers with direct (current) modulation can be used in a WDM—Passive Optical Network (WDM—PON) architecture [84] instead of LEDs which have poor modulation bandwidth. In this scheme, the directly modulated channels of the comb lasers are transmitted through a filter or slicer onto the optical link.

Multi-wavelength laser sources and modulator/driver arrays are the principal impediments to downscaling and allowing WDM to be more practical. Today WDM optical sources are based on DFB arrays on lnP [94], which can perhaps be bonded onto silicon in the near future [95], have several drawbacks. These include the complexity in packaging multiple lasers, modulators, and drivers, as well as the need for temperature control, and the fact that multiple wavelength tracking may become untenable in

large-scale deployments. The maximum number of lasers is limited by yield and system performance. I believe that a better alternative, particularly for what will become these signaling systems, is a single diode comb laser based on lnAs/GaAs quantum dots (QDs) [96-97] that can provide multiple narrow-spectrum peaks, each corresponding to a longitudinal mode of the laser cavity. This single laser is a viable WDM source, and it overcomes many of the drawbacks of discrete laser array sources in conventional systems, Two potential comb laser-driven transceiver approaches are illustrated in Fig. 4.10 [98]. Although comb laser-based WDM is promising for development of efficient and cost-effective, high bandwidth optical interconnects for future computer systems, as well as spectrum slicing for WDM-PON. The former includes transceivers for optical cables and for much shorter board-level interconnects. In both cases PICs or silicon ring resonators would be integrated with their DEMUX/modulation/MUX functionality. It has been proposed [99] that one can build on-chip silicon interconnects using arrays of rings in conjunction with a multi-frequency laser. A ring-based WDM optical interconnect would have many advantages compared with the MUX/DEMUX system. Rings are much more compact than MUX/DEMUX devices, and they consume less power than less-frequency selective modulators such as Mach-Zehnder interferometers. In addition, the ability to "turn off a ring by taking it off-resonance allows us to build transparent switches that can be used to full advantage in building innovative, high-performance computer architectures [99]. Ring resonators, however, present numerous challenges as well. First and foremost are a number of fabrication challenges. One needs rings with a large FSR, (in excess of 30 nm) to accommodate a large number of WDM channels. As a consequence the ring diameter has to be 5 um or less. However

to get channel spacing of the order of 80 GHz or less one needs to be able to fabricate rings and control their diameter with a precision of a few nm. It is also unclear how other fabrication imperfections such as waveguide roughness affect channel spacing will affect the performance. This microring-based transceiver has very challenging silicon photonics processing requirements. An intriguing possibility is to use comb lasers for network-on-chip optical interconnects, particularly since the demultiplexing and modulation is done directly by the network-on-chip rather than a separate transmitter module. Therefore, the comb laser output only has to be coupled to the chip and distributed to the waveguide array, e.g., via a star coupler similar to that in AWGs. Coupling costs need to be reduced dramatically, however, but the necessary packaging technology is available, and temperature adaptability also remains challenging.

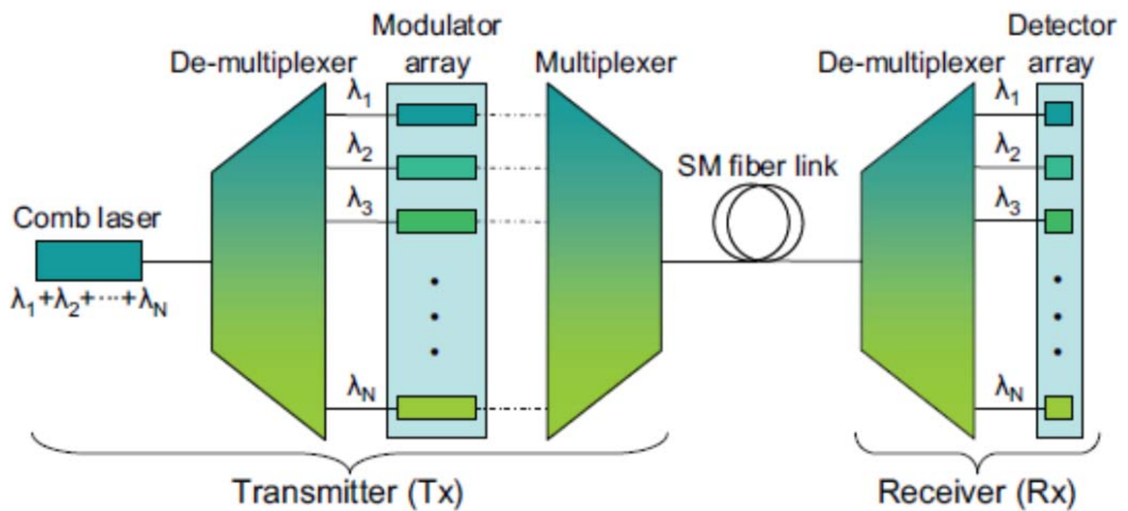


(a)

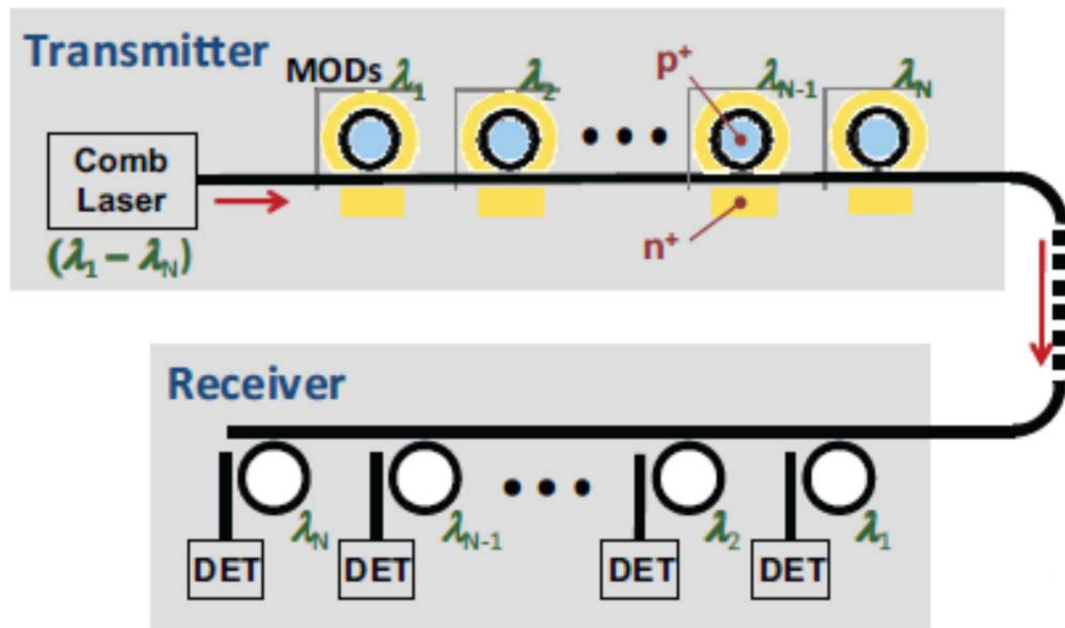


(b)

Fig. 4.10 Comb laser-based WDM transceiver options: (a) conventional design based on comb channel de-multiplexing, modulation, and multiplexing in the Tx, de-multiplexing and detection in the Rx; (b) unconventional design based on in- line ring resonators for combined channel selection and modulation in the Tx [100] and channel selection and detection in the Rx.

# Chapter 5

# Distributed Feedback and Tunable Distributed Bragg Reflector Lasers with Quantum Dot Active Region

## 5.1 Introduction

In Fabry-Pérot quantum dot lasers, the inhomogeneous broadening of the photoluminescence and gain spectra in quantum dots makes the output spectrum multi-mode. However, to be suitable for use in optical communications, these lasers should emit at only a single longitudinal mode which will minimize the dispersion of the signal in the waveguide, and also to maximize the number of individual channels which can be modulated. To this end, it is desirable to modify the standard Fabry-Pérot structure to add wavelength selective loss. However, due to the optical dispersion in the waveguides and other photonic components, they must also have a single longitudinal mode. Otherwise, the modulated signal will undergo dispersion in the fiber, limiting the bandwidth. Single longitudinal mode quantum dot lasers can be created by making modifications to the laser cavity, or the mirror reflectivity. In a similar manner to chapter 4, where I selectively induced loss to particular modes, I will make modifications to the device structure to introduce losses to undesired modes. In this chapter, the distributed feedback (DFB), and distribute Bragg reflector (DBR) lasers and designed, fabricated, and characterized. Self-assembled quantum dots, which allow for the fabrication of lasers with low threshold current [11-13], large differential gain [101-102], low chirp [103], and

low linewidth enhancement factor [104], are very suitable for use in photonic integrated circuits, and will be used as the active region for such DBF and DBR lasers.

A distributed Bragg reflector is a structure which provides high reflectivity, known as the Bragg wavelength. To design such as reflector, alternating pairs of materials satisfying the following condition are fabricated:

$$d = \frac{\lambda_0}{4n} \tag{5.1}$$

where d is the thickness of a particular layer, $\lambda_0$ is the lasing wavelength in free space, and n is the index of the layer. Creating pairs of alternating layers, with different refractive indices, each meeting this condition in that layer, will create a high reflectivity at $\lambda_0$, if sufficiently many layers are fabricated. If each of the layers meets the condition given in eqn. 5.1, then a wave propagating through the DBR will experience a large reflectivity. If the reflection at each interface is considered, the waves which are reflected will add up coherently outside the DBR, causing the high reflectivity. Away from this wavelength, the reflectivity depends on how the individual reflections add up, either coherently or destructively. If the difference in indices ($\Delta n$) between the two layers is small, the reflections at each interface will be small. In this case, many periods will be needed in order to obtain the same reflectivity as that from a DBR with a large $\Delta n$.

An alternative to using the shallow metal grating DBR is to use an etched semiconductor grating. Applying a bias to the semiconductor grating changes the index of the material, effectively altering the Bragg wavelength. This shift occurs by two mechanisms, the heating of the semiconductor redshifts the Bragg wavelength while a carrier induced index change blue-shifts the output wavelength. Additionally a phase

tuning section can be used to fine tune the output wavelength, with the three section device, illustrated in Fig. 5.1.

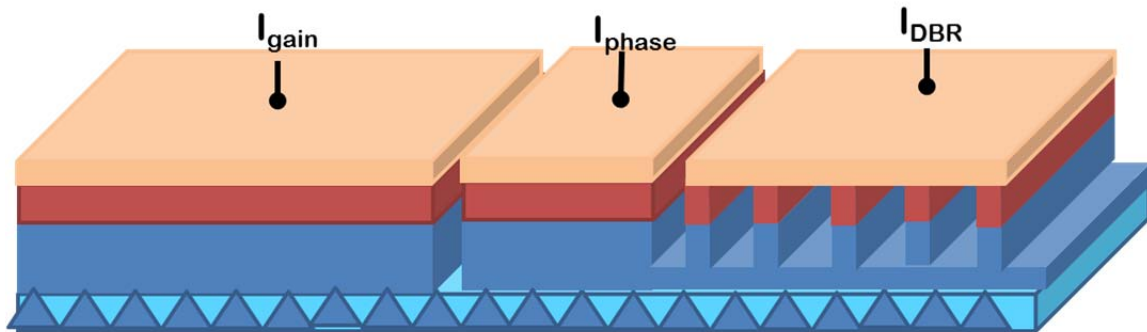


Fig. 5.1 The tunable DBR consists of three sections: the gain, phase, and DBR section with a contact to alter the grating index through a biasing current.

## 5.2 Experiment

### 5.2.1 Quantum Dot Distributed Feedback Laser

First I fabricated a distributed feedback laser using the Bragg reflector discussed. A DFB consists of the placing the wavelength selective grating throughout the gain region. I fabricate our DFB, using the heterostructure presented in Fig. 5.2. Traditional DFBs use gratings etch in the middle of the heterostructure. However, gratings grown in this way require the sample to be removed from growth, the gratings etched, followed by a second growth to finish growing the upper half of the laser heterostructure. Instead of fabricating this type of typical DBR, I choose to fabricate a half etched vertical gratings [105], as shown in Fig. 5.2. This type of grating can be fabricated without the need for expensive regrowth.

300 nm $P^+$ GaAs contact layer (Be 5e19 $cm^{-3}$)
20 nm $Al_{0.6}Ga_{0.4}As$ ◊ $Al_{0.08}Ga_{0.92}As$ (Be 5e18 $cm^{-3}$)
1100 nm $Al_{0.6}Ga_{0.4}As$ (Be 5e18 $cm^{-3}$)
400 nm $Al_{0.6}Ga_{0.4}As$ (Be 2e17 $cm^{-3}$)
45 nm $Al_{0.3}Ga_{0.6}As$
20 nm GaAs capping
34 nm GaAs (600$^0$C)
10 nm GaAs (500$^0$C)
8 nm $In_{0.15}Ga_{0.85}As$ /2.3 ML InAs QDs/
2 nm $In_{0.15}Ga_{0.85}As$
10 nm GaAs spacer
5 nm $In_{0.2}Ga_{0.8}As$ injector well
50 nm GaAs
45 nm $Al_{0.3}Ga_{0.6}As$
400 nm $Al_{0.6}Ga_{0.4}As$ (Si 5e17 $cm^{-3}$)
1100 nm $Al_{0.6}Ga_{0.4}As$ (Si 5e18 $cm^{-3}$)
20 nm $Al_{0.08}Ga_{0.92}As$ ◊ $Al_{0.6}Ga_{0.4}As$ ( Si 5e18 $cm^{-3}$)
500 nm $n^+$ GaAs ( Si 5e18 $cm^{-3}$)
$n^+$ GaAs Substrate



(a)



(b)

Fig. 5.2 (a) Schematic overview of the DFB structure using a half etched DFB grating. (b) An SEM image of the DFB after fabrication.

### 5.2.2 Quantum Dot Distributed Bragg Reflector Laser

Unlike the DFB which uses grating throughout the laser gain section, a DBR laser using the grating as a mirror coating at one end of the laser, instead of throughout the gain section. However, it serves a similar purpose in providing frequency selective feedback. Using transfer matrix method, I first designed a DBR using a shallow deposited metal grating, using the heterostructure presented in Fig. 5.3 (a), with a schematic overview of the grating in Fig. 5.3 (b).

| 300 nm $P^+$ GaAs contact layer (Be 5e19 $cm^{-3}$) |
| --- |
| 20 nm $Al_{0.6}Ga_{0.4}As$ ◊ $Al_{0.08}Ga_{0.92}As$ (Be 5e18 $cm^{-3}$) |
| 1100 nm $Al_{0.6}Ga_{0.4}As$ (Be 5e18 $cm^{-3}$) |
| 400 nm $Al_{0.6}Ga_{0.4}As$ (Be 2e17 $cm^{-3}$) |
| 40 nm $Al_{0.08}Ga_{0.92}As$ ◊ $Al_{0.6}Ga_{0.4}As$ |
| 40 nm GaAs capping |
| 15 nm GaAs/10 nm GaAs(Be doped) ($600^0C$)/ 9 nmGaAs |
| 6 nm GaAs ($500^0C$) |
| 2.3 ML InAs QDs/5 nm $In_{0.15}Ga_{0.85}As$ |
| 5 nm GaAs spacer |
| InGaAs injector well |
| 80 nm GaAs |
| 40 nm $Al_{0.6}Ga_{0.4}As$ ◊ $Al_{0.08}Ga_{0.4}As$ |
| 400 nm $Al_{0.6}Ga_{0.4}As$ (Si 5e17 $cm^{-3}$) |
| 1100 nm $Al_{0.6}Ga_{0.4}As$ (Si 5e18 $cm^{-3}$) |
| 20 nm $Al_{0.08}Ga_{0.92}As$ ◊ $Al_{0.6}Ga_{0.4}As$ ( Si 5e18 $cm^{-3}$) |
| 500 nm $n^+$ GaAs ( Si 5e18 $cm^{-3}$) |
| $n^+$ GaAs Substrate |

(a)

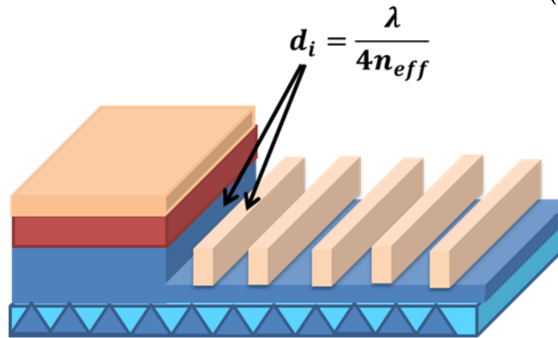


(b)

Fig. 5.3 (a) The laser heterostructure is presented. (b) The grating consists of deposited shallow metal grating, deposited near the active region.

The reflectivity of the laser is simulated by transfer matrix method (TMM), and is presented in Fig. 5.4 (a). The grating width is chosen to be 5 µm over a length of 75 µm. The metal thickness is ~100 nm, and it is deposited ~45 nm above the active region. Titanium is chosen as the metal for the grating due to its relatively low loss at 1.3 µm, with the extinction coefficient, k=3.52. An SEM image of the fabricate grating is presented in Fig. 5.4 (b).

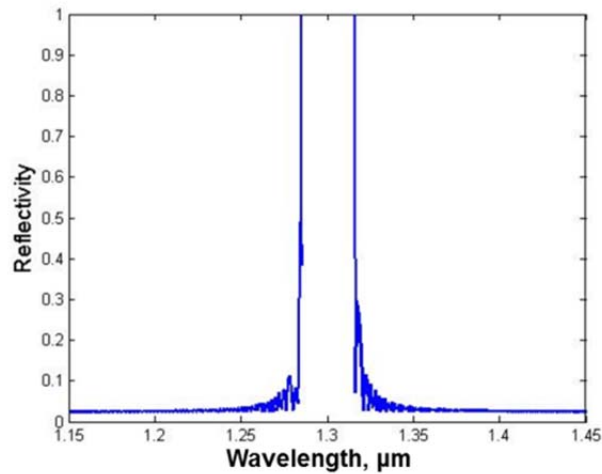


(a)

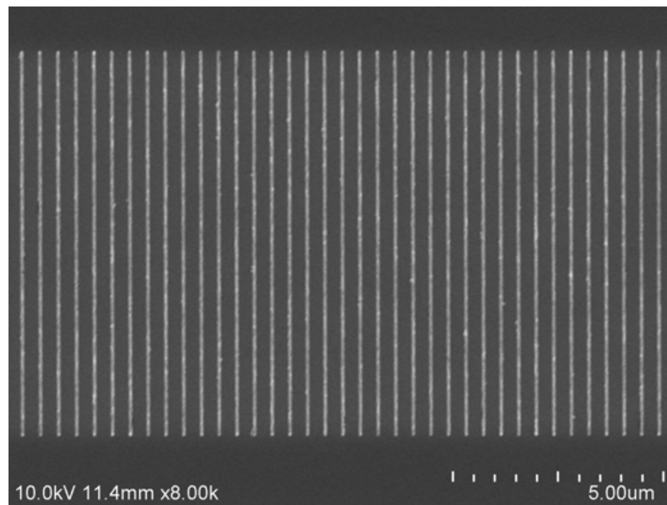


(b)

Fig. 5.4 (a)The grating reflectivity is plotted using the transfer matrix method. (b) An SEM image of the shallow titanium metal grating.

### 5.2.3 Quantum Dot Tunable Distributed Bragg Reflector Laser

Applying a bias to the phase section also affects the index, in the manner described above. The change index creates an effective change in the cavity length, slightly altering the cavity modes. The overall wavelength shift can be given by the following formula [106]:

$$\frac{\Delta\lambda}{\lambda} = \frac{\Delta n_g L_g + \Delta n_p L_p + \Delta n_{DBR} L_{eff}}{n_g L_g + n_p L_p + n_{DBR} L_{eff}} \tag{5.2}$$

where $n_g$ is the gain index, $n_p$ is the phase index, $n_{DBR}$ is the effective index of the DBR, and $L_{eff}$ is the effective length of the DBR. The simulated DBR maximum tunable range is presented in Fig. 5.5.

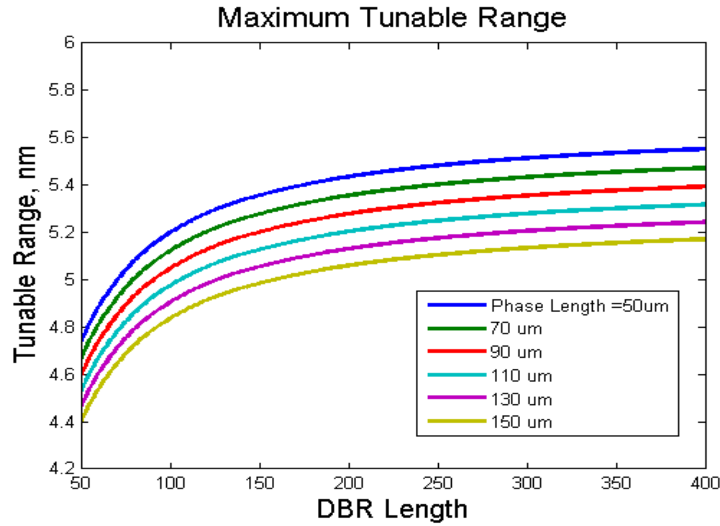


Fig. 5.5 Maximum tunable range of the DBR as a function of (actual) DBR length.

A three section device (using the same heterostructure as the shallow metal grating DBR) with a tunable DBR and phase tuning section was fabricated. Normally, a thinner p cladding is grown in order to fabricate the grating. This reduces the optical confinement factor, Γ, and increases the loss [107]. I kept the thick p cladding, and etched a trench to the top grating. Then the grating was etched down from there. In order to

prevent metal from filling in the grooves [108], the interconnection metal is deposited on the edge of the DBR gratings, with a thin metal remaining on top of the gratings from the e-beam step. This keeps the appropriate index difference between the semiconductor and $SiO_2$ gratings. A metal grating would also introduce a loss if it filled in the space between gratings. The fabricated DBR grating is shown in an SEM, in Fig. 5.6 (a), with a schematic of the final grating structure shown in Fig. 5.6 (b). A picture of the three section device with contacts is shown in Fig. 5.6 (c).

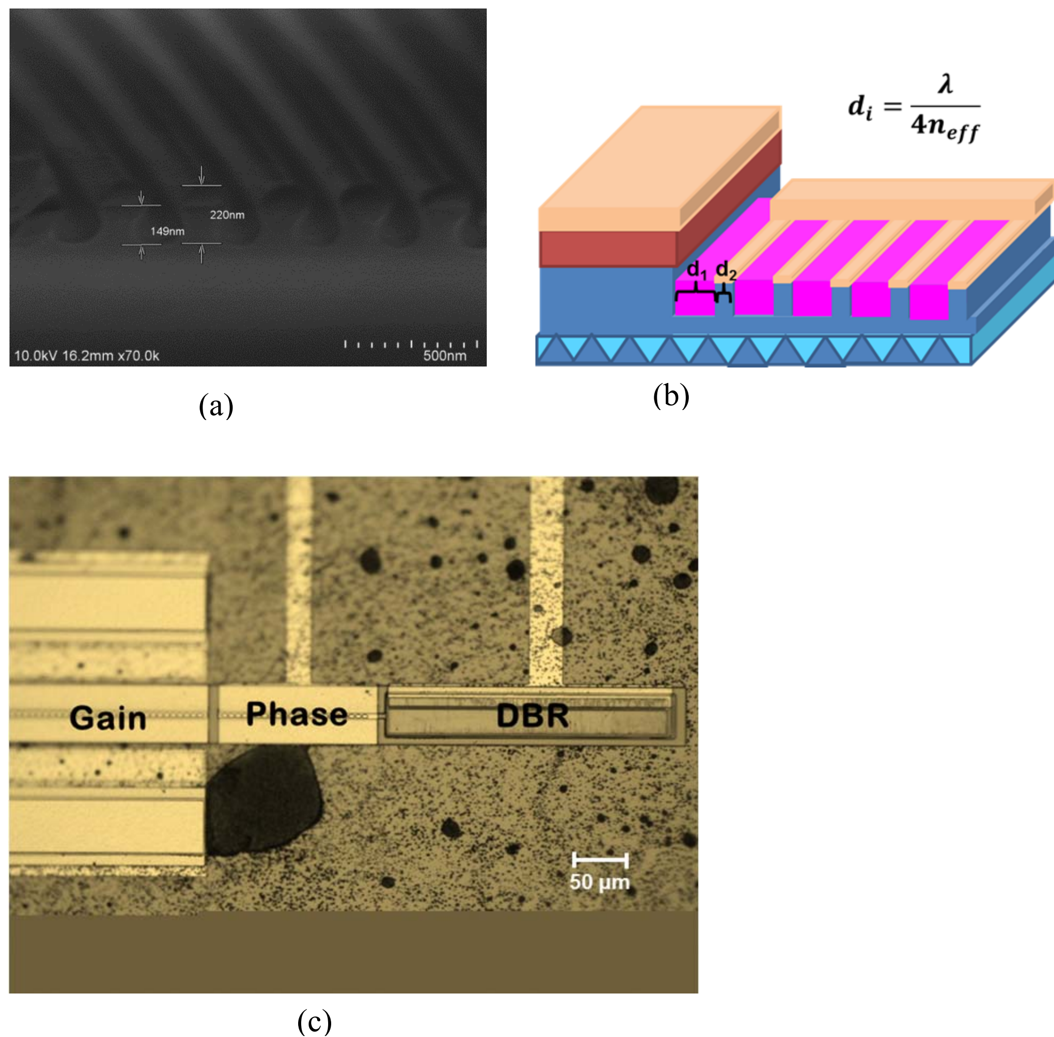


Fig. 5.6 (a) An SEM of the semiconductor grating. (b) A schematic of the grating showing a thin metal strip of metal remaining from the e-beam step acting as contact to the grating. (c) A picture showing the three sections of the fabricated DBR.

### 5.3 Results and Discussion

#### 5.3.1 Quantum Dot Distributed Feedback Laser

The fabricated DFB laser has a ridge width of 3μm, with a cavity length of 1230 μm. The DC characteristics are presented in Fig. 5.7 (a). The DFB laser is characterized by a threshold current density of 258 A/cm$^2$, and an external quantum efficiency, $\eta_d$=43%. The electroluminescence spectrum is presented in Fig. 5.7 (b). The DFB is shown to be pure single mode with a full width at half maximum (FWHM) of 0.16 nm at a peak emission wavelength of 1286 nm.

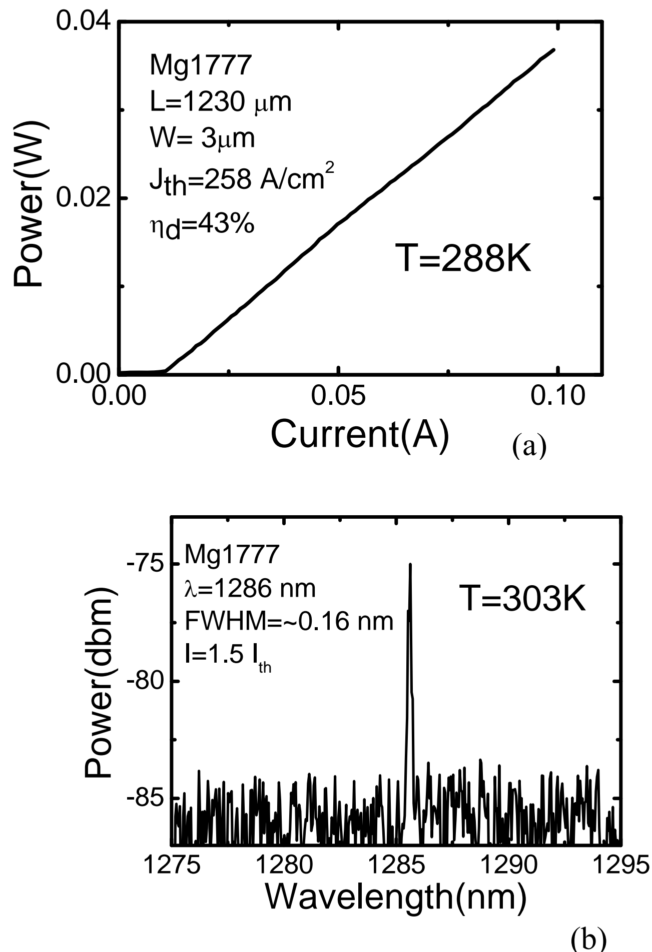


Fig. 5.7 (a)The light-current measurements from the DFB show $J_{th}$=258 A/cm$^2$, and $\eta_d$=43%. (b) The spectrum is shown to be a pure single mode at 1286 nm, with FWHM=0.16 nm.

The temperature dependence of the DFB characteristics was also studied. The threshold current of the laser follows the following relationship:

$$J_{th}(T) = J_{th}(T_0)e^{T/T_0} \quad (5.3)$$

A similar relationship for the external quantum efficiency can be written:

$$\eta_d(T) = \eta_d(T_0)e^{-T/T_1} \quad (5.4)$$

where $T_0$ and $T_1$ are empirical figures of merit describing the temperature dependence of the threshold current (density), and external quantum efficiency, respectively. To measure these performance characteristics, L-I measurements were taken from DFB from 280 to 325K. The temperature dependence of these two parameters is presented in Fig. 5.8 (a). The DFB is characterized by $T_0$=60 K, and $T_1$=380 K. Additionally, the temperature dependence of the output wavelength was also studied from 0$^o$C to 20$^o$C, and found to be 0.1 nm/$^o$C, which is a factor of five times lower than of traditional 1.3 μm InAs/GaAs QD lasers, which have a temperature dependence of . The temperature dependence of the lasing wavelength is presented in Fig. 5.8 (b).

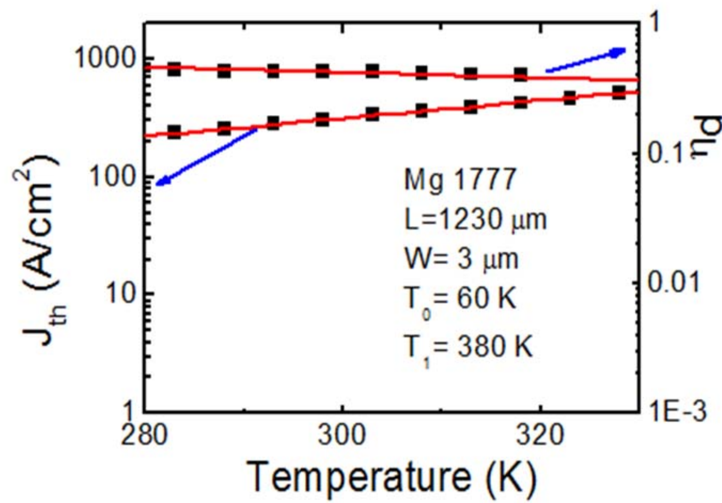


(a)

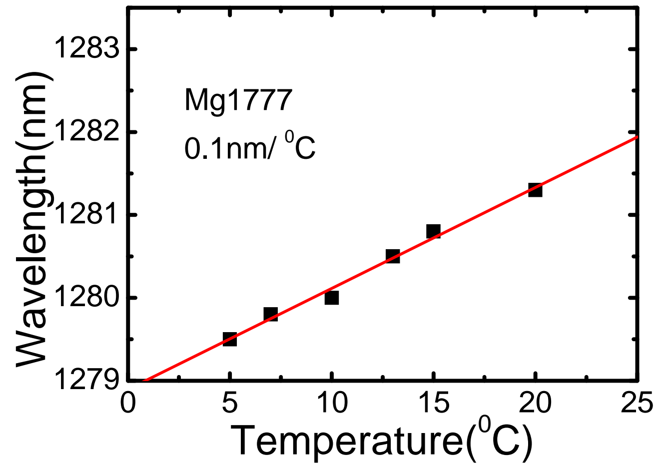


(b)

Fig. 5.8 (a) The DFB laser is characterized by $T_0$=60K, and $T_1$=380 K, and (b) a temperature dependence of the lasing wavelength of 0.1 nm/$^o$C.

### 5.3.2 Quantum Dot Distributed Bragg Reflector Laser

I demonstrate a QD DBR laser with a 5 µm cavity width. The relatively high threshold current and relatively low external quantum efficiency (only considering one facet) are likely due to the closer proximity of the grating to the active region, than in the design. This creates a larger loss. However, the side mode suppression ratio (SMSR) is greatly enhanced to ~30 dB due to the larger mode interaction of grating at this position, as shown in Fig. 5.9. The light-current measurements are presented in Fig. 5.10 (a). The emission wavelength changes by ~0.1 nm/$^o$C over a range of 5 to 85$^o$C, as shown in Fig. 5.10 (b), which is a factor of five times lower than the 1.3 µm InAs/GaAs QD FP laser (~0.5 nm/$^o$C).

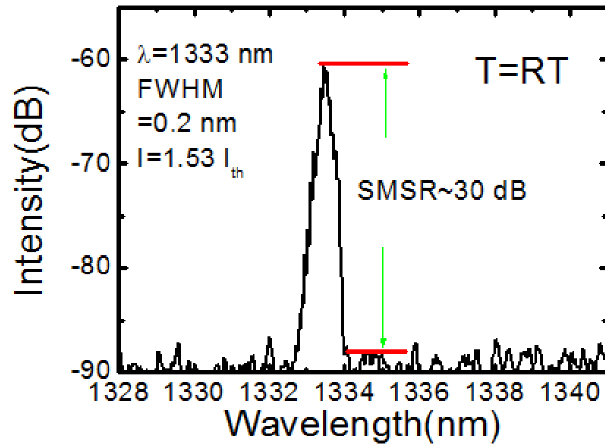


Fig. 5.9 The emission wavelength occurs at 1333 nm, with a FWHM of 0.2 nm at 1.53 Ith. The SMSR is ~30 dB.

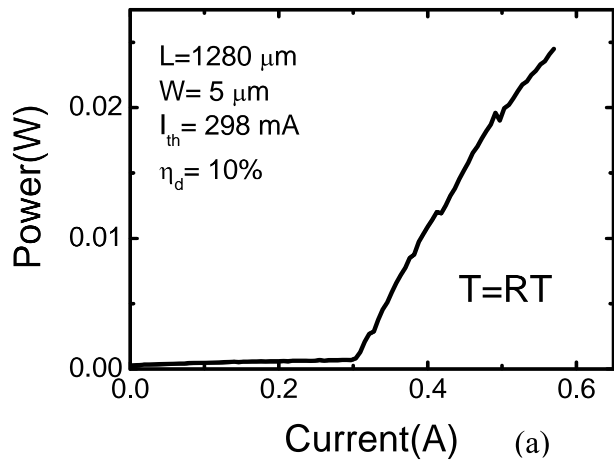


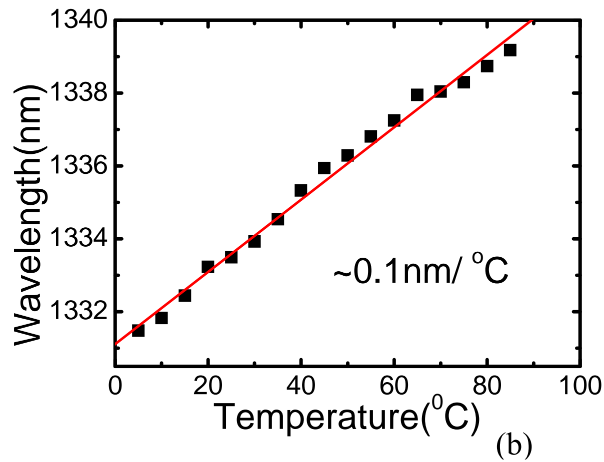


Fig. 5.10 (a) The light current measurement with a threshold of 298 mA. (b) The temperature dependence of the emission wavelength is 0.1 nm/°C.

### 5.3.3 Quantum Dot Tunable Distributed Bragg Reflector Laser

The spectrum of the laser, with a cavity length 980 μm and a ridge width of 4 μm is measured at three biases applied to the DBR grating, and is shown in Fig. 5.11 (a), with biases of 0V, 1V, and 1.2V. These three biases are characterized by an emission wavelength of 1325 nm, 1326 nm, and 1329 nm, respectively. The relatively high threshold current is likely due to absorption in the phase and grating sections due to the unbiased (non-inverted) quantum dots. This can be reduced, if I further biased the grating section, or biased the phase section as shown in the light current measurements in Fig 5.11 (b). The curves are characterized by several kinks, characteristic of mode hopping [109]. The maximum tunable range is limited by the change in the refractive index which can be applied to the DBR section, of which there are two competing processes: a temperature induced and a carrier induced change in the index. I measured a tunable range of ~ 4nm, which is in the range of $\Delta\lambda$=2-4 nm, suitable for WDM. The lasing peaks are true single modes with a FWHM linewidth of ~0.2 nm, and a SMSR of ~25 dB.

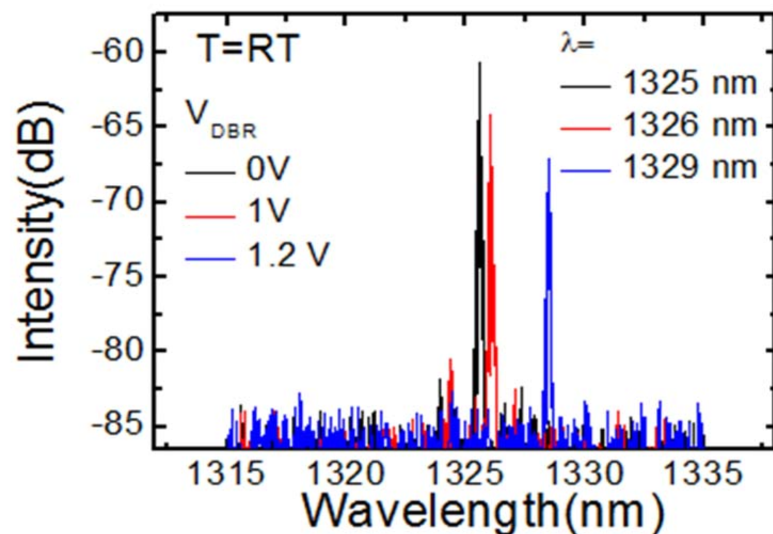


(a)

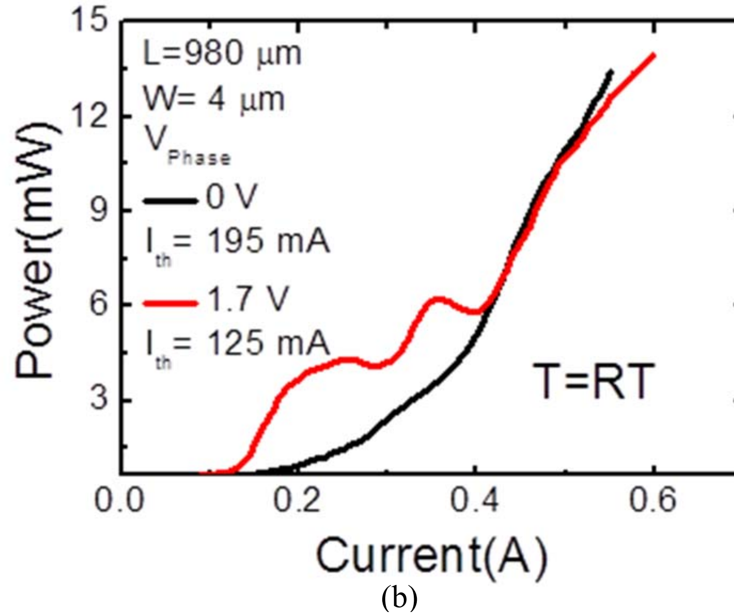


(b)

Fig. 5.11 (a) The laser spectrum is shown as a function of DBR bias voltage. (b) the light current characteristics of the laser.

## 5.4 Conclusion

In summary, I designed, characterized, and fabricated three single longitudinal devices: a half etched vertical DFB, a DBR with deposited shallow metal grating, and a shallow etched tunable DBR. The three devices are characterized by their excellent side mode suppression ratio of 10 dB, 30 dB, and 25 dB, respectively. They are characterized by excellent temperature stability of 0.1 nm/$^{o}$C, which favor excellently compared with traditional Fabry Pérot ridge waveguides without grating. The relatively high threshold current of the quantum dot tunable laser is likely due to the absorption in the phase and grating section due to the presence of non-inverted quantum dots. This device can replace the complicated and expensive DFB or DBR laser array with the precise wavelength control of < 1nm in DWDM system.

# Chapter 6

# Monolithic Integration of Quantum Dot Lasers with Waveguides for High Temperature Operation

## 6.1 High temperature Stability of 1.3 µm Quantum Dots Lasers with Dry Etched Facets

### 6.1.1 Introduction

As the demand for higher performance microchips, with larger data throughput, continues to rise, along with the desire to continue to shrink such devices, it is becoming increasingly necessary to develop alternatives to electrical interconnects which use more power, have higher electrical delay, and have poor signal integrity as they are scaled down. A quantum dot laser, integrated with optical interconnects is an attractive candidate for such purposes [110]. One requirement for such devices will be high quality laser facets. Cleaved facets provide an ideal mirror, but are not practical for device integration. Dry etched facets, on the other hand, have the advantages of having high throughput, with whole wafer processing possibility, allowing for accurate control of etch depth, and allowing for smooth and vertical facets [111]. By optimizing the reactive elements used to perform the etching, the power sources, and the chamber pressure, I have obtained results nearly identical to those obtained with cleaved facets. Furthermore, to increase temperature stability, a superlattice structure, consisting of alternating pairs of wide and narrow bandgap materials, was integrated into the laser heterostructure. The superlattice, in

conjunction with tunnel injection and p-type modulation doping allows for high temperature stability. These lasers are being integrated with tapered optical waveguides.

### 6.1.2 Experiment

The quantum dot laser heterostructure, grown by molecular beam epitaxy on a (001) GaAs substrate, is shown in Fig. 6.1 The active region consists of seven quantum dot layers to provide sufficient gain at high temperatures. Each layer consists of p-doped InAs quantum dots capped with an $In_{0.15}Ga_{0.85}As$ strain reducing layer, and an InGaAs tunnel injector well. In the operation of the laser, injected electrons first thermalize into the injector layer, from which they are transported to the quantum dots by phonon-assisted tunneling [112]. A superlattice structure, consisting of ten alternating GaAs/AlGaAs pairs was incorporated into the active region, shown in Fig. 6.1, which also shows the reflectivity of the superlattice, simulated by transfer matrix method [113-114]. I further optimized the structure by using GRINSCH and a reduced thickness of the GaAs spacer to increase the confinement factor (Γ). The separate confinement heterostructure (SCH) QD ridge waveguide is fabricated by standard photolithography, dry etching, and metallization techniques.

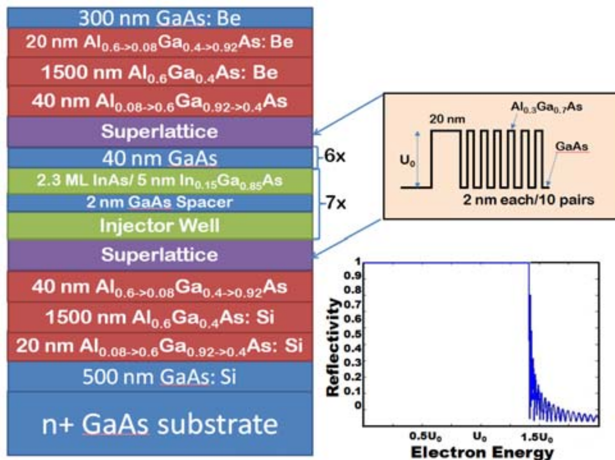


Fig. 6.1 The quantum dot laser heterostrucutre incorporates modulation p-doping of the dot, tunnel injection, and a superlattice structure. A detailed plot of the superlative band diagram, and simulated electron electivity are also shown.

### 6.1.3 Results and Discussion

The superlattice structure is simulated by transfer matrix method [114]. A series of thin alternating pairs of GaAs and $Al_{0.3}Ga_{0.7}As$ pairs form the superlattice structure. A detailed plot of the actual and effective band structures is shown in Fig. 6.2. The thin alternating pairs form a barrier which is larger than that of the barrier material itself. In this case electrons with energies < 1.5 times the barrier energy are blocked and not able to pass through the barrier. Due to the confined nature of the superlattice, if the thick initial layer is ignored, a miniband of allowed energy states is present in the band structure which would allow the electrons to tunnel through. However, this thick initial barrier prevents tunneling at energies less than the barrier height. A similar structure is grown on the other side of the waveguide core to prevent the escape of holes. Although this structure partially inhibits carrier injection, the confinement of carrier is much better, leading to slightly higher threshold but much more temperature insensitive performance.

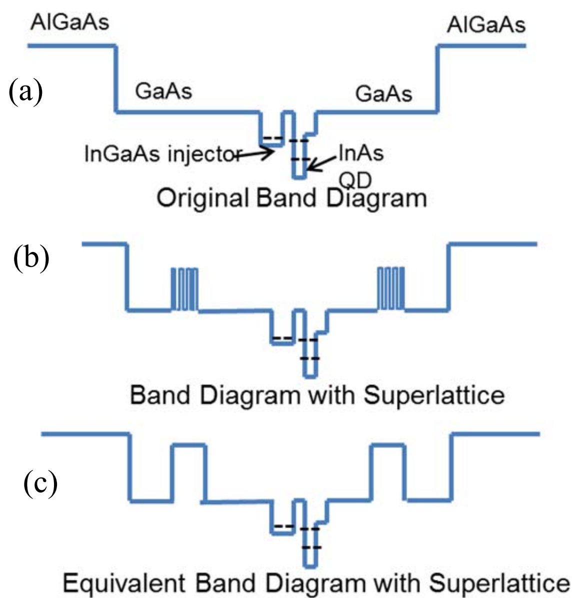


Fig. 6.2 (a) At high temperatures, electrons are able to escape the active region in a structure without a superlattice. (b) The band structure of the superlattice. (c) The superlattice has an effectively higher barrier than the AlGaAs material itself, and the initial barrier blocks low energy ($<U_0$) electrons from tunneling through the superlattice.

Gallium arsenide can be effectively cleaved leaving atomically smooth planes, suitable as the mirror for a standard Fabry Pérot lasers, with the power reflectivity given by:

$$R = \left(\frac{n_1 - n_2}{n_1 + n_2}\right)^2 \tag{6.1}$$

where $n_1$ is the effective index of the mode inside the laser, and $n_2$ is the index of the material the light is transmitted into, in general: air. In a GaAs based laser, the power reflection at an air interface is ~0.32. This reflection allows for ~68% of the laser power incident at the facet to be transmitted, while reflecting 32% back into the laser cavity. The relatively high reflectivity of this interface reduces the mirror loss, and therefor also reduces the threshold. However, facet cleaving has several drawbacks. It does not allow for full wafer processing. Each column of lasers must be cleaved independently. Additionally, cleaving restricts lasers in the same column to have the same cavity length. Devices cannot be cleaved independently. For these two reasons, cleaving is not suitable for creating optical systems which can be integrated on silicon chips. Dry etching, on the other hand, can overcome these disadvantages. An entire wafer can be processed simultaneously. Additionally, because the locations of the facets can be defined using photolithography, individual devices can have varying cavity lengths regardless of their spacial relationship to one another. Using dry etching would allow an array of lasers to be fabricated with varying cavity lengths. If the gain medium is carefully designed, as in chapter 4, the lasers can be designed to emit at different wavelengths, simply from differences in the cavity length.

In order to study the characteristics of a device with dry etched facets, I fabricated

devices with dual (ideal) cleaved facets, devices with a single dry etched facet with the other being cleaved, and also devices with dual dry etched facets. To perform the dry etching, I use $Cl_2$+Ar+$BCl_3$. Argon is mainly a physical etchant, and it serves to create vertical sidewalls. However, due to the physical nature of this etching, argon alone would create very rough facets, with high scattering loss. To reduce surface roughness, I include $Cl_2$ and $BCl_3$ in the etching, which are primarily chemical etchants. These leave a much smoother sidewall, but unfortunately are isotropic, and cannot be used alone to create vertical sidewalls. I optimized the direct current (DC) and inductively coupled power (ICP) power supplies and the chamber pressure to get both smooth and vertical sidewalls, as shown in the SEM, in figure 6.3. Additionally, I tried deliberately roughening a facet, as shown in the SEM in Fig. 6.4 (a). To remove this roughness, I next used an HBr based wet chemical solution to further polish the facet of the intentionally roughened facet. The SEM in Fig. 6.4 (b) shows the roughness is removed, yielding a high quality mirror facet.

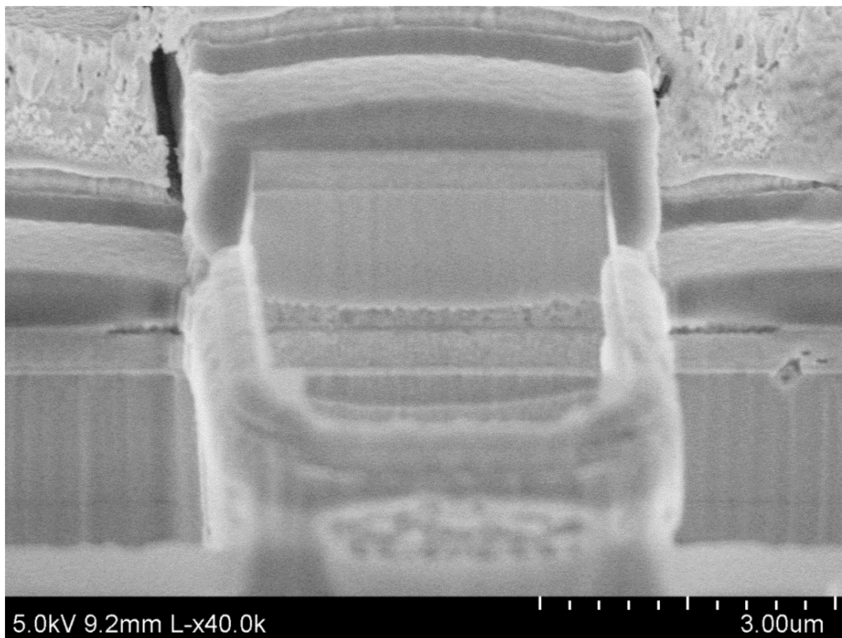


Figure 6.3 A smooth dry etched facet is created using a $Cl_2$+Ar+$BCl_3$ dry etching recipe.

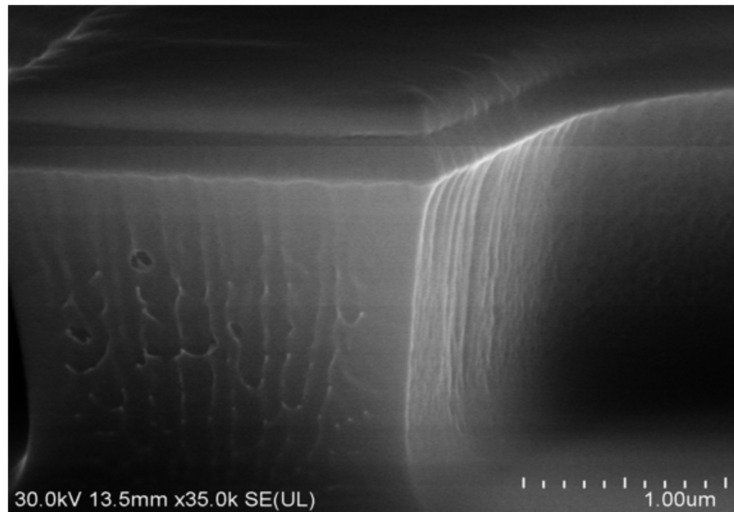


(a)

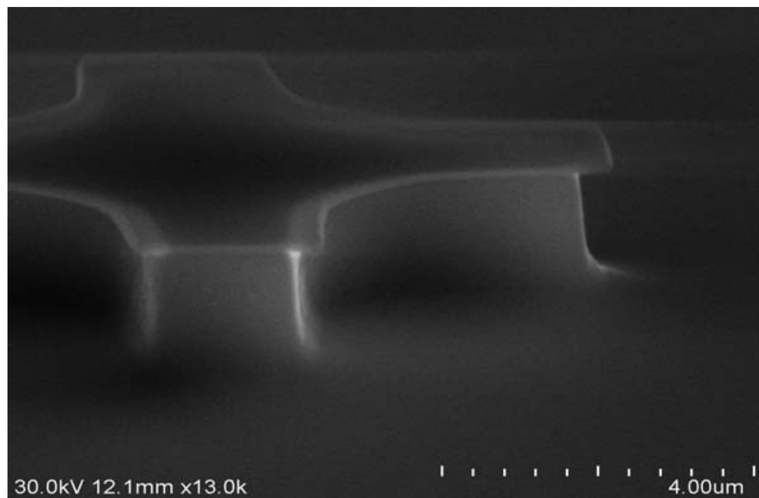


(b)

Fig. 6.4 (a) The facet is intentionally roughened using a non-optimized dry etching recipe. (b) I use an HBr based wet chemical etching to polish the roughened facet, leaving smooth facet, which can serve as a good laser cavity mirror.

An unfortunate drawback of dry-etching the facets is that they cannot be made atomically smooth as is the case with the cleaved facet. Surface roughness causes a

scattering loss, effectively reducing the facet reflectivity. This reduction in reflectivity increases the mirror loss of the cavity, increasing the threshold of the laser, as described by the formula [115]:

$$J_{th}(L) = J_{th}(\infty) + \frac{C}{2L} \ln\left(\frac{1}{R_1 R_2}\right) \tag{6.2}$$

where $J_{th}$ is the threshold current density of the laser, L is the cavity length, and $R_1$ and $R_2$ are the reflectivities of the two facets, which are known for a cleaved GaAs/air facet. By measuring the value of threshold for varying cavity lengths, I can fit the values of $J_{th}(\infty)$, and C. Next, when one facet is dry etched, I can use the calculated values of C and $J_{th}(\infty)$ to fit the reflectivity, given the threshold current density of the device. Using this method, I calculate the facet reflectivity of a single dry etched facet, using the dry etching process outlined above, to be ~0.25, which is close to, but not as good as a cleaved mirror facet.

Although it is not possible to create ideal facets using dry etching, I were able to successfully fabricate lasers with dry etched facets, comparable to those with two cleaved facets. Next, I will compare the performance of the lasers with single and dual dry etched facets with those of the dual cleaved facets discussed in chapter 2. Ridge waveguide lasers were fabricated with cleaved laser facets. These lasers show a light emission wavelength at 1304 nm, as shown in the EL spectrum, in Fig. 6.5 (a). These lasers had a threshold current of 32 mA at room temperature, as shown in the L-I-V in Fig. 6.5 (b). The temperature dependence of the devices is shown in Fig. 6.5(c). The incorporation of the superlattice allows for the devices to exhibit near temperature insensitive performance between 5-60$^{o}$C, with $T_0$ and $T_1$ ~$\infty$.

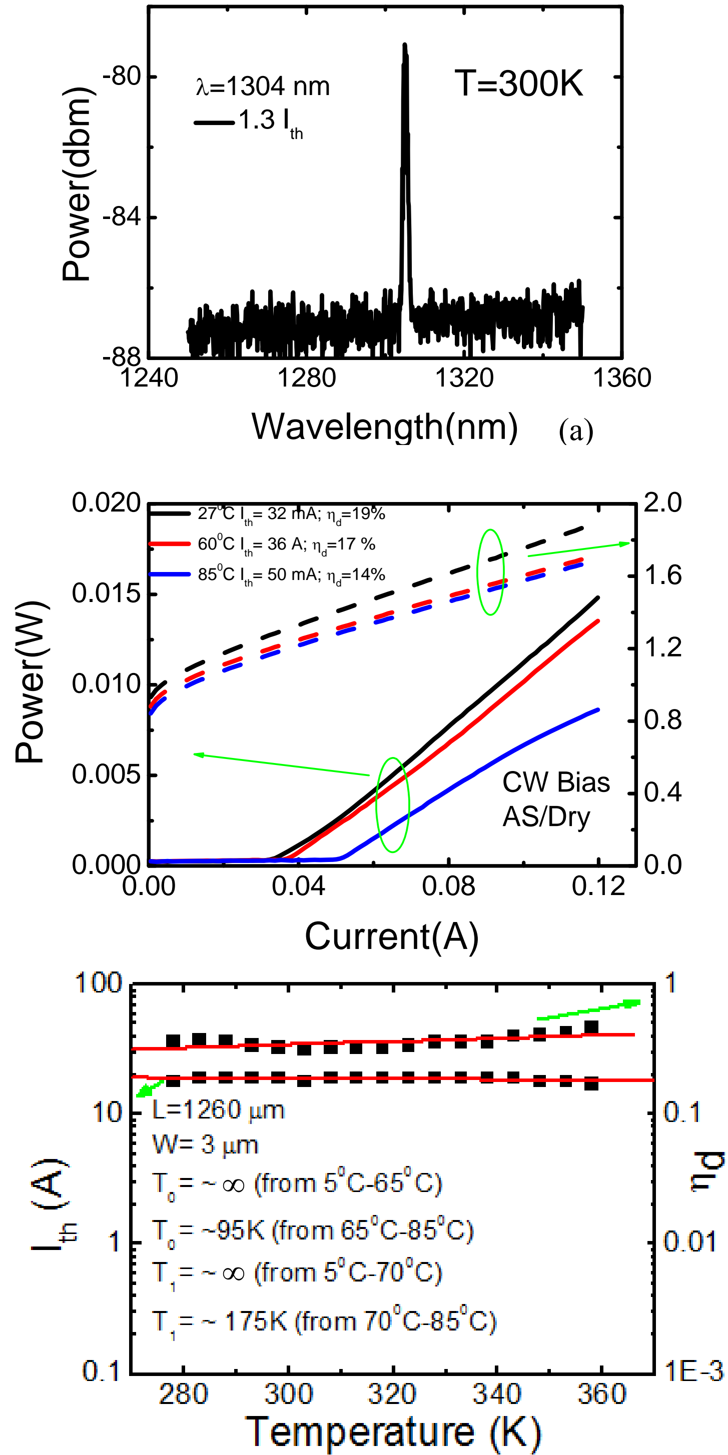


Fig. 6.5 (a) The electroluminescence shows a lasing wavelength of 1304 nm. (b) The L-I-V characteristics are shown as a function of temperature. (c) The temperature dependence of threshold and external quantum efficiency are shown.

For further integration applicability, I studied dual dry etched facet lasers and shortened the cavity length from 1260 um to 700 um. These devices are characterized by a threshold current of 23 mA under CW bias at room temperature, which compares well with the cleaved devices. The L-I-V characteristics are shown in Fig. 6.6 (a), with the temperature stability shown in Fig. 6.6 (b). These devices are also characterized by excellent temperature stability with $T_0$ and $T_1 \sim \infty$ between $5^o$-$50^oC$. These results are comparable to the cleaved lasers under pulsed bias. However, I can see thermal roll off under CW bias at 65ºC. I may need to further improve the dry etching recipe or increase the cavity length to fix this.

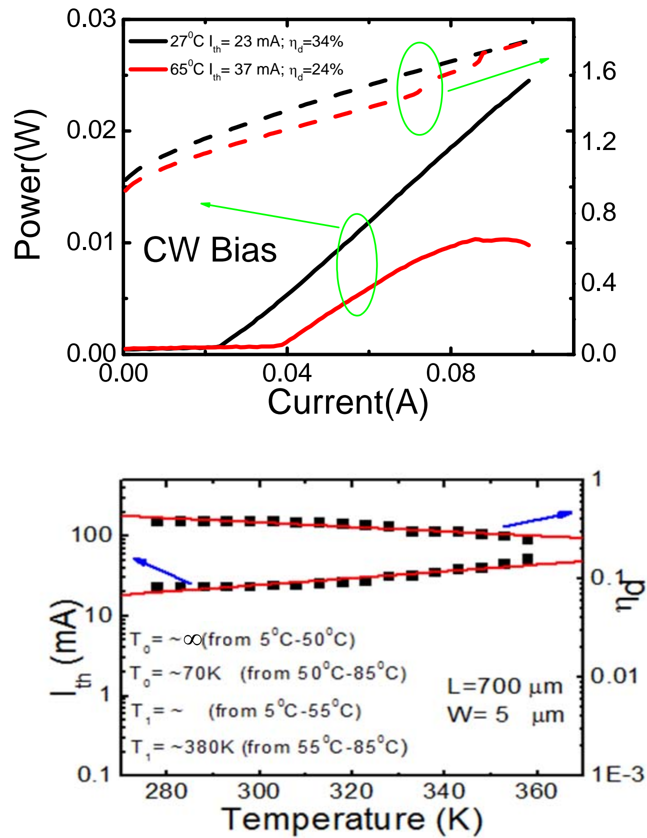


∞

Fig. 6.6 (a) Light-current-voltage characteristics of a laser with both facets dry etched (b) The temperature stability in the same device.

### 6.1.4 Conclusion

In conclusion, I demonstrate excellent temperature stability by introducing a superlattice into the laser heterostructure, which greatly improves carrier confinement. Additionally, I developed a dry etching recipe which allows for the fabrication of facets which are comparable to those of ideal cleaved facets. Dry etching facets also has the advantages of having a large throughput, with whole wafer processing possible, and it allows for all devices to have independently controlled cavity lengths. Using our new dry etching recipe, I fabricated lasers with single and dual dry etched facets, and compared their performance to cleaved lasers using the same heterostructure. The dry etched devices are very comparable to the cleaved lasers.

## 6.2 1.3 µm Quantum Dot Lasers Integrated with Silicon Nitride Waveguides

### 6.2.1 Introduction

Robust photonic integrated circuits (PICs) capable of operating at high temperatures with low power consumption, low delay, and good signal integrity will be essential for future on-chip communication [116]. An important element of such PICs is a low-loss monolithically integrated waveguide/directional coupler which can couple and/or transfer information from the laser to the CMOS chip. The waveguide should be designed to couple as much power from the laser as possible, to minimize the propagation loss, and to only support a single mode. Silicon nitride waveguides provide a relatively large index to effectively guide the laser contrast power without creating a large propagation loss, which is proportional to $\Delta n^2$ [116]. I have successfully designed, fabricated, and analyzed silicon

nitride waveguides coupled to quantum dot lasers using low temperature processing techniques conducive with high performance laser processing and also with traditional CMOS processing which would allow these devices to be integrated on chip and used for optical interconnects. I demonstrate a novel method for the analysis of the loss mechanism associated with the integrated waveguide. While traditional waveguide analysis uses an external laser, I use the integrated laser which allows us to fit the groove parameters and characterize the waveguide by its waveguide loss in terms of its coupling loss, taper loss and propagation loss. Previously reported silicon nitride waveguides have used isolated devices without the integration of an optical source with the waveguide [117-118]. These devices were measured with an external laser due to the high temperature treatment used to fabricate the waveguides (~1200$^{o}$C) which is not compatible with an integrated laser [119]. I report the design and characteristics of a coupled InAs QD laser and silicon nitride waveguide system, fabricated on the same chip. Additionally, I model the losses of the system including the coupling from the laser to the waveguide, the propagation loss, and the tapering loss created by tapering the waveguide to single mode dimensions. Additionally, the system shows temperature insensitive performance ($T_0$~∞) over the temperature range 5$^{o}$C to 50$^{o}$C.

### 6.2.2 Design and Experiment

The waveguide coupling and tapering losses were calculated using beam propagation method (using BeamPROP$^{TM}$), and the dimensions were designed in order to minimize these losses. The laser heterostructure is presented in figure 6.7 (a), and the coupling groove is shown in figure 6.7 (b) The ridge width of the laser was chosen to be 4 µm wide

in order to provide sufficient power, while minimizing the power present in higher order spacial modes. I first simulate the transmission of the laser's output power into the waveguide ($|S_{21}|^2$), the reflectivity of the groove ($|S_{11}|^2$).

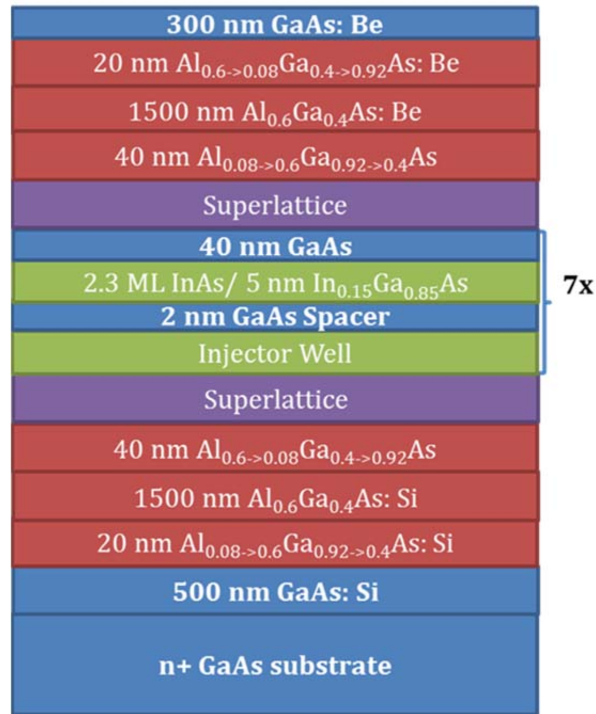


(a)

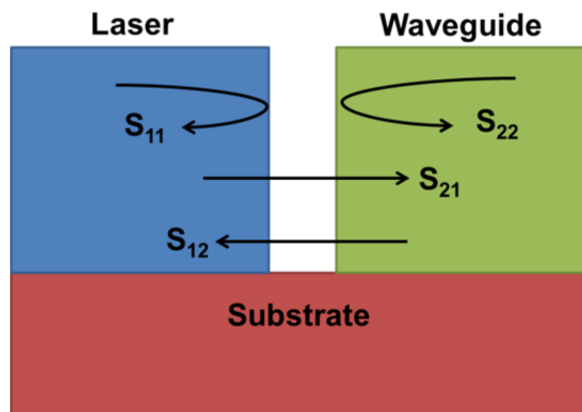


(b)

Figure 6.7. (a) The quantum dot laser heterostructure used as the integrated optical source with the waveguides. (b) I wish to maintain a high laser reflectivity ($S_{11}$) in order to minimize the laser threshold, while coupling as much of the remaining power as possible ($S_{21}$).

The power reflectivity of an ideal cleaved facet is ~0.32. I chose the groove to provide as close to this reflectivity as possible. This allows the laser threshold to be as closed to a free standing device as possible, and allows for substantial coupling between the laser and the waveguide. Figure 6.8 (a) shows the reflectivity of the laser as a function of groove width (blue), along with the transmission of the laser output into the waveguide (green). For comparison, the power which is not reflected is plotted (red) so the power lost, that is the power which is neither coupled back into the waveguide nor reflected back into the laser, can be seen. Ideally all the power which is not reflected back into the laser cavity should be coupled into the waveguide. However, due to the far field radiation spreading, some of the power is radiated away from the waveguide and the laser, which is particularly problematic as the groove width is increased. In order to minimize the radiated power, the waveguide is designed to be wider than the laser. Figure 6.8 (b) shows the increase of the coupling as the waveguide is made wider. The increase is particularly noticeable for the 2 μm laser where the far field angle is wider. To minimize the radiation loss in the groove, and also to account for any misalignment issues during the device fabrication, the starting width of the waveguide was chosen to be 8 μm.

An additional requirement for integrated waveguides to be used as optical interconnects is for their output to only support a single spacial mode. Higher order modes are characterized by varying effective indices, $n_{eff}$, and therefore propagate at different velocities, causing dispersion in the output signal if multiple modes are supported in the waveguide. In order to ensure single mode output, the waveguide must be designed so that its dimensions are below those of the cutoffs for higher order modes at 1.3 μm. Given the silicon nitride (n=1.98) and silicon dioxide (n=1.45) waveguide

structure, 800 nm is chosen to be the final width of the waveguide in order to ensure single mode output. Because the height of the waveguide cannot easily be tapered, its value is chosen to be a constant 750nm. As a note, this is around double the laser's active region thickness. This small dimension causes a large radiation pattern out of the laser, but fortunately, due to the close proximity of the laser to the waveguide, most of the power will still be able to be coupled into the waveguide. I chose a groove width of 2.1 μm which is characterized by a reflectivity of 0.32, close to the ideal cleaved facet reflectivity, while minimizing the power loss due to the far field angle in both the transverse and lateral laser direction

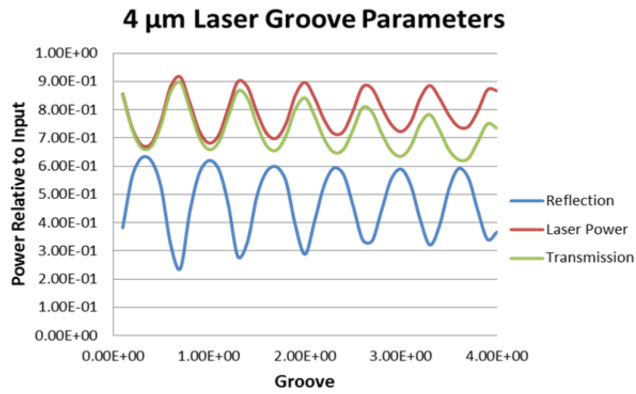


(a)

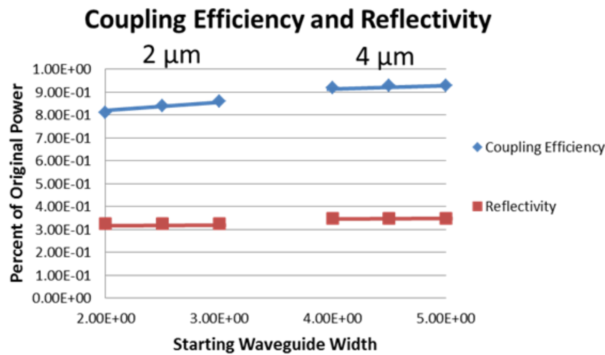


(b)

Fig. 6.8. (a)The laser reflectivity and transmission are simulated and plotted as function of groove width. (b) As the width of the waveguide is made wider, the coupled power increases. This particularly important for smaller lasers which have a greater divergence angle, and for wider grooves.

While the width of the silicon nitride waveguide core cannot easily be tapered, the width can be tapered using standard photolithography techniques. In order to minimize the tapering loss while still creating a single mode waveguide, the tapering is done over a long distance (100 μm). This tapered region is followed by a constant 800 nm width region, from which I will derive the propagation and insertion losses. The overall system is shown in figure 6.9.

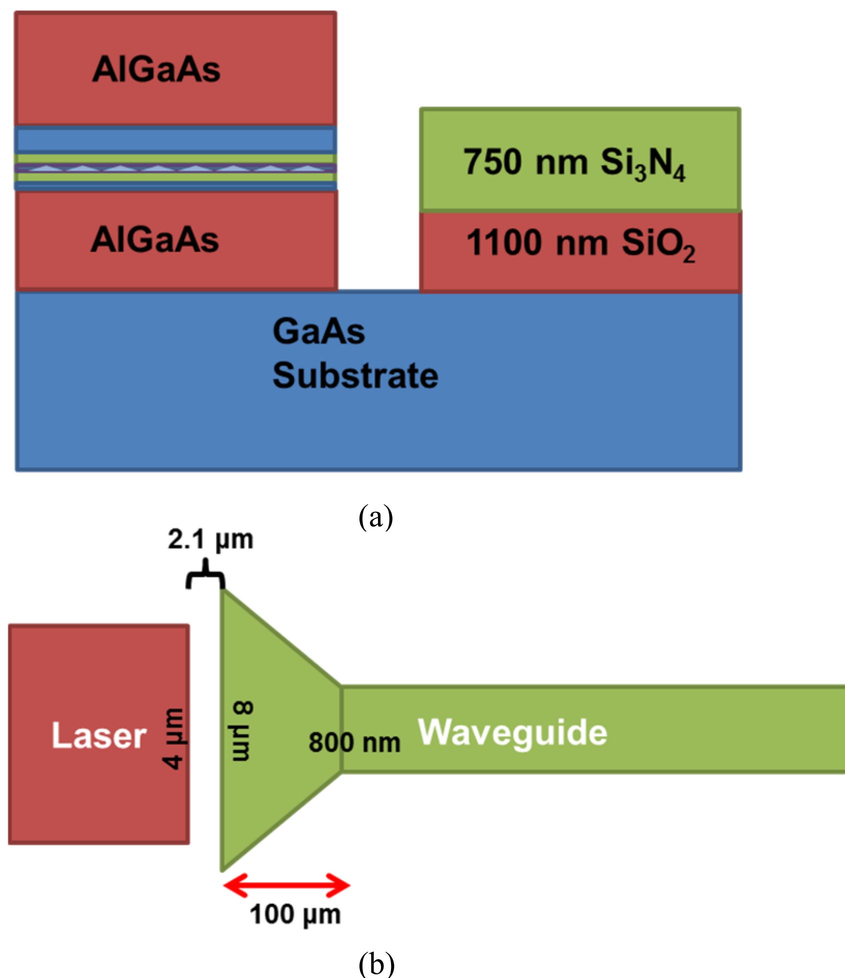


Fig. 6.9 (a) The side view of the system showing the coupled laser/waveguide system, separated by a 2.1 μm coupling groove. (b) The overhead view of the system with a 4μm laser coupled to an 8μm waveguide, which is subsequently tapered to 800 nm.

The waveguide and the coupling groove were fabricated using a new processing technique which allows us to easily remove the sidewall coating between the laser and waveguide. I first deposit the $Si_3N_4$/SiO2 waveguide using plasma enhanced chemical vapor deposition (PECVD). However, this tool also coats the sidewall of the laser, leaving a thick (~4 μm) layer of $SiO_2$ which cannot easily be removed when processing the groove. The sidewall coating with an index of 1.45 (compared with n=1 for air) produces a faster oscillation in the reflectivity and transmission, as seen in Fig. 6.8 (a), whose period is $\lambda/2n$, where n is the index of the groove material. This means the groove is more sensitive to slight changes in width. Additionally, this reduces the index difference between the laser and the groove, reducing the reflectivity which can be achieved. For these reason, I chose to use air as the groove material. I demonstrate a way to naturally crack the sidewall coating. First I deposit the $SiO_2$ and $Si_3N_4$ using PECVD. Next, I perform standard photolithology to create the tapered waveguide geometry in the silicon nitride core. Next, I etch vias in the $SiO_2$ to make electrical contacts with the laser, and then deposit the contact metal. Finally, I etch the laser facet and the sidewall will naturally crack due to its large aspect ratio, as confirmed by SEM images taken of the groove.

### 6.2.3 Results and Discussion

SEM images of waveguide and the coupled waveguide/laser system are shown in figure 6.10. An overhead view of the laser and waveguide is shown in Fig. 6.10 (a), while the tip of the waveguide is shown in Fig. 6.10 (b)

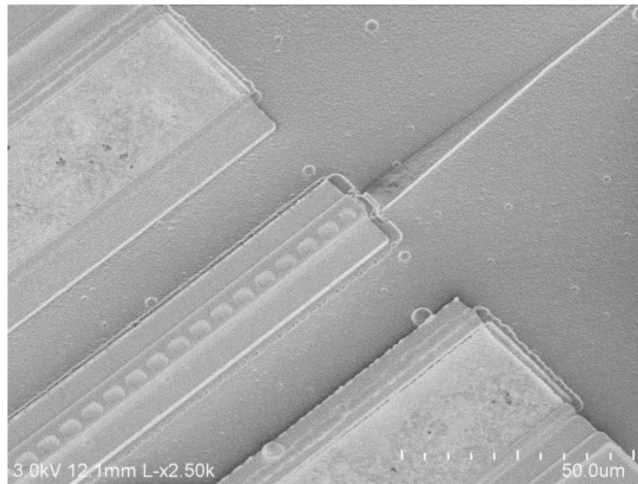


(a)

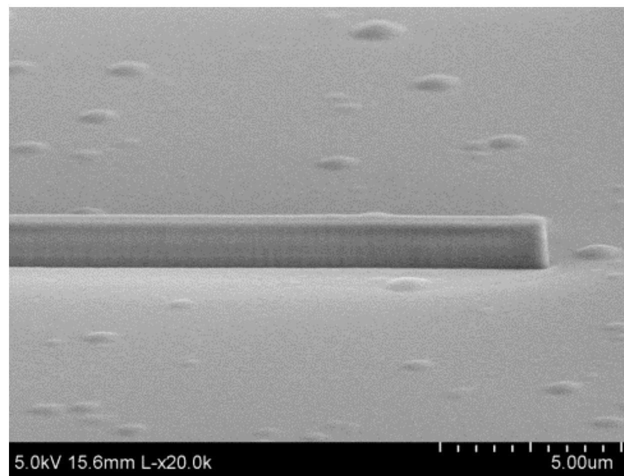


(b)

Fig. 6.10 (a) The waveguide is coupled to the laser by a dry etched groove of ~2.1 μm to provide reflectivity similar to that of a cleaved laser facet. (b) The tip of the waveguide is made 800 nm wide in order to prevent the propagation of higher order modes.

The laser spectrum is presented in figure 6.11 (a). It shows a pure single mode at 1298 nm at $1.4I_{th}$. Light-current from the cleaved laser facet and from the waveguide facet are shown in figure 6.11 (b), along with the temperature dependent threshold measurements in 6.12 (c). The lasers are characterized by a threshold of 51 mA for a device with a laser length of 1200 μm, and a waveguide length of 220 μm. The laser is

characterized by $T_0$~∞ from 5 to 50°C, and $T_0$~60 K from 55 to 85°C. In addition, by varying the cavity length, the reflectivity of the groove can be fit by using the formula 6.2 from which values of $J_{th}(\infty)$=725 A/cm$^2$ and C=33.52 A/cm are derived, as shown in Figure 6.12(d).

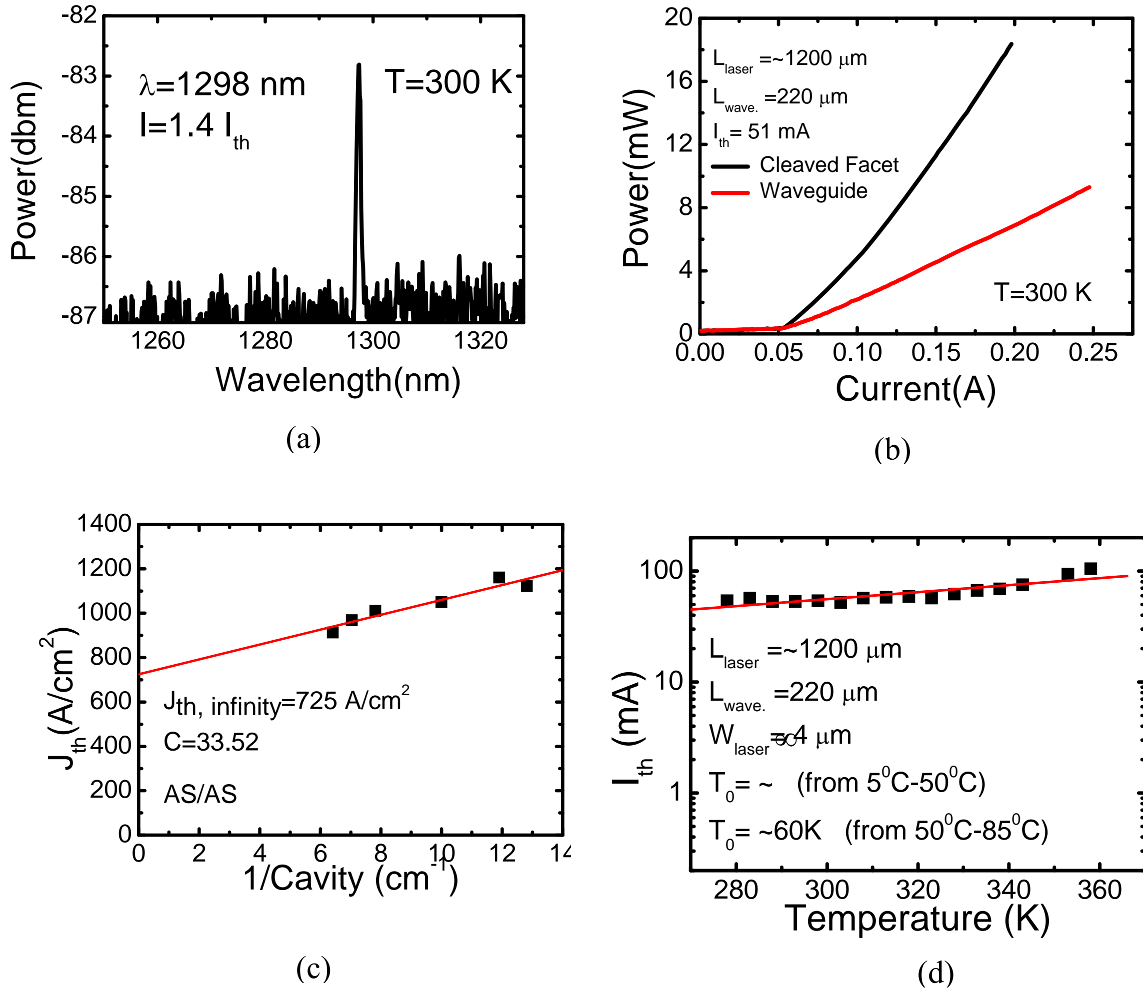


Fig. 6.11 (a) The output spectrum shows a single mode at 1.298 µm at 1.4 $I_{th}$ at 300K. (b) The L-I measurements demonstrate the excellent coupling from the laser into the waveguide. (c) Temperature dependent threshold measurement show excellent temperature stability with $T_0$~∞ from 5-55°C. (d) From the fitting of $J_{th}(\infty)$, and C, the reflectivity of the dry etched groove facet can be calculated for each device.

Three devices were fabricated with different length of the constant 800 nm width region, all using the same tapered waveguide section, with device A having waveguide length $L_A$=100 μm, device B with waveguide length $L_B$=160 μm, and device C with waveguide length $L_C$=220 μm. The three devices had threshold current densities of 1069, 972, and 1028 A/cm$^2$, corresponding to groove reflectivities of 28%, 54%, and 38%, respectively, using Eqn. 6.3. The output power from the waveguide can be compared with the output power from the cleaved laser facet using the following relationship [120]

$$|S_{21}|^2 = \frac{P_2}{P_1}\left|\frac{1 - S_{11}(1-t_3)^{0.5}t_2^2}{t_2}\right|^2 \left(\frac{t_1}{t_3}\right)^2 \quad (6.3)$$

where $|S_{21}|^2$ is the power transmission in the groove from the laser to the waveguide, $P_1$ and $P_2$ are the measured powers from the laser and waveguide, respectively, $t_1$ is the transmittance of the cleaved GaAs facet, and $t_3$ is the transmittance of the waveguide facet. The transmittance $t_2$ describes the transmission of the waveguide and is given by $t_2=\exp[(ik-\alpha/2)L]$. Under the condition that the transmission of the waveguide facet,$t_3$, is nearly 1, which is true given the relatively low index of silicon nitride relative to air, this equation simplifies to:

$$|S_{21}|^2 \approx \frac{P_2}{P_1}\left(\frac{t_1}{|t_2|t_3}\right)^2 \quad (6.4)$$

Combining the reflectivities calculated above with the power measurements from both the cleaved laser and waveguide facets, the loss inside the waveguide is calculated for the three devices with different waveguide lengths, and is shown in figure 6.12. From this data, I can obtain the power propagation loss of 11 dB/cm. This is higher than other reported values for several reasons: the waveguide is processed without using the high temperature treatments which are typically used but aren't compatible with the laser, and due to the extremely small dimensions (750x800 nm) of the $Si_3N_4$ core material which

greatly increases the propagation loss, which is proportional to w $^{-4}$. However, this waveguide is single mode. The insertion loss is measured and found to be 3.2 dB. This loss is a combination of power radiated away in the groove along with the tapering loss.

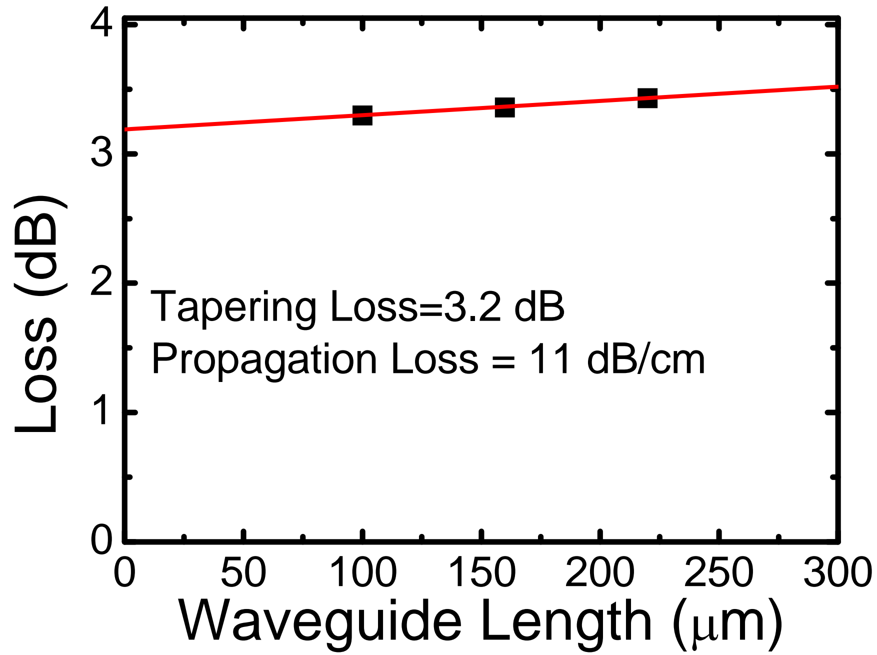


Fig. 6.12 The calculated propagation loss is 11 dB/cm. The insertion loss of 3.2 dB is largely due to the tapering loss, but is also contributed to by the radiated power in the groove.

Next from the measured propagation loss, the average surface roughness is calculated [121]. The average surface roughness is related to the propagation loss by the formula:

$$\alpha_{rougness} = \frac{4.34\sigma^2}{k_0\sqrt{2}d^4 n_c} gf(x) \tag{6.5}$$

Where σ is the RMS surface roughness, d is the width of the waveguide, and $n_c$ is the index of the core of the waveguide. g is given by:

$$g = \frac{U^2 V^2}{1+W} \quad (6.6)$$

where

$$U = k_0 d\sqrt{n_c^2 - n_{eff}^2} \quad (6.7)$$

$$V = k_0 d\sqrt{n_c^2 - n_{cl}^2} \quad (6.8)$$

$$W = k_0 d\sqrt{n_{eff}^2 - n_{cl}^2} \quad (6.9)$$

f(x) is related to the sidewall roughness and can be expressed in the following relationship:

$$f(x) = \frac{x\sqrt{1-x^2+\sqrt{(1+x^2)^2+2x^2\gamma^2}}}{\sqrt{(1+x^2)^2+2x^2\gamma^2}}$$

(6.10)

where

$$x = \frac{WL_c}{d} \quad (6.11)$$

$$\gamma = \frac{n_{cl}V}{n_c W\sqrt{\Delta}} \quad (6.12)$$

$$\Delta = \frac{n_c^2 - n_{cl}^2}{2n_c^2} \quad (6.13)$$

and where $L_c$ is the correlation length of the surface roughness.

The refractive indices of the deposited material, silicon dioxide and silicon nitride, were measured, and found to be $n_{cl}$=1.45 and $n_c$=1.98, respectively. Given the measured indices and waveguide dimensions, the effective index $n_{eff}$ is calculated to be 1.773 using BeamPROP. Given the known propagation loss, eqns. 6.5 can be solved numerically to

calculate the average surface roughness of $\sigma \approx 10$ nm given a correlation length of around 50 nm.

Next I approximate the tapering loss by calculating the loss of tapering an 8 μm waveguide to 800 nm over a length of 100 μm. This simulation is done in BeamPROP using the input mode calculated from the laser heterostructure. The tapering loss as a function of final tip width is presented in figure 6.13. This figure shows the transmission is near unity up until the waveguide is tapered to dimensions smaller than 1 μm. Given the single mode tip width of 800 nm, a tapering loss of 0.4 dB is determined for fundamental mode power. This does not include the scattering loss from the surface roughness. Additionally, the coupling loss is simulated to be 0.45 dB. It should be noted that this power lost only includes power in the fundamental mode. The dimensions of the waveguide were chosen such that higher order modes could not propagate, and so they experience very high loss in the tapered region. Any higher order mode power from the laser is converted to a propagated mode outside the waveguide instead of a guided mode. The total surface roughness loss is calculated by dividing the taper into many thin layers, and summing the surface roughness loss over each layer, and is found to be 0.8 dB. Removing the groove loss and the propagation loss, there is a total tapering loss of 2.15 dB, including the full conversion of higher order mode power to radiating power.

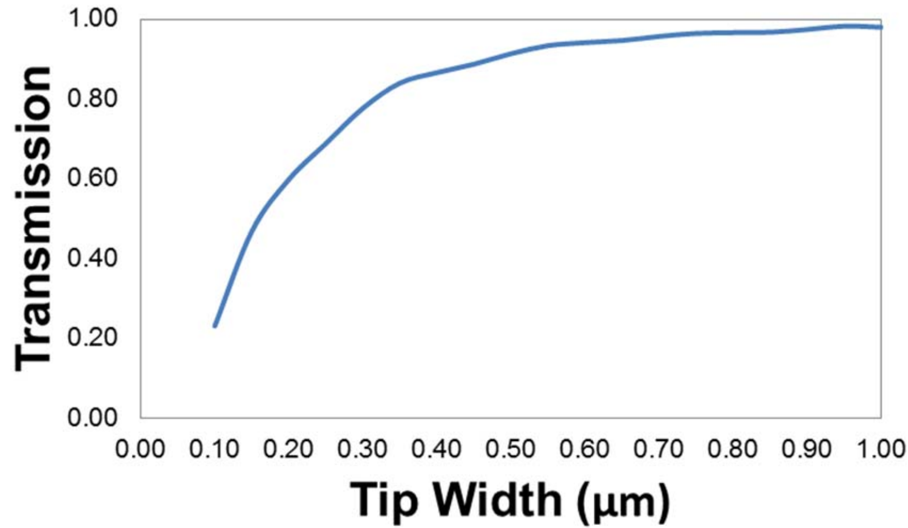


Fig. 6.13 as the width of the waveguide is tapered to narrower dimensions, more power is radiated away in the tapered region. Additionally, at ~800 nm, the waveguide is below the cutoff of the 1st higher order mode, so no power propagates in this mode.

In order to further minimize the loss of the waveguide, I designed a double tapered waveguide, as illustrated in Fig. 6.14. The tapering loss of the waveguide increases at narrower widths, as shown in Fig. 6.13, particularly when tapering to near or less than single mode conditions (w=800 nm). In order to overcome this loss, without the need to taper the laser over a long distance, I chose to use a double tapered laser, with two linear tapers. The first linear taper is from 8 μm to 2 μm over the relatively short distance of 75 μm. The next taper, to single mode dimensions (from 2 μm to 800 nm), was done over a distance of 125 μm. This waveguide used the same material system and process flow as the previously mentioned waveguides.

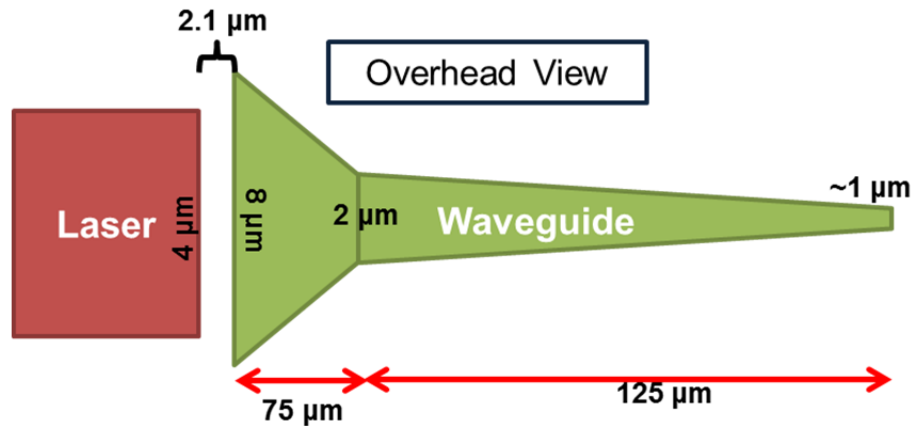


Fig. 6.14 Using a double tapered waveguide will allow for a reduced tapering and propagation loss.

In order to characterize the double tapered waveguide, I again measured the L-I characteristics of the device. For comparison, I chose a laser with as close to threshold of our single tapered waveguide laser as possible. With a similar threshold, the reflectivity of the groove is the same, as can be seen from eqn. 6.2. I plotted the L-I characteristics for both the laser with the single tapered waveguide and the laser with the double tapered waveguide with the same threshold. These results clearly show higher slope efficiency for this device. Additionally, the measured total loss, using the same analysis as above is found to be 2.75 dB. This is due to both the reduced tapering loss, and the reduced propagation loss. Using the calculated average surface roughness of 10 nm, I divided up the waveguide into many thin layers, and integrated the propagation loss over the length of the waveguide. I calculate a propagation loss of 0.7 dB, with a coupling loss of 0.4 dB, this leaves a tapering loss of 1.65 dB, which is 0.3 dB better than the single taper waveguide.

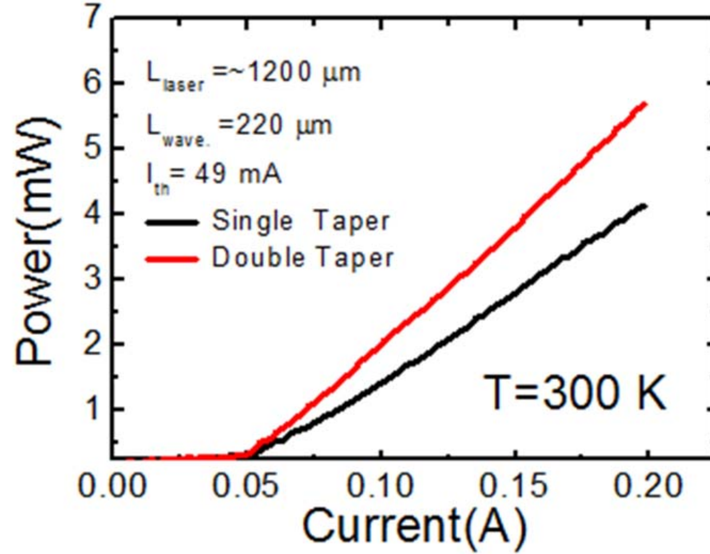


Fig. 6.15 L-I measurements from both single tapered and double tapered devices with comparable threshold, showing a higher slope efficiency in the double tapered device.

### 6.2.4 Conclusion

I have demonstrated a low loss, integrated silicon nitride waveguide coupled to a quantum dot laser. The waveguide was designed to maximize the coupled power from the laser, and was tapered in order to achieve single mode output. The insertion loss from the laser through the groove and the tapered region of the waveguide, including the radiated power lost in the groove, and the higher order mode power lost in the taper was found to be 3.2 dB. The propagation loss was found to 11 dB/cm, which corresponds to an average surface roughness of 10 nm with a correlation length of 50 nm. The relatively high values of loss are attributed to the lack of high temperature annealing which is not compatible with laser processing, and due to the small dimensions used to ensure single mode output. Given the calculated surface roughness values, I calculate the total scattering loss in both

the tapered and straight region of the waveguide to be 0.8 dB. From the waveguide simulations, I obtain a coupling loss of 0.45 dB, and a radiation loss in the taper of 0.4 dB. The remaining loss is likely due to the filtering out of higher order modes by the tapered region of the waveguide which tapers to a width below the cutoff of any higher order modes at 1.3 μm. This waveguide was successfully designed and integrated with a laser, using processing techniques compatible with both the laser processing and CMOS processing, making this process and the fabricated devices suitable for creating optical interconnects for future CPUs.

## 6.3 1.3 μm QD Cross Lasers with Integrated Silicon Nitride Waveguides

### 6.3.1 Introduction

While using a tapered waveguide does provide single mode output, the laser itself still produces power in higher order modes. Any power contained in these higher order modes is radiated away in the tapered region, and is effectively lost. While it may seem attractive to increase the width of the laser to get more power from it, this also reduces the threshold of higher order modes, and increases the percentage of the output power which is from these modes. An alternative then is to try to design a laser geometry which only supports a single optical mode. Using such a mode filtering laser, I are able to create both a high power device, and one which only supports a single optical mode. This allows us to use a non-tapered waveguide design while preserving the single mode output, reducing the propagation loss of the waveguide.

### 6.3.2 Design and Experiment

Several different geometries have been proposed and demonstrated as mode filtering structures. Figure 6.16 illustrates the two main types of filtering geometries from an overhead perspective. Figure 6.16 (a) shows a tapered geometry [122]. This wider laser is able to generate more power, but because the cavity includes the narrow region, higher order modes are not able overcome the total loss of the cavity, preventing lasing in these modes. The cross [123], as shown in figure 6.16 (b) geometry operates in a similar, but distinct manner, which will be discussed below.

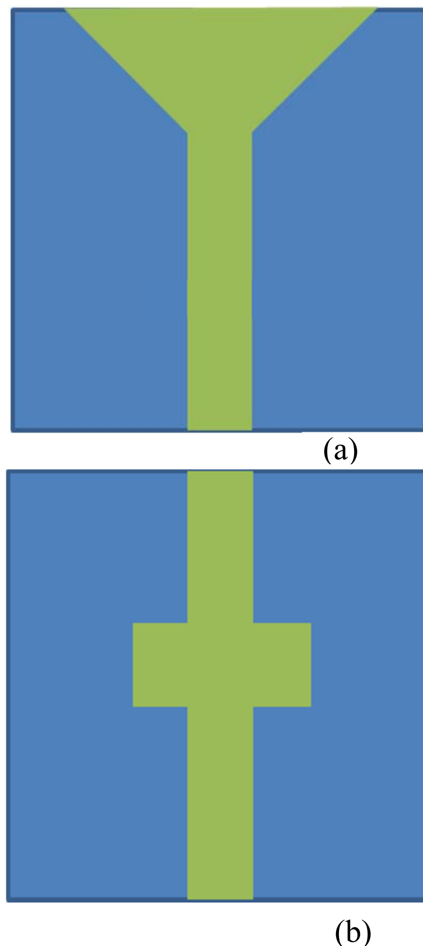


Fig. 6.16 Two possible mode filtering laser geometries, in an overhead view, with the green representing the laser cavity. (a) A tapered laser allows more power to be generated, but the narrow region prevents lasing in higher order modes. (b) The cross waveguide also induces a large loss in higher order modes.

A cross contains a standard ridge waveguide laser, with a relatively wider region contained within the middle of the ridge, as shown in Fig. 6.16 (b). When light reaches this wider region, it begins to expand as it propagates along the cross, as shown in figure 6.17. In this figure the mode is shown propagating through the cross from the bottom of the figure to the top. Once the mode reaches the other edge of the cross, it is forced to rapidly contract, inducing a relatively high loss that the mode must overcome in order to lase. The fundamental mode undergoes the least divergence as it propagates through this region, causing it to experience the least loss. The higher order modes, on the other hand, diverge relatively faster, and so the cross can be designed to minimize the loss in the fundamental mode, while maximizing the loss in the higher order modes.

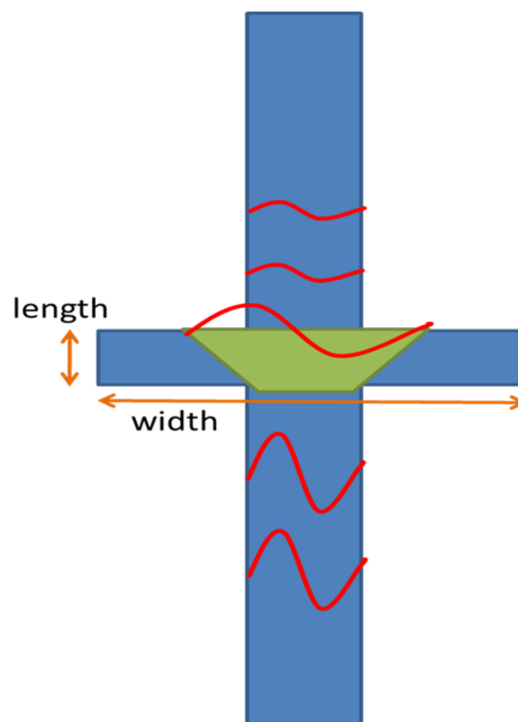


Fig. 6.17 shows how the mode propagates through the cross. Starting at bottom, as the mode enters the cross, it begins to expand. When the mode reaches the other edge of the cross, it is forced to rapidly contract, radiating a large portion of the power. This loss prevents the higher order modes from lasing. The fundamental mode diverges the slowest, and experiences the least loss.

The cross laser geometry was studied using the beam propagation method (using BeamPROP™), and the dimensions were designed in order to create the largest difference between the fundamental mode loss and the first higher order mode loss as possible. Each successively higher order mode diverges faster than the previous mode, meaning modes with even higher orders will experience a still larger loss, and therefore be even less likely to lase. For this reason, I only considered the loss in the fundamental mode and the first higher order mode. The laser heterostructure was the same as the previous devices in this chapter, and is shown in figure 6.7 (a). I first simulated how the cross length and widths affect the performance.

The width of the wider region of the ridge simply needs to be chosen to be wide enough to allow for the mode to continue expanding inside that region. Fig. 6.18 shows the power lost by both the fundamental mode and the higher order modes passing through a cross as function of length, for 2, 3, 4, and 5µm wide ridges. The width of the cross was fixed at 30 µm, and this was checked to ensure that the mode expansion didn't saturate for any of the lengths. This is true for these designs due to the relatively small divergence in both the fundamental and higher order modes at these dimensions. These figures show how a cross can be designed to present a small loss in the fundamental mode, and large loss in the higher order modes. For example, using a ridge width of 4µm, and a cross length and width of 30 µm provides a relatively small loss in the fundamental mode of 4%, and relatively high loss in the first higher order mode of 65%. This large difference can be to help prevent the higher order modes from reaching lasing conditions, with a minimal increase in threshold of the fundamental mode.

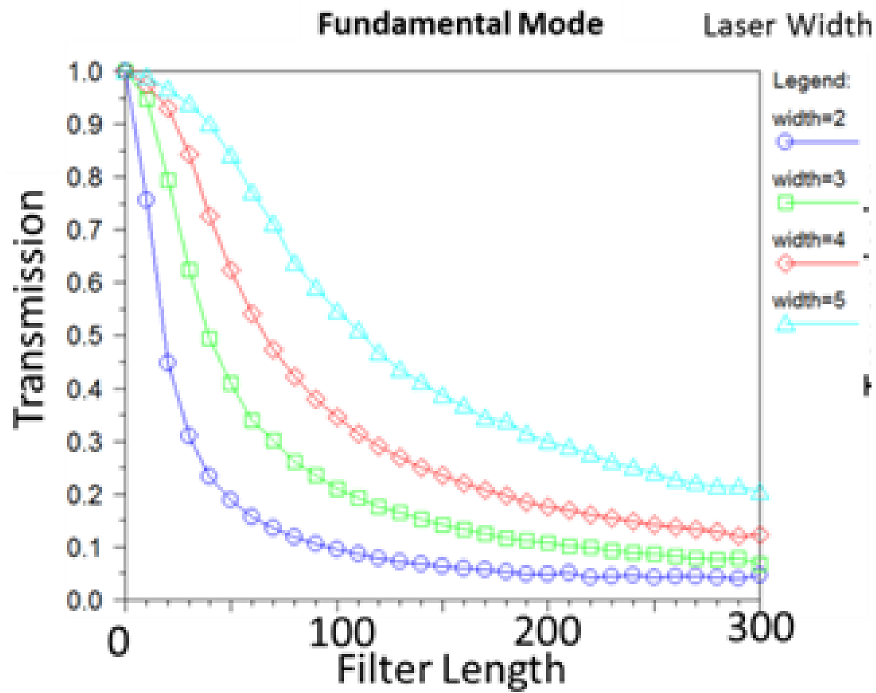


(a)

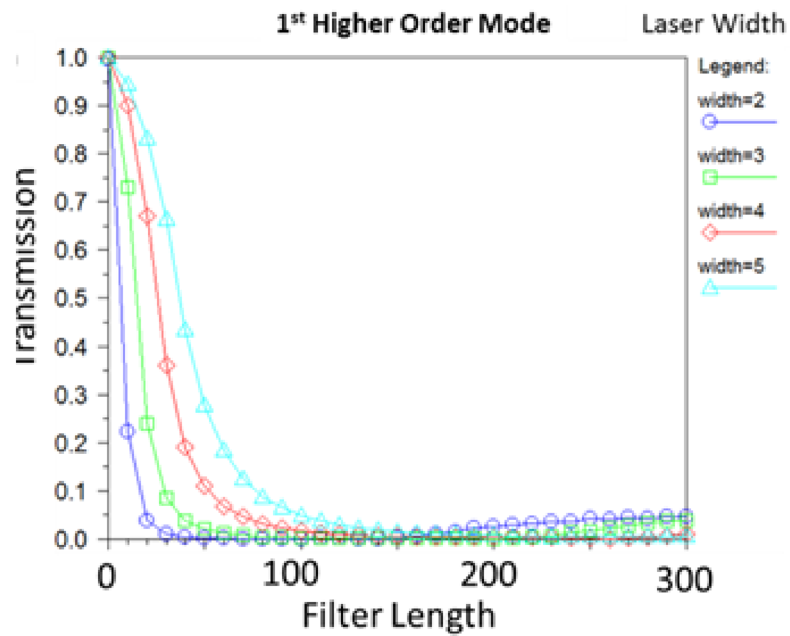


(b)

Fig 6.18. The transmission of the fundamental mode (a) and first higher order mode (b) are presented as a function of cross length. The width of the filter is kept constant at 30 μm.

I further investigated the properties of the cross structure, by creating a novel new cross structure incorporating two major changes from the standard cross geometry, illustrated in Fig. 6.19. I have chosen to fabricate 10μm wide lasers in order to ensure higher order mode lasing (in devices without the mode filters). First, this cross uses a hexagonal filter region instead of a sharp transition. This is used to help reduce the loss in the fundamental mode. The gradual taper allows the fundamental mode, which has diverged less, time to contract back into the ridge region. The higher order modes, on the other hand which have diverged much more than the fundamental mode, will not be able to fully contact, still inducing a loss, despite the taper. Due to limitations on our mask maker, I fixed the taper angle at $45^{o}$ to ensure that the cross geometry could be accurately created, without discontinuities at the interfaces which would have created unwanted additional losses. To this end, I chose to fabricate a device which has a transition length of 30 μm. The constant width region of the waveguide was chosen to be 50 μm.

Fig. 6.19. The mode filter has gradual tapers, allowing the fundamental mode which has diverged less a short distance to contract back into the narrow region. Higher order modes have diverged too much for this to help, and still experience a large loss.

Another geometry which was investigated was the use of a partially etched cross, as depicted in Fig. 6.20. The mesa for the cross is etched higher than I typically fabricated in the previously discussed devices. In simulating the modes of the laser, it was found that

the fundamental mode sits higher into the ridge than the first higher order mode. The fundamental mode experiences a greater compression from the ridge of the waveguide, and that the mesa was used as the cross, instead of the ridge itself. I determined, using BeamPROP, that if the mesa was etched at least 1100 nm from the top of the heterostructure, as shown in Fig. 6.20, then the fundamental mode would be confined by the ridge, regardless of the width of the mesa. I also determined that the first higher order mode is only confined by the ridge if the mesa etched at least 1400 nm from the top of the mesa. In our final design, I chose to etch the mesa 1200 nm from the top of the heterostructure. This will minimize the expansion of the fundamental mode, which will be confined by the ridge, but will still allow the 1$^{st}$ higher order to expand freely into the cross. This, in combination with the hexagonal mode filter should minimize the increase in the fundamental mode loss, minimizing the increase in threshold due to the cross structure. On the other hand, the relatively wide (70 μm) and long (50 μm constant with regions with two 30 μm tapers) will induce a very large loss in the higher order modes.

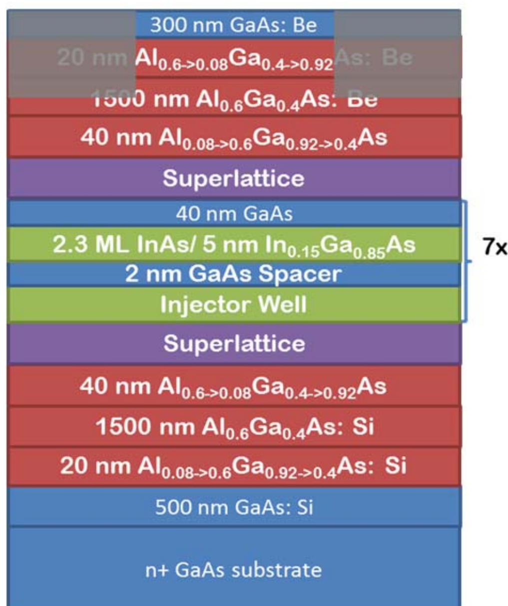


Fig. 6.20 Device heterostructure with the ridge illustrated. The greyed out region represented the material removed to form the ridge. The etch depth is chosen to be 1200μm in order to prevent fundamental mode divergence into the mesa

Ten micron wide lasers with such hexagon mode filters were fabricated, as shown in Fig. 6.21(a). The width of the laser ensures that there will be higher order modes [124]. The crosses were fabricated with constant width waveguides, using the same process as for the single mode waveguides, as shown in Fig. 6.21(b). These waveguides have a starting width of 12μm to capture as much light as possible. The waveguides were then tapered to a width of 5 μm over a length of 125 μm. This length is designed to be large enough as to render the tapering loss negligible. While the waveguide supports multiple modes, the laser does not produce or couple any higher order modes to the waveguide.

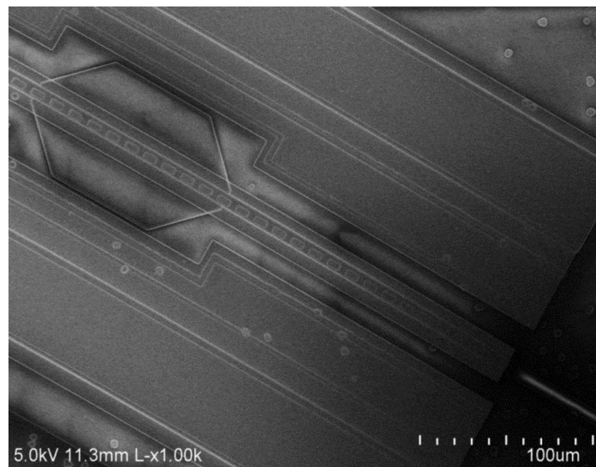


(a)

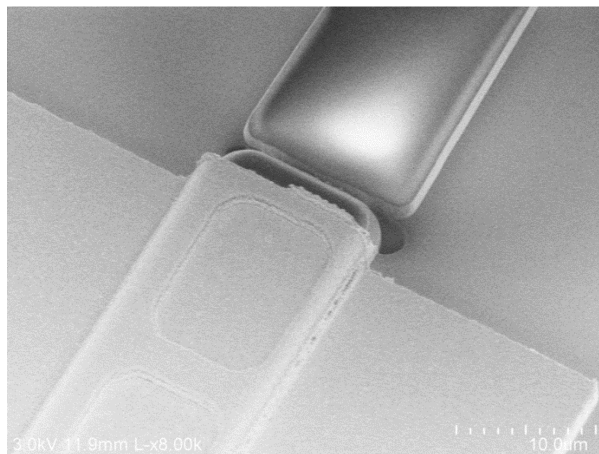

(b)

Fig. 6.21 (a) The hexagonal mode filter is added to the standard ridge waveguide laser to filter out higher order modes, which allows for the use of a wider, non-single mode waveguide. (b) The laser (right) is integrated with a silicon nitride waveguide (left).

### 6.3.3 Results and Discussion

The fabrication of the waveguide lead to a slight degradation in the performance of the laser, which was characterized by a threshold of 96 mA for the 10 µm wide ridge waveguide laser and 126 mA for the laser width the mode filter. However, the two lasers showed a near identical slope efficiency, as shown in Fig. 6.22 (a), with the temperature performance shown in Fig. 6.22(b).

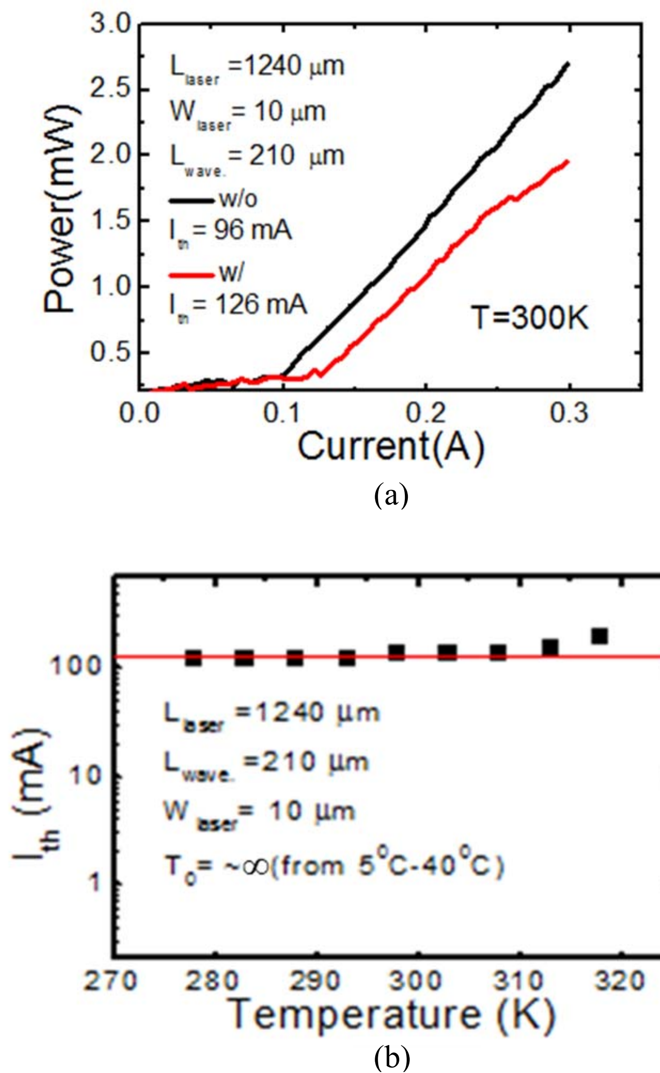


Fig. 6.22 (a) The laser with the mode filter (red) shows near identical slop efficiency as compared to a standard laser without the filter, and only a slight increase in threshold. (b) The mode filtered laser with integrated waveguide is characterized by near temperature insensitive performance with $T_0 \sim \infty$ between $5^oC$ to $40^oC$.

The spectrum of the device is shown in Fig. 6.23. The device was characterized by a peak light emission wavelength of 1305 nm. Overall, the waveguide processing did slightly degrade the performance of the laser, but only by a small amount. This confirms our belief that the hexagon shape and half etched mesa can be used to reduce the loss in the fundamental mode due to the filter.

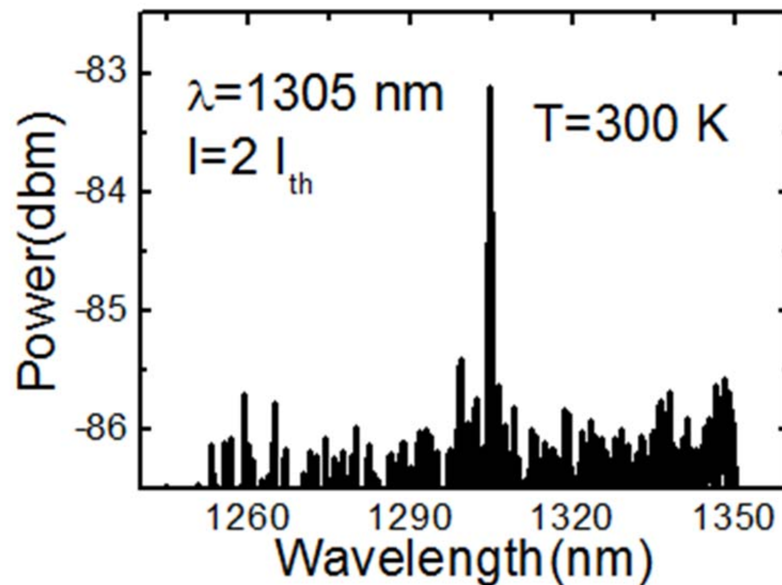


Figure 6.23 The spectrum from the mode filter laser shows a peak emission wavelength of 1305nm.

Next, I measured the far field mode profiles, to confirm our expectation that the cross mode filter increased the threshold of higher order modes. The mode profiles were captured as images, and then analyzed using Matlab. I captured the mode profile as a movie file, and then extracted a single image from the file of the measured mode. This mode image was imported into Matlab, and a cross section of the mode was taken at the peak of the mode intensity in the direction perpendicular to the growth direction, which is

the direction that the cross can filter out higher order modes. As expected, I do not observe any higher order modes in the direction parallel to the growth direction due to how thin the core of the laser active region is. An image of the mode profile, as captured by the camera, is shown in Fig. 6.24 for the mode filter laser.

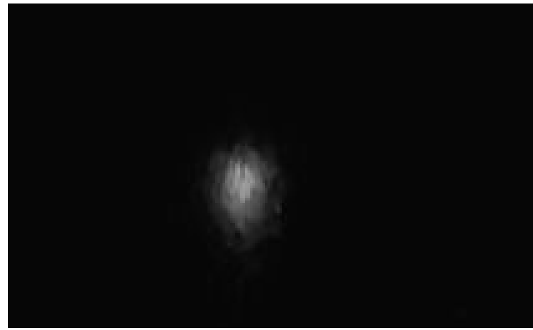

(a)

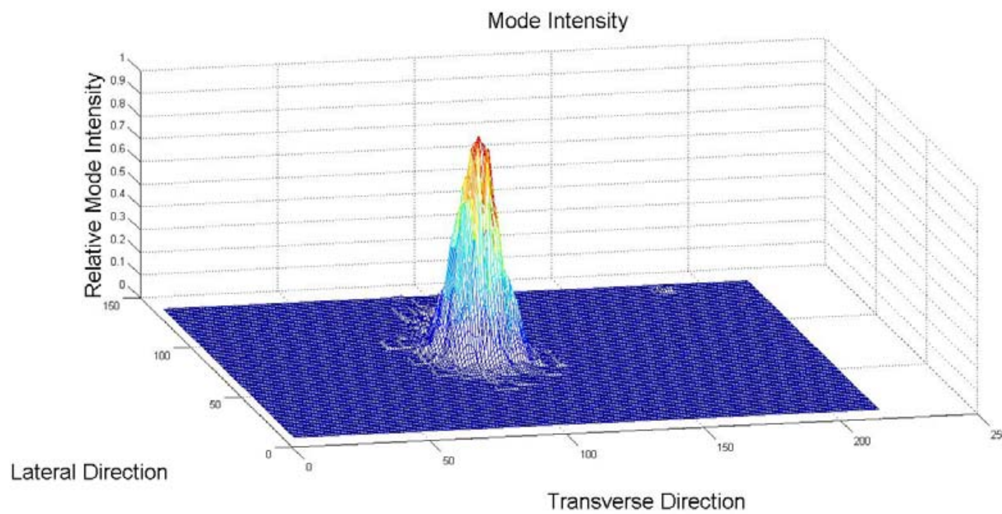


(b)

Fig. 6.24 (a) The measured mode profile of the laser as captured by the camera, and (b) a contour plot of the relative mode profile.

The standard ridge laser showed signs of higher order modes at a pumping current of 200 mA, as shown in Fig. 6.25(a). On the other hand, the mode filtered laser output a single mode up to 450 mA, as shown in Fig. 6.25(b). This device was single mode up to biases of more than twice that of the laser without the mode filter, although higher order

modes did start to become visible at 500 mA. This confirms our expectation that higher order modes can be filtered out using this new laser geometry. This serves several important benefits as opposed to tapering the waveguide to single mode dimensions. First the waveguide does not have to be tapered as narrow, which reduces the radiation loss in the fundamental mode. Second this will reduce the propagation loss inside the waveguide, which is proportional to $\Delta n^2$. Additionally, it prevents the wasted power caused by the laser lasing in higher order modes, which is removed by the taper.

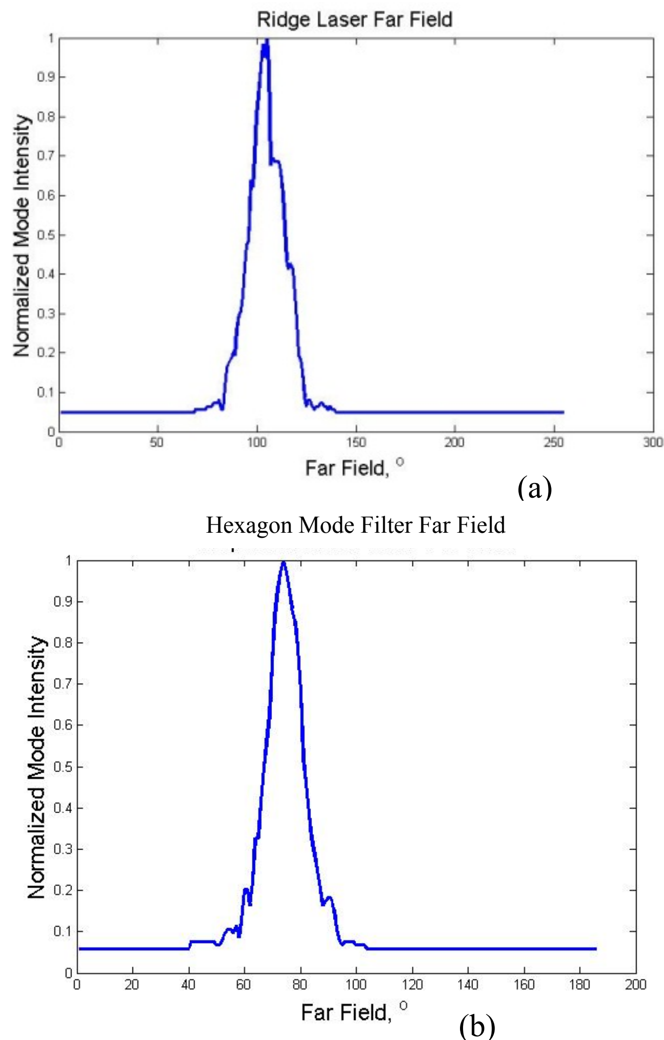


Figure 6.25 (a) The mode profile of the ridge laser at a bias of 200 mA showing a combination of multiple modes, and (b) the mode profile of the hexagon mode filter laser a bias of 450 mA, showing a single optical mode.

### 6.3.4 Conclusion

In conclusion, I were able to successfully fabricate a ridge laser with a hexagonal mode filter. This filter was designed to minimize the optical loss in the fundamental mode through the use of a tapered cross design which gives a short distance for the expanded mode to contract back into the ridge, minimizing the fundamental mode loss. The higher order modes, on the other hand, diverge more inside the mode filter, and are not able to contract fully, despite the taper. The expansion and rapid contraction of the higher order modes causes a portion of the mode to be unguided at the edges of the cross, and to radiate away. Additionally, I use a partially etched mesa to create a ridge structure which interacts more strongly with the fundamental mode. This further reduces the expansion of the fundamental mode, reducing its loss. This can be seen in the minimal increase in threshold of device fabricated with and without this mode filter. The mode filter laser showed a single longitudinal mode up to a bias of 450 mA, while the standard ridge showed higher order modes at a bias of 200 mA.

# Chapter 7
# Conclusions

## 7.1 Summary of Dissertation

In this thesis, I have studied the InAs/GaAs self-assembled QD lasers for chip to chip optical interconnects, including the requirements of such devices, and their implementation. A summary of the chapters is presented below.

### 7.1.1 Performance Characteristics of 1.3 µm Quantum Dot Lasers: Effect of Growth Parameters

I report the optimization of the growth conditions for InAs/$In_{0.15}Ga_{0.67}As$ quantum dots (QDs). The growth conditions include the V/III ratio for the core InAs QDs, and the growth interruption for the two steps growth. I found that low V/III ratio (40) during depositing the InAs QD seed layer can drastically suppress the formation of coalescent dots and improve the optical quality of the QDs. The two step growth with 5 seconds interruption time resulted in dense and uniform quantum dot formation. Overgrowing InGaAs on InAs QDs can enlarge the dot size and leads to red-shifting of the dots to 1300 nm. Using our optimized growth conditions, I obtained high-density QDs with strong PL emission. Finally, I fabricated a QD laser with 7-stacks of InAs/ $In_{0.15}Ga_{0.85}As$ QD grown using the optimized conditions. The cleaved 740 µm long ridge waveguide laser is characterized by an emission wavelength of 1304 nm and a threshold current density of

23 mA, under CW biasing and the measured temperature dependence of $I_{th}$ and $\eta_d$, from which values of $T_0$ and $T_1 \sim\infty$ in the temperature range of 5-60 $^oC$ is observed. Between 60-85$^oC$, $T_0$= 90 K and $T_1$=280 K. The obtained laser performance indicates the good material quality of the $InAs/In_{0.15}Ga_{0.85}As$ QDs.

### 7.1.2 High Speed 1.22 µm Tunnel Injection p-doped Quantum Dot Excited State Laser

The measured characteristics of excited state lasing in tunnel injection, p-doped, InAs quantum dot lasers were reported. Excited state lasing at 1.22 µm is ensured by a high-reflectivity facet coating which is designed to suppress ground state lasing in the devices. The saturation modal gain in the excited states is 56 $cm^{-1}$, which is a factor of ~2.5 higher than that of the ground state. The small-signal modulation bandwidth for I= $4.5I_{th}$ is 13.5 GHz and the differential gain is 1.1x $10^{-15}$ $cm^2$.

### 7.1.3 Quantum Dot Multichannel and Comb Lasers

I demonstrate a four channel, 1.3 µm range, tunnel injection, p-doped, chirp quantum dot (QD) laser by simply altering the cavity length of the lasers. All devices show near equal spacing (~5 nm) and threshold current using the ground states of the QDs. The lasers show high temperature stability with $T_0$~75 $^oC$ and $T_1$~270 $^oC$. Additionally, I fabricated an array of lasers, using In(Ga)As QDs in 1.2 µm range, which emitted in the ground state of the two types of QDs, but also the first excited state of the InAs QDs at 1.05 µm, again simply by altering the cavity lengths.

A high-speed multi-wavelength quantum dot comb laser, grown by molecular beam epitaxy, is demonstrated. The device is characterized by a 75.9 nm (FWHM) and a 91.4

nm ($\triangle_{-15dB}$) wide lasing spectrum. There are 105 and 185 simultaneously emitting longitudinal modes with a maximum channel intensity non-uniformity of less than 3 dB in the spectral range of 1231-1252 nm and 1274-1311 nm, respectively, for a laser with 1040 µm cavity length. The channel spacing can be tuned with cavity length and remains invariant in the temperature range of 300-323 K. The small signal modulation bandwidth is 7.5 GHz.

### 7.1.4 Distributed Feedback and Tunable Distributed Bragg Reflector Lasers with Quantum Dot Active Region

Single longitudinal mode quantum dot lasers are desirable for a photonic integrated circuit system. Using a single mode laser, such as DFB or DBR, will allow for multiple channels of closely spaced wavelength lasers to be modulated and their information sent on a single optical interconnect. Additionally, a single mode output, both optical and longitudinal, will reduce the dispersion of the optical signal and the corresponding signal degradation. I fabricated a half etched DFB laser, which is characterized by threshold current density of 258 A/cm$^2$, an external quantum efficiency of 43%, and a pure single mode at 1286 nm. I also fabricated a DBR with shallow metal grating, characterized by a threshold of 298 mA, and a side mode suppression ratio of 30 dB. Finally, I fabricated a tunable DBR using semiconductor gratings. A metal contact was placed on the edge of the grating to prevent fill in with metal, with metal lines on the top of the gratings remaining from the e-beam lithography step. This device is characterized by a tunable range of 4 nm, and a side mode suppression ratio of 25 dB. All devices were characterized by a temperature dependent wavelength shifting of 0.1 nm/$^o$C, which is a factor of five times lower than that of a standard InAs/GaAs FP QD laser.

### 7.1.5 Monolithic Integration of QD Lasers with Waveguides for High Temperature Operation

Cleaved facets, while they provide an ideal mirror for the ridge lasers, are not practical for integration with waveguides and it doesn't allow for whole wafer processing, has a low throughput, and doesn't allow for on chip testing. To this end, I developed a dry etching recipe which creates very vertical and smooth facets, with a calculated reflectivity of ~0.25, which is close to ideal reflectivity of a cleaved facet (0.32). I next designed and fabricated single mode integrated silicon nitride waveguides. The groove width is designed to provide as close to the reflectivity of a cleaved facet as possible, while the tapered width allows for as much light to be coupled from the laser to the waveguide as possible. In these devices, I measured a propagation loss of 11 dB/cm, and an insertion loss of 3.2 dB. Finally, I investigated the use of a mode filter on the laser as an alternative to using a tapered single mode laser. I were able to get a single mode output from the device at 450 mA as compared with 200 mA for a standard ridge, with comparable threshold currents.

## 7.2 Suggestions for Future Work

### 7.2.1 Integrated Single Optical and Longitudinal Mode Coupled Quantum Dot Laser-Waveguide System

An optical source, which is both single optical and single longitudinal mode, is desirable for the realization of a photonic integrated circuit scheme. This would allow for an array of lasers with closely spaced wavelengths, to be modulated and transmitted over a single optical interconnection, with each signal being dispersionless. While I have

fabricated individually single optical mode or single longitudinal mode, a coupled laser/waveguide system which presents both has not yet been fabricated. To that end, I propose a single an integrated system which is single longitudinal mode by the use of DFB or DBR laser. This laser should be coupled to a single mode fiber, which could be created using a tapered design. Fig. 7.1 shows a potential schematic for such a system with shallow grating. The use of a contact to this grating could allow for an array of identical lasers, with closely spaced emission wavelengths, which could fabricated, and used for on chip interconnects.

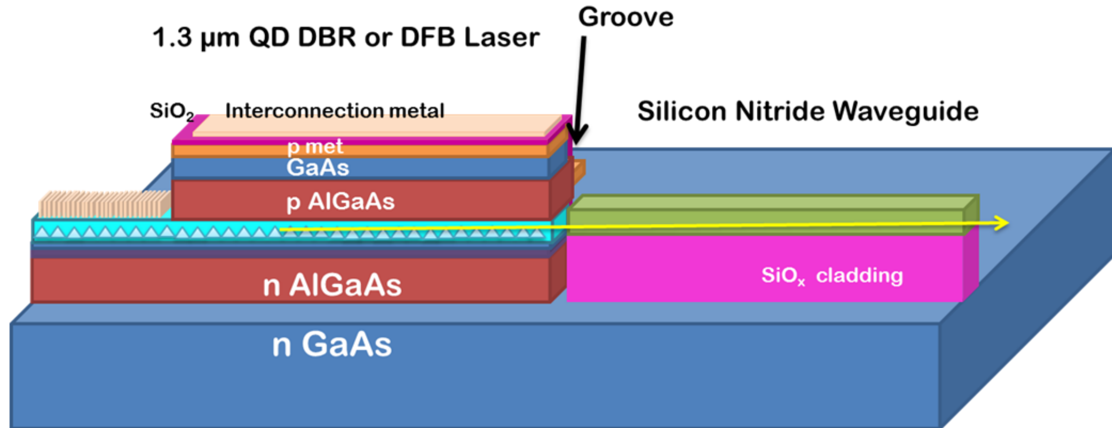


Fig. 7.1 A potential integration scheme of a single longitudinal mode DBR laser coupled to a tapered-to-single-mode silicon nitride waveguide.

### 7.2.2 Hybrid Integration of Quantum Dot Lasers with Coupled Waveguides

Silicon, with its indirect bandgap, is a poor light emitter, and is not suitable for producing coherent laser light, suitable for use in optical interconnects in CMOS circuits. A potential scheme for overcoming this limitation is shown in Fig. 7.2. The quantum dot laser with an integrated silicon nitride waveguide is fabricated, as described in chapter 6, except the waveguide tip must be squeezed to much smaller than single mode dimensions

(d≈100 nm). Surrounding the waveguide core, a polymer mode expansion (ME) is deposited. As the waveguide is tapered to narrower dimensions, more power leaks, and is guided by, the ME. The wafer is then flip-chip bonded onto a silicon wafer, with another waveguide and ME, which is placed in close proximity to the ME on the GaAs wafer. Through the evanescent mode coupling, the waveguide power is transmitted to the second ME, and then to the silicon nitride waveguide, with its relatively high index as compared with the ME (n=2.1 vs. 1.6). This hybrid integration scheme will allow for the realization of high performance optical interconnects.

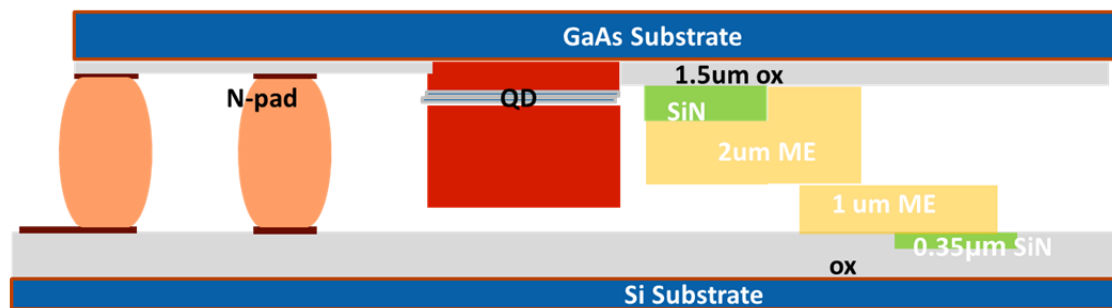


Fig. 7.2 The GaAs based QD laser is integrated with a silicon nitride waveguide, whose mode is coupled to another waveguide on the silicon wafer.

# Appendix A

## Fabrication of Silicon Nitride Waveguides with Dry Etched Coupling Grooves

The laser process was initiated using standard processing techniques. For the details, please refer to reference [125]. After the fabrication of the ridge, mesa, and the deposition of the n contact metal, the fabrication of the waveguide in initiated with deposition of the lower cladding.

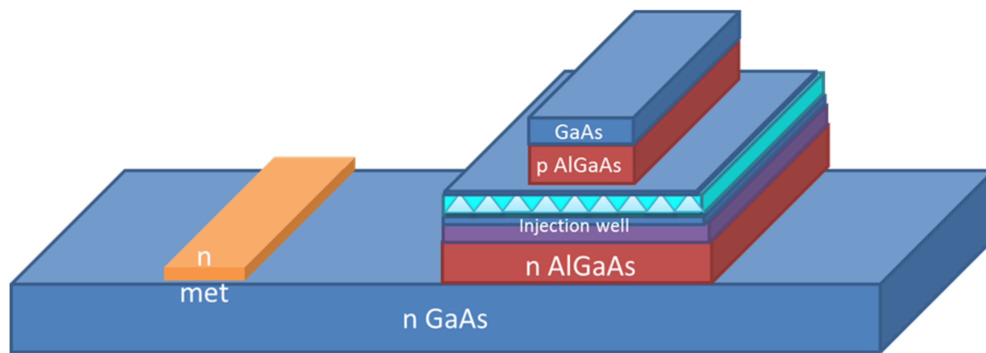


Fig. A.1 Laser device is processed using standard techniques.

First, the 1100 nm silicon dioxide lower cladding is deposited using PECVD. The deposition temperature is 350$^{o}$C. After the deposition of the silicon dioxide, the 830 nm silicon nitride core material is deposited. It is likewise deposited using PECVD at 350$^{o}$C.

After the deposition of the waveguide material, the waveguide is patterned using standard photolithography, using the GCA auto stepper. This is an I-line photolithography tool which uses a mercury arc lamp which allows for exposure sizes of

<1µm, which allows us to fabricate the narrow 800 nm tip of the waveguide. Then the $Si_3N_4$ waveguide core is etched using dry etching.

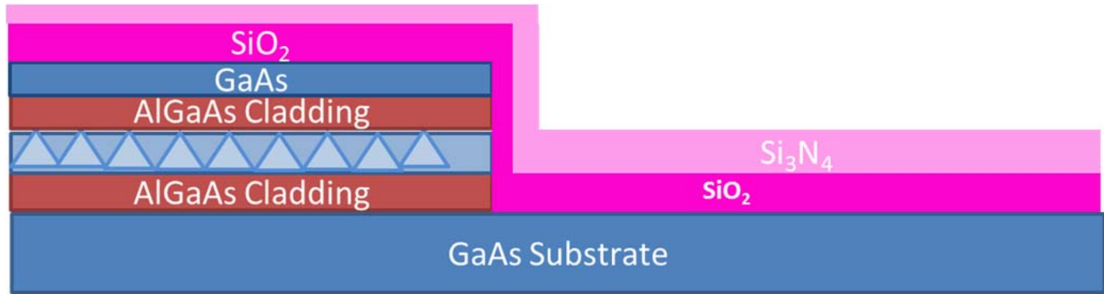


Fig. A.2 The $SiO_2$ cladding and $Si_3N_4$ core coat the sidewall of the laser. This is too thick to etch directly (~4 µm).

Next the vias are opened through the silicon dioxide above the laser for the interconnection. The top p-contact metal is deposited using an e-beam evaporator. The deposited metal is Ti/Pt/Ti/Au/Ti, with thickness of 500/500/500/8500/2000 Å, respectively. The contacts are annealed at 400°C to form the p-ohmic contact.

The laser facet is dry etched using $BCl_3$:$Cl_2$:Ar (5:2:8) as the source gases. The sample is dipped into Acetone, and ultrasound is used to naturally crack the sidewall coating. Finally, the sample is dipped into an HBr based wet chemical solution to further polish the laser facet.

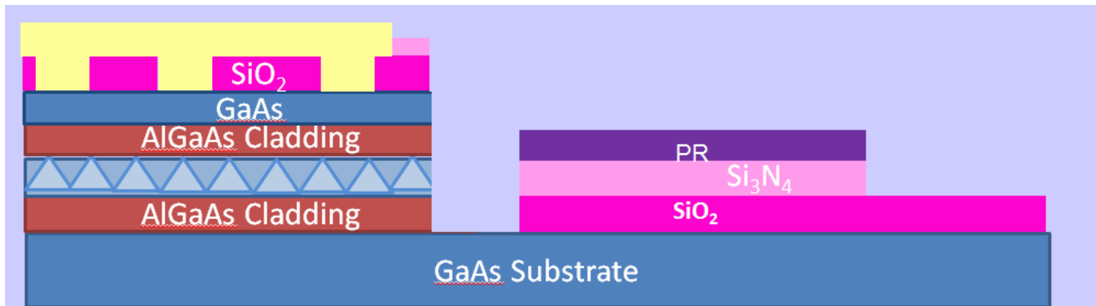


Fig. A.3 The laser facet is dry etched, and the sidewall coating is allowed to crack naturally.

# Bibliography


[1] I. A. Young, E. M. Mohammed, J. T. S. Liao, A. M. Kern, S. Palermo, B. A. Block, M. R. Reshotko, and P. Chang, Optical Technology for Energy Efficient I/O in High Performance Computing, *IEEE Comm. Mag.*, vol. 48, no.10, p. 184, Oct. (2010).

[2] ITRS-Roadmap Requests Additional Research in Alternative Interconnect Options. www.itrs.net

[3] I. A. Young, E. Mohammed, J. T. S. Liao, A. M. Kern, Member, S. Palermo, B. A. Block, M. R. Reshotko, and P. L.D. Chang, *IEEE J. Solid-State Circuits*, vol. 45, no. 1, p.235, (2010)

[4] David A. B. Miller, *Proceedings of the IEEE*, Vol. 97, no. 7, p.1166, (2009)

[5] M. J. R. Heck, H.W. Chen, A. W. Fang, Brian R. Koch, Di Liang, H. Park, M. N. Sysak, and J. E. Bowers, , *IEEE. J. Select. Topics Quantum Electron.*, vol. 17, no. 2 p. 333, (2011).

[6] [Online]. Available: http://www.itrs.net/Links/2007ITRS/ExecSum2007.pdf ,(2007)

[7] J. Ahn, M. Fiorentino, R. G. Beausoleil, N. Binkert, A. davis, D. Fattal, N. P. Jouppi, M. McLaren, C. M. Santori, R. S. Schreiber, S. M. Spillane, D. Vantrease, and Q. Xu, *Appl. Phys. A*, vol. 95, p. 989, (2009).

[8] Silicon Integrated Nanophotonics. http://domino.research.ibm.com/comm/research_projects.nsf/pages/photonics.index.html , (2010)

[9] Y. Arakawa and H. Sakaki, *Appl. Phys. Lett.*, vol. 40, p. 939, (1982).

[10] N. N. Ledentsov, M. Grundmann, F. Heinrichsdorff, D. Bimberg, V. M. Ustinov, A. E. Zhukov, M. V. Maximov, Zh. I. Alferov, and J. A. Lott, *IEEE. J. Select. Topics Quantum Electron.*, vol. 6, p. 439, (2000).

[11] M. Sugawara, Self-Assembled InGaAs/GaAs Quantum Dots. , Academic Press, (1999).

[12] I.R. Sellers, H.Y. Liu, K.M. Groom, D.T. Childs, D.Robbins, T.J. Badcock, M.Hopkinson, D.J. Mowbary and M.S. Skolnick, *Electron. Lett.*, vol. 40, p. 1412, (2004).

[13] D.G. Deppe, K. Shavritranuruk, G. Ozgur, H. Chen, and S. Freisem, *Electron Lett.*, vol. 45, p.154, (2009).

[14] M. Asada, Y. Miyamoto, and Y. Suematsu, *IEEE J. Quantum Electron.*, vol. 22 p. 1915, (1986).

[15] S. Fathpour, Z. Mi, P. Bhattacharya, A. R. Kovsh, S. S. Mikhrin, I. L. Krestnikov, A. V. Kozhukhov, and N. N. Ledentsov, *Appl. Phys. Lett.*, vol. 85, p. 5164, (2004).

[16] I.I. Novikov, N.Yu Gordeev, L. Ya. Karachinskii, M.V. Maksimov, Yu. M. Shernyakov, A.R. Kovsh, I. L. Krestnikov, A.V. Kozhukhov, S.S. Mikhrin and N.N Ledentsov, *Semicond.*, vol 39, p. 477, ( 2005).

[17] S. Fathpour, Z. Mi, and P. Bhattacharya, *J. Appl. Phys. D: Appl. Phys.,* vol, 38, p. 2103, (2005).

[18] N. Kirstaedter, N. N. Ledentsov, M. Grundmann, D. Bimberg, V. M. Ustinov, S. S. Ruvimov, M. V. Maximov, P. K. Kop'ev, Zh. I. Alferov, U. Richter, P. Werner, U. Gosele, and J. Heydenreich, *Electron. Lett.*, vol. 30, p. 1416, (1994).

[19] K. Kamath, P. Bhattacharya, T. Sosnowski, T. Norris, and J. Phillips, *Electron. Lett.*, vol. 32, no. 15, p. 1374 (1996).

[20] G. T. Liu, H. Li, K. J. Malloy, and L. F. Lester, *Electron. Lett.*, vol. 35, p. 1163, (1999).

[21] O. B. Shchekin and D. G. Deppe, *Appl. Phys. Lett.*, vol. 80, p. 3277,( 2002).

[22] K. Mukai, Y. Nakata, K. Otsubo, M. Sugawara, N. Yokoyama, and H.Ishikawa, *Appl. Phys. Lett.*, vol. 76, p. 3349, (2000).

[23] F. Y. Chang, C. C. Wu, and H. H. Lin, *Appl. Phys. Lett.,* vol. 82, p. 4477,( 2003).

[24] A. Stintz, G. T. Liu, H. Li, L. F. Lester, and K. J. Malloy, *IEEE Photon. Technol. Lett.*, vol. 12, p. 591,( 2000).

[25] K. Mukai, Y. Nakata, K. Otsubo, M. Sugawara, N. Yokoyama, and H. Ishikawa, *Appl. Phys. Lett* vol. 36, p.472, (2000).

[26] Y. Qiu, P. Gogna, S. Forouhar, A. Stintz, and L. F. Lester, *Appl. Phys. Lett.,* vol. 79, p. 3570, (2001).

[27] R. Krebs, F. Klope, J.P. Reithmaier, and A. Forchel, *Jpn. J. Appl. Phys.*, vol 41, p. 1158, (2002).

[28] A. R. Kovsh, N. A. Maleev, A. E. Zhukov, S. S. Mikhrin, A. P. Vasil'ev, E. A. Semenova, Yu. M. Shernyakov, M. V. Maximov, D. A. Livshits, V. M. Ustinov, N. N. Ledentsov, D. Bimberg, and Zh. I. Alferov, *J. Cryst. Growth*, vol. 251, p. 729, (2003).

[29] F. Y. Chang, J. D. Lee, and H. H. Lin, *Electron. Lett.*, vol. 40, p. 179, (2003).

[30] M. Grundmann, F. Heinrichsdorff, N. N. Ledentsov, C. Ribbat, D. Bimber, A. E. Zhukov, A. R. Kovsh, V. M. Ustinov, Zh. I. Alferov, *Jpn. J. Appl. Phys.* vol. 39, p.2341, (2000).

[31] D. L. Huffaker and D. G. Deppe, *Appl. Phys. Lett,* vol. 73, p.520, (1998).

[32] R. Songmuang, S. Kiravittaya, M. Sawadsaringkarn, S. Panyakeow, O.G. Schmidt, *J. Cryst. Growth* vol. 166 ,p. 251, (2003).

[33] J. Tatebayashi, N. Hatori, H. kakuma, H. Eba, H. Sudo, A. Kuramata, Y. Nakata, M. Sugawara, and Y. Arakawa, *Electron. Lett.* vol. 39, p.1130, (2003).

[34] A. Stintz, G. T. Liu, H. Li, L. F. Lester, and K. J. Malloy, *IEEE Photon. Technol. Lett.* vol.12, p. 591, (2000).

[35] H. Saito, K. Nishi, and S. Sugou, *Appl. Phys. Lett.* vol.73, p. 2742, (1998).

[36] K. Nishi, H. Saito, S. Sugou, and J. S. Lee, *Appl. Phys. Lett.* vol. 74, p. 1111, (1999).

[37] M. V. Maximov et al, *Phys. Rev. B*, vol. 62, p.16671 (2000).

[38] J. M. Ripalda, D. Granados, A. M. Sanchez S. I. Molina and J. M. Garcia, *Appl. Phys. Lett.,* vol. 87 , p.202108 (2005).

[39] V. A. Odnoblyudov, A. Yu. Egorov, N. V. Kryzhanovskaya, A. G. Gladyshev, V. V. Mamutin, A. F. Tsatsul'nlkov, and V. M. Ustinov, *Tech. Phys, Lett.* vol.28, p. 964, (2002).

[40] M. O. Lipinski, H. Schuler, O. G. Schmidt, K. Eberl, and N. Y. Jin-Phillipp, *Appl. Phys. Lett.* vol.77 , p.1789, (2000).

[41] N. N. Ledentsov, M. V. Maximov, D. Bimberg, T. Maka, C. M. Sotomayor Torres, I. V. Kochnev, I. L. Krestnikov, V. M. Lantratov, N. A. Cherkashin, Yu. M. Musikhin, and Zh. I. Alferov: *Semicond. Sci. Technol.* vol.15, p.604, (2000).

[42] H. Y. Liu, I. R. Sellers, T. J. Badcock, D. J. Mowbray, M. S. Skolnick K. M. Groom, M. Gutierrez, M. Hopkinson, J. S. Ng, J.P. R. David and Beanland: *Appl. Phys. Lett.* vol.85, p.704, (2004).

[43] H. C. Sun, L. Davis, S. Sethi, J. Singh, and P. Bhattacharya, *IEEE Photon. Techn. Lett.*, vol.5, no.8, p. 870, (1993)

[44] M. Geiger, A. Bauknecht, F. Adler, H. Schweizer, F. Scholz, *J. Crystal Growth* vol 170, p. 558, (1997).

[45] P. Bhattacharya, S. Ghosh, S. Pradhan, J. Singh, Z.-K. Wu, J. Urayama, K. Kim, and T. B. Norris, *IEEE J. Quantum Electron.*, vol. 39, p. 952, (2003).

[46] D. Klotzkin, K. Kamath, K. Vineberg, P. Bhattacharya, R. Murty, and J. Laskar, *IEEE Photonic. Tech. Lett.* vol. 10, p. 932 (1998).

[47] D. G. Deppe and D. L. Huffaker, *Appl. Phys. Lett.* vol. 77, p. 3325, (2000).

[48] O. B. Shchekin and D. G. Deppe, *Appl. Phys. Lett.* vol. 80, p. 3277, (2002).

[49] Y. Miyamoto, Y. Miyake, M. Asada, and Y. Suematsu, *IEEE J. Quantum Electron.*,vol. 25, p. 2001, (1989).

[50] L. Asryan, and S. Luryi, *IEEE Journal of Quantum Electronics*, vol.37, p .905, (2001).

[51] P. Bhattacharya and S. Ghosh, *Appl. Phys. Lett.*, vol. 80, no.19, p. 3482, (2002).

[52] D. G. Deppe, H.Huang, and O. B. Shchekin*IEEE J. Quantum Electron,* vol. 38, p. 1587, (2002).

[53] M. Gioannini, *Proc. SPIE*, vol. 5452, p. 526, (2004).

[54] D. L. Huffaker, G. Park, Z. Zou, O. B. Shchekin, and D. G. Deppe, *Appl. Phys, Lett.,* vol.73, p. 2564, (1998).

[55] F. Klopf, R. Krebs, J. P. Reithmaier, and A. Forchel, *IEEE Photon. Technol. Lett.*, vol. 13, p.764 (2001).

[56] A.R. Kovsh, N.A. Maleev, A.E. Zhukov, S.S. Mikhrin, A.P. Vasil'ev, E.A. Semenova, Yu.M. Shernyakov, M.V. Maximov, D.A. Livshits, V.M. Ustinov, N.N. Ledentsov, D. Bimberg, and Zh.I. Alferov, *J. Crystal Growth,* vol. 251, p.729, (2003).

[57] Z. Mi, P. Bhattacharya, and S. Fathpour, *Appl. Phys. Lett.* vol.86, p.153109, (2005).

[58] M. Sugawara N. Hatori, M. Ishida, H. Ebe, Y. Arakawa, T. Akiyama, K. Otsubo, T. Yamamoto, and Y. Nakata, *J. Appl. Phys. D: Appl. Phys.,* vol.38, p.2126, (2005).

[59] R. R. Alexander, D. T. D. Childs, H. Agarwal, K. M. Groom, H. Y. Liu, M. Hopkinson, R. A. Hogg, M. Ishida, T. Yamamoto, M. Sugawara, Y. Arakawa, T. J. Badcock, R. J. Royce, and D. J. Mowbray, *IEEE J. Quantum Electron.,* vol. 43, p.1129, (2007).

[60] D.G. Deppe, K. Shavritranuruk, G. Ozgur, H. Chen, and S. Freisem, *Electron Lett.* vol.45, p. 54, (2009).

[61] S. Fathpour, Z. Mi, and P. Bhattacharya, *IEEE Photon. Technol. Lett.*, vol.11, p.2250, (2005).

[62] S. M. Kim, Y. Wang, M. Keever, and J. S. Harris, *IEEE Photon. Technol. Lett.*, vol.16, p. 377, (2004).

[63] A. Capua, L. Rozenfeld, V. Mikhelashvili, G. Eisenstein, M. Kuntz, M. Laemmlin, and D. Bimberg, *Optics Express*. vol.15, p.5388, (2007).

[64] G. Park, O.B. Shchekin, and D. G. Deppe, *IEEE J. Quantum Electron*. vol.36, p.1065, (2000).

[65] K. Kim, T. B. Norris, S. Ghosh, J. Singh, and P. Bhattacharya, *Appl. Phys. Lett*. vol. 82, p.1959, (2003).

[66] O. Qasaimeh and H. Khanfar, *IEEE Proc-Optoelectron*. vol.151, p.143, (2004).

[67] B. J. Stevens, D. T. D. Childs, H. Shahid, and R. A. Hogg, *Appl. Phys. Lett.* vol.95, p.061101, (2009).

[68] P. Xu, T. Yang, H. Ji, Y. Cao, Y. Gu, Y. Liu, W. Ma, and Z. Wang, *J. Appl. Phys*, vol. 107, p.013102, (2010).

[69] S.W. Chang, S.L. Chuang, and N. Holonyak, Jr. *Phys. Rev. B,* vol.70, p.125312, (2004).

[70] P. N. Keating, *Phys. Rev.,* vol.145, p.637, (1966).

[71] R. M. Martin, *Phys. Rev.,* Vol.B1, p. 4005, (1969).

[72] H.T. Jiang and J. Singh, *Phys. Rev. B,* vol.56, p.4696, (1997).

[73] S. Fathpour, Z. Mi, and P. Bhattacharya, *Appl. Phys. Lett.*, vol. 85, p.5614, (2004).

[74] A. E. Zhukov, A. R. Kovsh, V. M. Ustinov, and Z. I. Alferov, *Semi. Lasers,* vol.13, p.319, (2003).

[75] A. E. Zhukov, A. R. Kovsh, V. M. Ustinov, A Y. Egorov, N. N. Ledentsov, A. F. Tsatsul'nikov, M. V. Maximov, Y. M. Shernyakov, V. I. Kopchatov, A. V. Lunev, P. S. Kop'ev, D. Bimberg and Z. I. Alferov, *Semicond. Sci. Technol*. vol. 14, p.118, (1999).

[76] C. Tong, D. Xu, and S. F. Yoon, *IEEE J. Lightwave Technol.,* vol.27, p.5442, (2009).

[77] A. Markus, J. X. Chen, C. Paranthoen, A. Fiore, C. Platz, and O. G. Lafaye, *Appl. Phys. Lett.*, vol. 82, p. 1818-1820, (2003).

[78] A. Markus, J. X. Chen, O. G. Lafaye, J. Guy, C. Paranthoen and A. Fiore, *IEEE Select. Topics Quantum Electron.*, vol. 9, p. 1308, (2003).

[79] G. Lin, C. Y. Chang, W. C. Tseng, C. P. Lee, K. F. Lin, R. Xuan, and J. Y. Chi, *Semicon. Laser Dynam. III,* vol. 6997, p. 69970R (2008).

[80] H.D. Yang, Q.Gong, S.G.Li, C.F.Cao, C.F.Xu, P.Chen, and S.L.Feng, *J. Crystal Growth*, vol. 312, p. 3451 (2010).

[81] J. Liu, Z. Lu, S. Raymond, P.J. Poole, P.J. Barrios, G. Pakulski, D. Poitras, *IEEE Photon. Technol. Lett.* vol. 20, p.81, (2008).

[82] A. Gubenko, I. Krestnikov, D. Livshtis, S. Mikhrin, A. Kovsh, L. West, C. Bornholdt, N. Grote and A. Zhukov, *Electron. Lett.* vol.43, p.1430, (2007)
.
[83] A. E. Zhukov, A. R. Kovsh, *Quantum Electron*. vol.38, p.409, (2008)
.
[84] G. L. Wojcik, D. Yin, A. R. Kovsh, A. E. Gubenko, I. L. Krestnikov, S. S. Mikhrin, D. A. Livshits, D. A. Fattal, M. Fiorentino, R. G. Beausoleil, *Proceedings of the SPIE*, vol.7230, p.72300M, (2009).

[85] A. M. Rollins, M. V. Sivak Jr., S. Radhakrishnan, J. H. Lass, D. Huang, K. D. Cooper, and J. A. Izatt, *Optics and Photonics News*, 36,( 2002).

[86] W. Ha, V. Gambin, M. Wistey, S. Bank, S. Kim, and J. S. Harris, Jr., *Compound Semiconductor*, vol. 14, p. 591, (2005).

[87] P. Bhattacharya, J. Singh, H. Yoon, X. Zhang, A. Gutierrez-Aitken, and Y. Lam, *IEEE J. Quantum Electron.*, vol.32, p.1620, (1996).

[88] A. Markus, J. X. Chen, C. Paranthoen, A. Fiore, C. Platz, and O. Gauthier-Lafaye, *Appl. Phys. Lett.*, vol. 82, p.1818, (2003).

[89] A. Markus, J. X. Chen, O. Gauthier-Lafaye, J. Guy, C. Paranthoen and A. Fiore, *IEEE Select. Topics Quantum Electron.*, vol. 9, p.1308, ( 2003).

[90] A. Kovsh, I. Krestnikov, D. Livshits, S. Mikhrin, and J. Weimert, *Optics Lett*, vol.32, p.793, (2007).

[91] I. P. Marko, N. F. Massé, S. J. Sweeney, A. D. Andreev, A. R. Adams, N. Hatori, and M. Sugawara, *Appl. Phys. Lett.*, vol.87, p. 211114, (2005).

[92] H. Chen, Z. Zou, O. B. Shchekin, and D. G. Deppe, *Electron. Lett.*, vol.36, p.1703, (2000).

[93] B.W. Hakki, and T.L. Paoli, *J. Appl. Phys.*, vol.46, p.1299, (1975)

[94] G. Maxwell, (Invited) OFC/NFOEC OWI3, (2008).

[95] A.W. Fang, E. Lively, Y.-H. Kuo, D. Liang, and J.E.Bowers, *Opt. Express*, vol. 16, no.7, p. 4413, (2008).

[96] A. Gubenko, I. Krestnikov, D. Livshits, S. Mikhrin, A.Kovsh, L.West, C. Bornholdt, N. Grote and A. Zhukov, *Electron.Lett*.,vol. 43, no. 25, p. 1430, (2007).

[97] G. Wojcik, D. Yin, A. Kovsh, A. Gubenko, I. Krestnikov, S. Mikhrin, D. Livshits, D. Fattal, M. Fiorentino, and R. Beausoleil, *SPIE Photonics West*, p. 7230, (2009).

[98] D. Livshits, D. Yina, A. Gubenkob, I.Krestnikovb, S. Mikhrinb, A. Kovsha, and G. Wojcika, *Proc. of SPIE*, vol. 7607, p. 76070W-1, (2010).

[99] R. Beausoleil, Invited Paper, *PhotonicsWest '08*, vol. p. 6898, (2008).

[100] S. Rochus, *OIDA Forum - Future Optical Communication Systems*, Baltimore, MD, Nov.7-8, (2007).

[101] D. Klotzkin, K. Kamath, K. Vineberg, P. Bhattacharya, R. Murty, and J. Laskar, *IEEE Photon. Technol. Lett.,* vol.10, no.7, p.932, (1998).

[102] N. Kirstaedter, O. G. Schmidt, N. N. Ledentsov, D. Bimberg, V. M. Ustinov, A.Y. Egorov, A. E. Zhukov, M. V. Maximov, P. S. Kopev, and Z. I. Alferov, *Appl. Phys. Lett.,* vol.69, no. 9, p.1226, (1996).

[103] H. Saito, K. Nishi, and S. Sugou, *Electron. Lett.,* vol.37, no 21, p.1293 (2001).

[104] T. C. Newell, D. J. Bossert, A. Stintz, B. Fuchs, K. J. Malloy, and L. F. Lester, *IEEE Photon.Technol. Lett.,* vol.11, no12, p. 1527, (1999).

[105] K. Goshima, T. Amano, K. Akita, R. Akimoto,T. Sugaya, M. Mori, and K. Komori, *Jap. J. Appl. Phys.,* vol.48, p.050203, (2009).

[106] R. K. Price, V. C. Elarde, and J. J. Coleman, *Proc. SPIE*, vol. 6133, p. 613317, (2006).

[107] R. K. Price, V. B. Verma, V.C. Elarde, and J. J. Coleman, *J. Appl. Physics*, vol. 103, p.013108, (2008).

[108] R. K. Price, V.C. Elarde, and J. J. Coleman, *IEEE J. Quantum Electron.,* vol.42 no. 7, p.667, (2006).

[109] D. J. Robbins, J. P. Duck, N. D. Whitbread, A. J. Ward, B. Rousseau, and F. Lelarge, *IEEE Photon. Tech. Lett.,* vol. 20, no2, p. 147, (2008).

[110] P. Bhattacharya, and Z. Mi, *Proc. IEEE*, vol.95 , no. 9, p.1723, (2007).

[111] E. Deichsel, F. Eberhard, P. Jager, and P. Unger, *IEEE J. Select. Topics in Quantum Electron.,*vol.7, (2001).

[112] Z. Mi, P. Bhattacharya, and S. Fathpour *Appl. Phys. Lett.* vol.86, p.153109, (2005).

[113] T.Takagi, F. Koyama, and K. Iga, *IEEE J. Quantum Electron*., vol.27, no. 6, p.1511, (1991).

[113] H. Uenohara, K. Iga and F. Koyama, *Electron. Communication. Japan.,* vol.71, no.5, p. 851, (1988).

[114] J. Yang, and P. Bhattacharya, *J. Lightwave Tech.* vol.25, no.7, p.1826, (2007).

[115] N. Daldosso, M. Melchiorri, F. Riboli, M. Girardini, G. Pucker, M. Crivellari, P. Bellutti, A. Lui, and L. Pavesi, *J. Lightwave Tech.,* vol. 22, no.7, p.1734, (2004).

[116] F. Morichetti, A. Melloni, M. Martinelli, R.G. Heideman, A. Leinse, D. H. Geuzebroek, and A. Borreman, *J. Lightwave Tech.,* vol.25, no.9, p.2579, (2007).

[117] S.C. Mao, Y.L. Xu, S.H. Tao, X.W. Sun, M.B. Yu, G.Q. Lo and D.L. Kwong, *Photonics Global Singapore*, (2008).

[118] D. H. Yoon, S. G. Yoon, Y. T. Kim, *Thin Film Solids*, vol.515, p. 5004, (2007).

[119] J. Jang, and P. Bhattacharya, *Optics Express*, vol.16, no. 7, p.5136, (2008).

[120] F. Grillot, L. Vivien, S. Laval, D. Pascal, and E. Cassan, *IEEE Photon. Tech Lett.,* vol.16, no. 7, p. 1661, (2004).

[121] M. G. Thompson, A. R. Rae, M. Xia, R. V. Penty, and I. H. White, *IEEE J. Select. Topics Quantum Electron.,*vol.15, no.3 , p.661, (2009).

[122] A. E. Zhukov, M. V. Maximov, N. Y. Gordeev, A. V. Savelyev, D. A. Livshits and A. R. Kovsh, *Semicond. Sci. Technol.* vol.26, p.014004 (2011).

[123] C. Ribbat, R. L. Sellin, I. Kaiander, F. Hopfer, N.N. Ledentsov, D. Bimberg, A. R. Kovsh, V. M. Ustinov, A. E. Zhukov, and M. V. Maximov, *Appl. Phys. Lett.,* vol.82 , no.6, p. 952, (2003).

[125] J. Yang, *Dissertation*, University of Michigan, p. 115 (2008).